

1 A search for sparticles in zero lepton final states

2 Russell W. Smith

3 Submitted in partial fulfillment of the

4 requirements for the degree of

5 Doctor of Philosophy

6 in the Graduate School of Arts and Sciences

7 COLUMBIA UNIVERSITY

8 2016

9

© 2016

10

Russell W. Smith

11

All rights reserved

12

ABSTRACT

13

A search for sparticles in zero lepton final states

14

Russell W. Smith

15 TODO : Here's where your abstract will eventually go. The above text is all in the
16 center, but the abstract itself should be written as a regular paragraph on the page,
17 and it should not have indentation. Just replace this text.

Contents

19	Contents	i
20	1 Introduction	1
21	2 The Standard Model	5
22	2.1 Overview	5
23	2.2 Field Content	6
24	2.3 Deficiencies of the Standard Model	15
25	3 Supersymmetry	21
26	3.1 Supersymmetric theories : from space to superspace	21
27	3.2 Minimally Supersymmetric Standard Model	24
28	3.3 Phenomenology	30
29	3.4 How SUSY solves the problems with the SM	33
30	3.5 Conclusions	35
31	4 The Large Hadron Collider	37
32	4.1 Basics of Accelerator Physics	37
33	4.2 Accelerator Complex	39
34	4.3 Large Hadron Collider	41
35	4.4 Dataset Delivered by the LHC	43
36	5 The ATLAS detector	49

37	5.1	Magnets	50
38	5.2	Inner Detector	52
39	5.3	Calorimetry	56
40	5.4	Muon Spectrometer	61
41	5.5	Trigger System	66
42	6	Object Reconstruction	73
43	6.1	Primitive Object Reconstruction	73
44	6.2	Physics Object Reconstruction and Quality Identification	79
45	7	Recursive Jigsaw Reconstruction	105
46	7.1	Razor variables	105
47	7.2	Recursive Jigsaw Reconstruction	108
48	7.3	Variables used in the search for zero lepton SUSY	109
49	8	Table of Contents Title	111
50	9	A search for supersymmetric particles in zero lepton final states with the Recursive Jigsaw Technique	113
51	9.1	Object reconstruction	113
52	9.2	Signal regions	114
53	9.3	Background estimation	114
55	10	Results	115
56	10.1	Statistical Analysis	115
57	10.2	Signal Region distributions	115
58	10.3	Pull Plots	115
59	10.4	Systematic Uncertainties	115
60	10.5	Exclusion plots	115

61	Conclusion	117
62	10.6 New Section	117
63	Bibliography	119
64	Quantum Field Theory and Symmetries	129
65	Quantum Field Theory	129
66	Symmetries	130
67	Local symmetries	132

Acknowledgements

Dedication

Introduction

72 Particle physics is a remarkably successful field of scientific inquiry. The ability to
 73 precisely predict the properties of a exceedingly wide range of physical phenomena,
 74 such as the description of the cosmic microwave background [1, 2], the understanding
 75 of the anomalous magnetic dipole moment of the electron [3, 4], and the measurement
 76 of the number of weakly-interacting neutrino flavors [5] is truly amazing.

77 The theory that has allowed this range of predictions is the *Standard Model*
 78 of particle physics (SM). The Standard Model combines the electroweak theory of
 79 Glashow, Weinberg, and Salam [6–8] with the theory of the strong interactions, as
 80 first envisioned by Gell-Mann and Zweig [9, 10]. This quantum field theory (QFT)
 81 contains a tiny number of particles, whose interactions describe phenomena up to at
 82 least the TeV scale. These particles are manifestations of the fields of the Standard
 83 Model, after application of the Higgs Mechanism. The particle content of the SM
 84 consists only of the six quarks, the six leptons, the four gauge bosons, and the scalar
 85 Higgs boson.

86 Despite its impressive range of described phenomena, the Standard Model has
 87 some theoretical and experimental deficiencies. The SM contains 26 free parameters
 88 ¹. It would be more theoretically pleasing to understand these free parameters in
 89 terms of a more fundamental theory. The major theoretical concern of the Standard
 90 Model, as it pertains to this thesis, is the *hierarchy problem*[11–15]. The light mass

¹This is the Standard Model corrected to include neutrino masses. These parameters are the fermion masses (6 leptons, 6 quarks), CKM and PMNS mixing angles (8 angles, 2 CP-violating phases), W/Z/Higgs masses (3), the Higgs field expectation value, and the couplings of the strong, weak, and electromagnetic forces (3 α_{force}).

of the Higgs boson (125 GeV) should be quadratically dependent on the scale of UV physics, due to the quantum corrections from high-energy physics processes. The most perplexing experimental issue is the existence of *dark matter*, as demonstrated by galactic rotation curves [16–22]. This data has shown that there exists additional matter which has not yet been seen interacting with the particles of the Standard Model. There is no particle in the SM which can act as a candidate for dark matter.

Both of these major issues, as well as numerous others, can be solved by the introduction of *supersymmetry* (SUSY) [15, 23–35]. In supersymmetric theories, each SM particles has a so-called *superpartner*, or sparticle partner, differing from given SM particle by 1/2 in spin. These theories solve the hierarchy problem, since the quantum corrections induced from the superpartners exactly cancel those induced by the SM particles. In addition, these theories are usually constructed assuming *R*–parity, which can be thought of as the “charge” of supersymmetry, with SM particles having $R = 1$ and sparticles having $R = -1$. In collider experiments, since the incoming SM particles have total $R = 1$, the resulting sparticles are produced in pairs. This produces a rich phenomenology, which is characterized by significant hadronic activity and large missing transverse energy (E_T^{miss}), which provide significant discrimination against SM backgrounds [36].

Despite the power of searches for supersymmetry where E_T^{miss} is a primary discriminating variable, there has been significant interest in the use of other variables to discriminate against SM backgrounds. These include searches employing variables such as αT , $M_{T,2}$, and the razor variables (M_R, R^2) [37–47]. In this thesis, we will present the first search for supersymmetry using the novel Recursive Jigsaw Reconstruction (RJR) technique. RJR can be considered the conceptual successor of the razor variables. We impose a particular final state “decay tree” on an events, which roughly corresponds to a simplified Feynmann diagram in decays containing weakly-interacting particles. We account for the missing degrees of freedom associated

118 to the weakly-interacting particles by a series of simplifying assumptions, which allow
119 us to calculate our variables of interest at each step in the decay tree. This allows an
120 unprecedented understanding of the internal structure of the decay and the ability to
121 construct additional variables to reject Standard Model backgrounds.

122 This thesis details a search for the superpartners of the gluon and quarks, the
123 gluino and squarks, in final states with zero leptons, with 13.3 fb^{-1} of data using the
124 ATLAS detector. We organize the thesis as follows. The theoretical foundations of
125 the Standard Model and supersymmetry are described in Chapters 2 and 3. The
126 Large Hadron Collider and the ATLAS detector are presented in Chapters 4 and 5.
127 Chapter 5 provides a detailed description of Recursive Jigsaw Reconstruction and a
128 description of the variables used for the particular search presented in this thesis.
129 Chapter 6 presents the details of the analysis, including details of the dataset, object
130 reconstruction, and selections used. In Chapter 7, the final results are presented;
131 since there is no evidence of a supersymmetric signal in the analysis, we present the
132 final exclusion curves in simplified supersymmetric models.

2.1 Overview

A Standard Model is another name for a theory of the internal symmetry group $SU(3)_C \otimes SU(2)_L \otimes U(1)_Y$, with its associated set of parameters. *The Standard Model* refers specifically to a Standard Model with the proper parameters to describe the universe. The SM is the culmination of years of work in both theoretical and experimental particle physics. **TODO: cite** In this thesis, we take the view that theorists construct a model with the field content and symmetries as inputs, and write down the most general Lagrangian consistent with those symmetries. Assuming this model is compatible with nature (in particular, the predictions of the model are consistent with previous experiments), experimentalists are responsible measuring the parameters of this model. This will be applicable for this chapter and the following one.

Additional theoretical background is in 10.6. The philosophy and notations are inspired by [48, 49].

¹⁴⁹ **2.2 Field Content**

The Standard Model field content is

$$\begin{aligned} \text{Fermions} &: Q_L(3, 2)_{+1/3}, U_R(3, 1)_{+4/3}, D_R(3, 1)_{-2/3}, L_L(1, 2)_{-1}, E_R(1, 1)_{-2} \\ \text{Scalar (Higgs)} &: \phi(1, 2)_{+1} \\ \text{Vector Fields} &: G^\mu(8, 1)_0, W^\mu(1, 3)_0, B^\mu(1, 1)_0 \end{aligned} \tag{2.1}$$

¹⁵⁰ where the $(A, B)_Y$ notation represents the irreducible representation under $SU(3)$
¹⁵¹ and $SU(2)$, with Y being the electroweak hypercharge. Each of these fermion fields
¹⁵² has an additional index, representing the three generation of fermions.

¹⁵³ We observed that Q_L , U_R , and D_R are triplets under $SU(3)_C$; these are the *quark*
¹⁵⁴ fields. The *color* group, $SU(3)_C$ is mediated by the *gluon* field $G^\mu(8, 1)_0$, which has
¹⁵⁵ 8 degrees of freedom. The fermion fields $L_L(1, 2)_{-1}$ and $E_R(1, 1)_{-2}$ are singlets under
¹⁵⁶ $SU(3)_C$; we call them the *lepton* fields.

¹⁵⁷ Next, we note the “left-handed” (“right-handed”) fermion fields, denoted by L (R)
¹⁵⁸ subscript, The left-handed fields form doublets under $SU(2)_L$. These are mediated
¹⁵⁹ by the three degrees of freedom of the “W” fields $W^\mu(1, 3)_0$. These fields only act
¹⁶⁰ on the left-handed particles of the Standard Model. This is the reflection of the
¹⁶¹ “chirality” of the Standard Model; the left-handed and right-handed particles are
¹⁶² treated differently by the electroweak forces. The right-handed fields, U_R , D_R , and
¹⁶³ E_R , are singlets under $SU(2)_L$.

¹⁶⁴ The $U(1)_Y$ symmetry is associated to the $B^\mu(1, 1)_0$ boson with one degree of
¹⁶⁵ freedom. The charge Y is known as the electroweak hypercharge.

¹⁶⁶ To better understand the phenomenology of the Standard Model, let us investigate
¹⁶⁷ each of the *sectors* of the Standard Model separately.

¹⁶⁸ **Electroweak sector**

The electroweak sector refers to the $SU(2)_L \otimes U(1)_Y$ portion of the Standard Model gauge group. Following our philosophy of writing all gauge-invariant and renormalizable terms, the electroweak Lagrangian can be written as

$$\mathcal{L} = W_a^{\mu\nu}W_a^\mu + B^{\mu\nu}B_{\mu\nu} + (D^\mu\phi)^\dagger D_\mu\phi - \mu^2\phi^\dagger\phi - \lambda(\phi^\dagger\phi)^2. \quad (2.2)$$

where $W_a^{\mu\nu}$ are the three ($a = 1, 2, 3$) gauge bosons associated to the $SU(2)_L$ gauge group, $B^{\mu\nu}$ is the one gauge boson of the $U(1)_Y$ gauge group, and ϕ is the complex Higgs multiplet. The covariant derivative D^μ is given by

$$D^\mu = \partial^\mu + \frac{ig}{2}W_a^\mu\sigma_a + \frac{ig'}{2}B^\mu \quad (2.3)$$

where $i\sigma_a$ are the Pauli matrices times the imaginary constant, which are the generators for $SU(2)_L$, and g and g' are the $SU(2)_L$ and $U(1)_Y$ coupling constants, respectively. The field strength tensors $W_a^{\mu\nu}$ and $B^{\mu\nu}$ are given by the commutator of the covariant derivative associated to each field

$$B^{\mu\nu} = \partial^\mu B^\nu - \partial^\nu B^\mu \quad (2.4)$$

$$W_a^{\mu\nu} = \partial^\mu W_a^\nu - \partial^\nu W_a^\mu - g\epsilon_{abc}W_a^\mu W_b^\nu, \quad i = 1, 2, 3$$

¹⁶⁹

¹⁷⁰ The terms in the Lagrangian 2.2 proportional to μ^2 and λ make up the “Higgs
¹⁷¹ potential” [50]. As normal (see Appendix 10.6), we restrict $\lambda > 0$ to guarantee our
¹⁷² potential is bounded from below, and we also require $\mu^2 < 0$, which gives us the
¹⁷³ standard “sombrero” potential shown in 2.1.

This potential has infinitely many minima at $\langle \phi \rangle = \sqrt{2m/\lambda}$; the ground state is *spontaneously* broken by the choice of ground state, which induces a vacuum expectation value (VEV). Without loss of generality, we can choose the Higgs field ϕ to point in

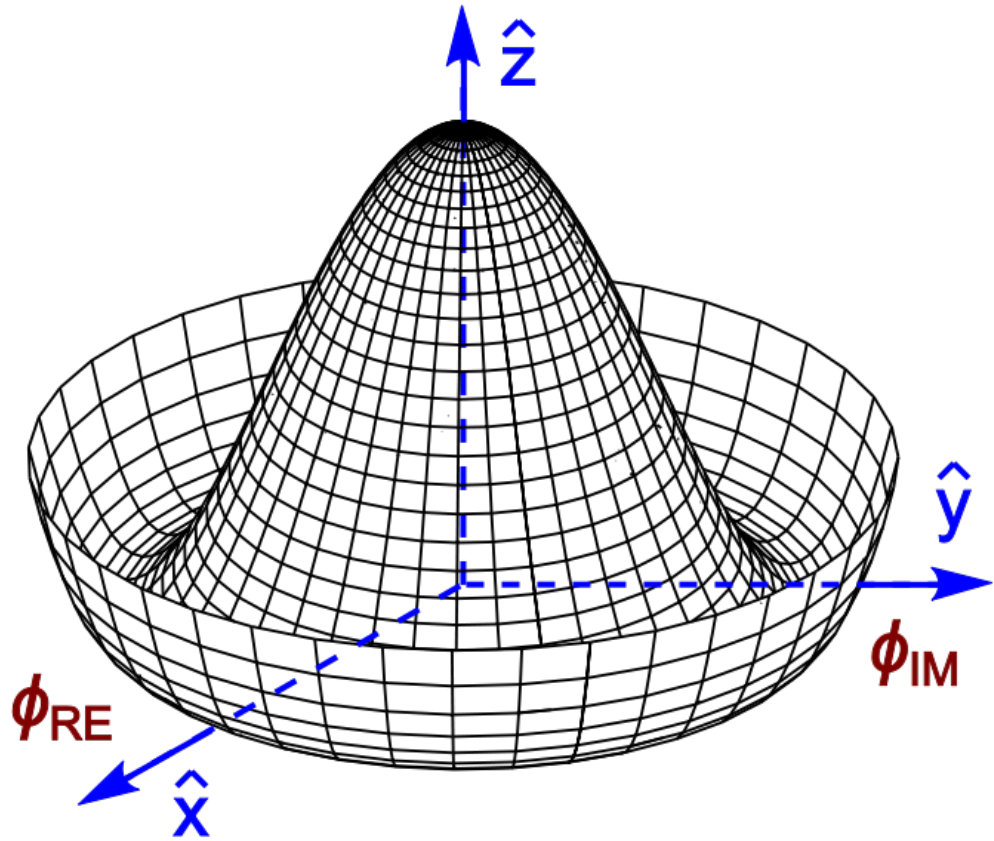


Figure 2.1: Sombrero potential

the real direction, and write the Higgs field ϕ in the following form :

$$\phi = \frac{1}{\sqrt{2}} \exp\left(\frac{i}{v} \sigma_a \theta_a\right) \begin{pmatrix} 0 \\ v + h(x) \end{pmatrix}. \quad (2.5)$$

We choose a gauge to rotate away the dependence on θ_a , such that we can write simply

$$\phi = \frac{1}{\sqrt{2}} \begin{pmatrix} 0 \\ v + h(x) \end{pmatrix}. \quad (2.6)$$

Now, we can see how the masses of the vector bosons are generated from the application of the Higgs mechanism. We plug Eq.2.6 back into the electroweak Lagrangian, and only showing the relevant mass terms in the vacuum state where

$h(x) = 0$ see that (dropping the Lorentz indices) :

$$\begin{aligned}\mathcal{L}_M &= \frac{1}{8} \left| \begin{pmatrix} gW_3 + g'B & g(W_1 - iW_2) \\ g(W_1 + iW_2) & -gW_3 + g'B \end{pmatrix} \begin{pmatrix} 0 \\ v \end{pmatrix} \right|^2 \\ &= \frac{g^2 v^2}{8} \left[W_1^2 + W_2^2 + \left(\frac{g'}{g} B - W_3 \right)^2 \right]\end{aligned}\quad (2.7)$$

Defining the *Weinberg* angle $\tan(\theta_W) = g'/g$ and the following *physical* fields :

$$\begin{aligned}W^\pm &= \frac{1}{\sqrt{2}}(W_1 \mp iW_2) \\ Z^0 &= \cos \theta_W W_3 - \sin \theta_W B \\ A^0 &= \sin \theta_W W_3 + \cos \theta_W B\end{aligned}\quad (2.8)$$

we can write the piece of the Lagrangian associated to the vector boson masses as

$$\mathcal{L}_{M_V} = \frac{1}{4}g^2 v^2 W^+ W^- + \frac{1}{8}(g^2 + g'^2)v^2 Z^0 Z^0. \quad (2.9)$$

and we have the following values of the masses for the vector bosons :

$$\begin{aligned}m_W^2 &= \frac{1}{4}v^2 g^2 \\ m_Z^2 &= \frac{1}{4}v^2(g^2 + g'^2) \\ m_A^2 &= 0\end{aligned}\quad (2.10)$$

¹⁷⁴ We thus see how the Higgs mechanism gives rise to the masses of the W^\pm and Z
¹⁷⁵ boson in the Standard Model; the mass of the photon is zero, as expected. The
¹⁷⁶ $SU(2)_L \otimes U(1)_Y$ symmetry of the initially massless $W_{1,2,3}$ and B fields is broken to
¹⁷⁷ the $U(1)_{EM}$. Of the four degrees of freedom in the complex Higgs doublet, three are
¹⁷⁸ “eaten” when we give mass to the W^\pm and Z_0 , while the other degree of freedom is
¹⁷⁹ the Higgs particle, as found in 2012 by the ATLAS and CMS collaborations [51, 52].

¹⁸⁰ Quantum Chromodynamics

Quantum chromodynamics (or the theory of the *strong* force) characterizes the behavior of *colored* particles, collectively known as *partons*. The partons of the

Standard Model are the (fermionic) quarks, and the (bosonic) gluons. The strong force is governed by $SU(3)_C$, an unbroken symmetry in the Standard Model, which implies the gluon remains massless. Defining the covariant derivative for QCD as

$$D^\mu = \partial^\mu + ig_s G_a^\mu L_a, a = 1, \dots, 8 \quad (2.11)$$

where L_a are the generators of $SU(3)_C$, and g_s is the coupling constant of the strong force. The QCD Lagrangian then is given by

$$\mathcal{L}_{\text{QCD}} = i\bar{\psi}_f D_\mu \gamma^\mu \psi_f - \frac{1}{4} G_{a,\mu\nu} G_a^{\mu\nu} \quad (2.12)$$

where the summation over f is for quarks *families*, and $G_a^{\mu\nu}$ is the gluon field strength tensor, given by

$$G_a^{\mu\nu} = \partial^\mu G_a^\nu - \partial^\nu G_a^\mu - g_s f^{abc} G_b^\mu G_c^\nu, a, b, c = 1, \dots, 8 \quad (2.13)$$

181 where f^{abc} are the structure constants of $SU(3)_C$, which are analogous to ϵ_{abc} for
 182 $SU(2)_L$. The kinetic term for the quarks is contained in the standard ∂_μ term, while
 183 the field strength term contains the interactions between the quarks and gluons, as
 184 well as the gluon self-interactions.

185 Written down in this simple form, the QCD Lagrangian does not seem much
 186 different from the QED Lagrangian, with the proper adjustments for the different
 187 group structures. The gluon is massless, like the photon, so one could naïvely expect
 188 an infinite range force, and it pays to understand why this is not the case. The
 189 reason for this fundamental difference is the gluon self-interactions arising in the
 190 field strength tensor term of the Lagrangian. This leads to the phenomena of *color*
 191 *confinement*, which describes how one only observes color-neutral particles alone in
 192 nature. In contrast to the electromagnetic force, particles which interact via the
 193 strong force experience a *greater* force as the distance between the particles increases.
 194 At long distances, the potential is given by $V(r) = -kr$. At some point, it is more
 195 energetically favorable to create additional partons out of the vacuum than continue

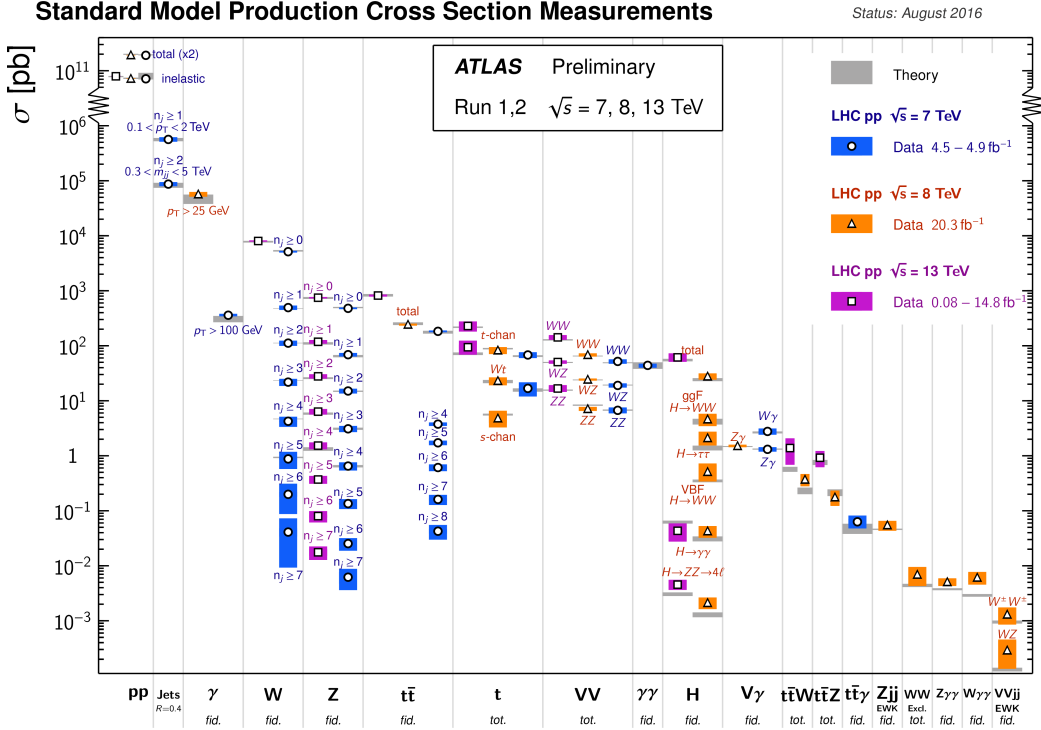


Figure 2.2: Cross-sections of various Standard Model processes

pulling apart the existing partons, and the colored particles undergo *fragmentation*. This leads to *hadronization*. Bare quarks and gluons are actually observed as sprays of hadrons (primarily kaons and pions); these sprays are known as *jets*, which are what are observed by experiments.

It is important to recognize the importance of understanding these QCD interactions in high-energy hadron colliders such as the LHC. Since protons are hadrons, proton-proton collisions such as those produced by the LHC are primarily governed by the processes of QCD. In particular, by far the most frequent process observed in LHC experiments is dijet production from gluon-gluon interactions (see Fig.2.2). These gluons that interact are part of the *sea* particles inside the proton; the simple $p = uud$ model does not apply. The main *valence* uud quarks are constantly interacting via gluons, which can themselves radiate gluons or split into quarks, and so on. A more useful understanding is given by the colloquially-known *bag* model [53, 54], where the proton is seen as a “bag” of (in principle) infinitely many partons, each with energy

210 $E < \sqrt{s} = 6.5$ TeV. One then collides this (proton) bag with another, and views the
211 products of this very complicated collision, where calculations include many loops in
212 nonperturbative QCD calculations.

213 Fortunately, we are generally saved by the QCD factorization theorems [55]. This
214 allows one to understand the hard (i.e. short distance or high energy) $2 \rightarrow 2$ parton
215 process using the tools of perturbative QCD, while making series of approximations
216 known as a *parton shower* model to understand the additional corrections from
217 nonperturbative QCD. We will discuss the reconstruction of jets by experiments in
218 Ch.5.

219 Fermions

220 We will now look more closely at the fermions in the Standard Model [56].

221 As noted earlier in Sec.2.2, the fermions of the Standard Model can be first
222 distinguished between those that interact via the strong force (quarks) and those
223 which do not (leptons).

There are six leptons in the Standard Model, which can be placed into three
generations.

$$\begin{pmatrix} e \\ \nu_e \end{pmatrix}, \begin{pmatrix} \mu \\ \nu_\mu \end{pmatrix}, \begin{pmatrix} \tau \\ \nu_\tau \end{pmatrix} \quad (2.14)$$

224 There is the electron (e), muon (μ), and tau (τ), each of which has an associated
225 neutrino (ν_e, ν_μ, ν_τ). Each of the so-called charged (“electron-like”) leptons has
226 electromagnetic charge -1 , while the neutrinos all have $q_{EM} = 0$.

227 Often in an experimental context, lepton is used to denote the stable electron
228 and metastable muon, due to their striking experimental signatures. Taus are often
229 treated separately, due to their much shorter lifetime of $\tau_\tau \sim 10^{-13}s$; these decay
230 through hadrons or the other leptons, so often physics analyses at the LHC treat
231 them as jets or leptons, as will be done in this thesis.

232 As the neutrinos are electrically neutral, nearly massless, and only interact via the
 233 weak force, it is quite difficult to observe them directly. Since LHC experiments rely
 234 overwhelmingly on electromagnetic interactions to observe particles, the presence of
 235 neutrinos is not observed directly. Neutrinos are instead observed by the conservation
 236 of four-momentum in the plane transverse to the proton-proton collisions, known as
 237 *missing transverse energy*.

There are six quarks in the Standard Model : up, down, charm, strange, top, and bottom. Quarks are similar organized into three generations :

$$\begin{pmatrix} u \\ d \end{pmatrix}, \begin{pmatrix} c \\ s \end{pmatrix}, \begin{pmatrix} t \\ b \end{pmatrix} \quad (2.15)$$

238 where we speak of “up-like” quarks and “down-like” quarks.

239 Each up-like quark has charge $q_{up} = 2/3$, while the down-like quarks have $q_{down} =$
 240 $-1/3$. At the high energies of the LHC, one often makes the distinction between
 241 the light quarks (u, d, c, s), the bottom quark, and top quark. In general, due to
 242 the hadronization process described above, the light quarks, with masses $m_q < \sim$
 243 $1.5 GeV$ are indistinguishable by LHC experiments. Their hadronic decay products
 244 generally have long lifetimes and they are reconstructed as jets.¹. The bottom quark
 245 hadronizes primarily through the B -mesons, which generally travels a short distance
 246 before decaying to other hadrons. This allows one to distinguish decays via b -quarks
 247 from other jets; this procedure is known as *b-tagging* and will be discussed more in
 248 Ch.5. Due to its large mass, the top quark decays before it can hadronize; there
 249 are no bound states associated to the top quark. The top is of particular interest at
 250 the LHC; it has a striking signature through its most common decay mode $t \rightarrow Wb$.
 251 Decays via tops, especially $t\bar{t}$ are frequently an important signal decay mode, or an
 252 important background process.

¹In some contexts, charm quarks are also treated as a separate category, although it is quite difficult to distinguish charm quarks from the other light quarks.

Standard Model Interactions (Forces Mediated by Gauge Bosons)



Figure 2.3: The interactions of the Standard Model

253 Interactions in the Standard Model

254 We briefly overview the entirety of the fundamental interactions of the Standard
255 Model; these can also be found in [2.3](#).

256 The electromagnetic force, mediated by the photon, interacts with via a three-
257 point coupling all charged particles in the Standard Model. The photon thus interacts
258 with all the quarks, the charged leptons, and the charged W^\pm bosons.

259 The weak force is mediated by three particles : the W^\pm and the Z^0 . The Z^0 can
260 interacts with all fermions via a three-point coupling. A real Z_0 can thus decay to

261 a fermion-antifermion pair of all SM fermions except the top quark, due to its large
262 mass. The W^\pm has two important three-point interactions with fermions. First, the
263 W^\pm can interact with an up-like quark and a down-like quark; an important example
264 in LHC experiments is $t \rightarrow Wb$. The coupling constants for these interactions are
265 encoded in the unitary matrix known as the Cabibbo–Kobayashi–Maskawa (CKM)
266 matrix [57, 58], and are generally known as flavor-changing interactions. Secondly,
267 the W^\pm interacts with a charged lepton and its corresponding neutrino. In this case,
268 the unitary matrix that corresponds to CKM matrix for quarks is the identity matrix,
269 which forbids (fundamental) vertices such as $\mu \rightarrow We$. For leptons, instead this is
270 a two-step process : $\mu \rightarrow \nu_m u W \rightarrow \nu_m u \bar{\nu}_e e$. Finally, there are the self-interactions
271 of the weak gauge bosons. There is a three-point and four-point interaction; all
272 combinations are allowed which conserve electric charge.

273 The strong force is mediated by the gluon, which as discussed above also carries
274 the strong color charge. There is the fundamental three-point interaction, where a
275 quark radiates a gluon. Additionally, there are the three-point and four-point gluon-
276 only interactions.

277 2.3 Deficiencies of the Standard Model

278 At this point, it is quite easy to simply rest on our laurels. This relatively simple
279 theory is capable of explaining a very wide range of phenomena, which ultimately
280 break down only to combinations of nine diagrams shown in Fig.2.3. Unfortunately,
281 there are some unexplained problems with the Standard Model. We cannot go
282 through all of the potential issues in this thesis, but we will motivate the primary
283 issues which naturally lead one to *supersymmetry*, as we will see in Ch.3.

The Standard Model has many free parameters; see Table 2.1. In general, we prefer models with less free parameters. A great example of this fact, and the primary

m_e	Electron mass	511 keV
m_μ	Muon mass	105.7 MeV
m_τ	Tau mass	1.78 GeV
m_u	Up quark mass	1.9 MeV ($m_{\bar{MS}} = 2\text{GeV}$)
m_d	Down quark mass	4.4 MeV ($m_{\bar{MS}} = 2\text{GeV}$)
m_s	Strange quark mass	87 MeV ($m_{\bar{MS}} = 2\text{GeV}$)
m_c	Charm quark mass	1.32 GeV ($m_{\bar{MS}} = m_c$)
m_b	Bottom quark mass	4.24 GeV ($m_{\bar{MS}} = m_b$)
m_t	Top quark mass	172.7 GeV (on-shell renormalization)
θ_{12} CKM	12-mixing angle	13.1°
θ_{23} CKM	23-mixing angle	2.4°
θ_{13} CKM	13-mixing angle	0.2°
δ CKM	CP-violating Phase	0.995
g'	U(1) gauge coupling	0.357 ($m_{\bar{MS}} = m_Z$)
g	SU(2) gauge coupling	0.652 ($m_{\bar{MS}} = m_Z$)
g_s	SU(3) gauge coupling	1.221 ($m_{\bar{MS}} = m_Z$)
θ_{QCD}	QCD vacuum angle	~0
VEV	Higgs vacuum expectation value	246 GeV
m_H	Higgs mass	125 GeV

Table 2.1: Parameters of the Standard Model. For values dependent on the renormalization scheme, we use a combination of the on-shell normalization scheme [59–62] and modified minimal subtraction scheme with $m_{\bar{MS}}$ as indicated in the table[63]

experimental evidence for EWSB, is the relationship between the couplings of the weak force and the masses of the gauge bosons of the weak force :

$$\rho \equiv \frac{m_W^2}{m_Z^2 \cos^2 \theta_W} \stackrel{?}{=} 1 \quad (2.16)$$

where ? indicates that this is a testable prediction of the Standard Model (in particular, that the gauge bosons gain mass through EWSB). This relationship has been measured within experimental and theoretical predictions. We would like to produce additional such relationships, which would exist if the Standard Model is a low-energy approximation of some other theory.

An additional issue is the lack of *gauge coupling unification*. The couplings of any quantum field theory “run” as a function of the distance scales (or inversely, energy scales) of the theory. The idea is closely related to the unification of the

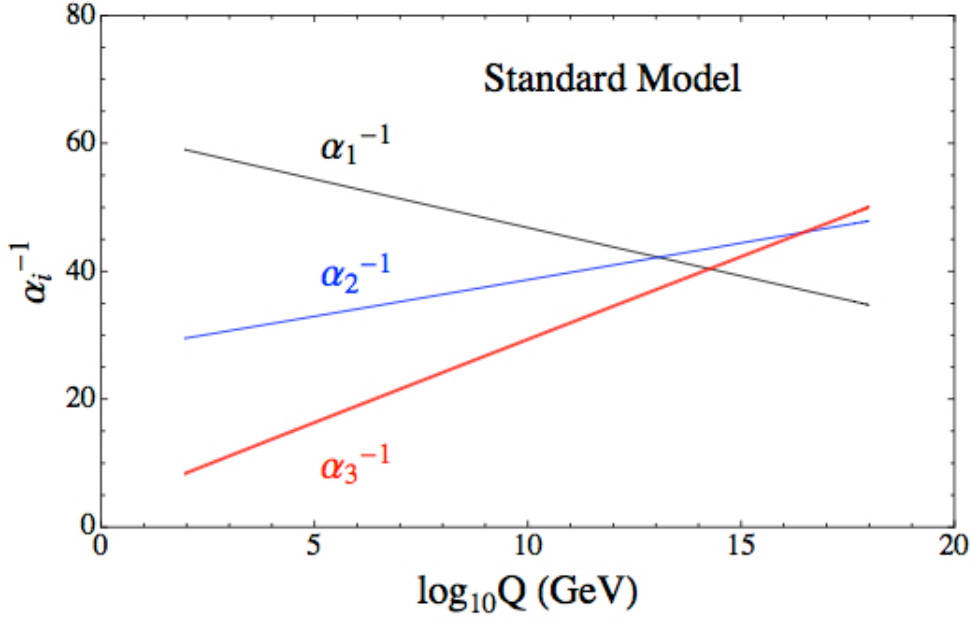


Figure 2.4: The running of Standard Model gauge couplings. The Standard Model couplings do not unify at high energies, which indicates it cannot completely describe nature through the Planck scale.

292 electromagnetic and weak forces at the so-called *electroweak scale* of $O(100 \text{ GeV})$.
 293 One would hope this behavior was repeated between the electroweak forces and the
 294 strong force at some suitable energy scale. The Standard Model does automatically
 295 not exhibit this behavior, as we can see in Fig.2.4.

The most significant problem with the Standard Model is the *hierarchy problem*. In its most straightforward incarnation, the Higgs scalar field is subject to quantum corrections through loop diagrams, as shown in Fig.2.5. For demonstration, we use the contributions from the top quark, since the top quark has the largest Higgs Yukawa coupling due to its large mass. In general, we should expect these corrections to be quadratically dependent on the scale of the ultraviolet physics, Λ . Briefly assume there is no new physics before the Planck scale of gravity, $\Lambda_{\text{Planck}} = 10^{19} \text{ GeV}$. In this case, we expect the corrections to the Higgs mass like

$$\delta m_H^2 \approx \left(\frac{m_t}{8\pi^2 \langle \phi \rangle_{VEV}} \right)^2 \Lambda_{\text{Planck}}^2. \quad (2.17)$$

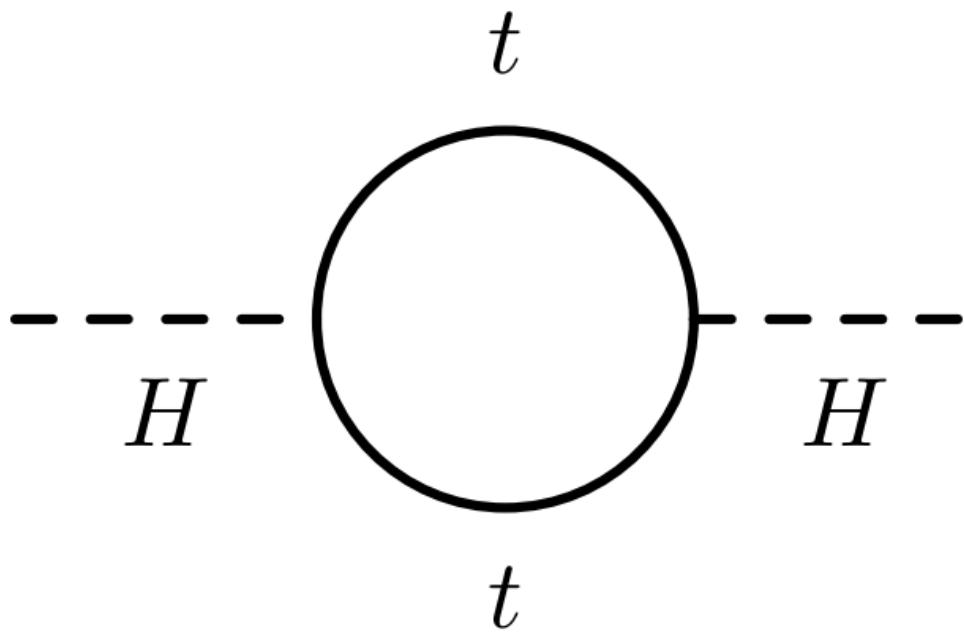


Figure 2.5: The dominant quantum loop correction to the Higgs mass in the Standard Model.

296 To achieve the miraculous cancellation required to get the observed Higgs mass of
 297 125 GeV, one needs to then set the bare Higgs mass m_0 , our input to the Standard
 298 Model Lagrangian, itself to a *precise* value $\sim 10^{19}$ GeV. This extraordinary level of
 299 parameter finetuning is quite undesirable, and within the framework of the Standard
 300 Model, there is little that can be done to alleviate this issue.

301 An additional concern, of a different nature, is the lack of a *dark matter* candidate
 302 in the Standard Model. Dark matter was discovered by observing galactic rotation
 303 curves, which showed that much of the matter that interacted gravitationally was
 304 invisible to our (electromagnetic) telescopes [16–22]. The postulation of the existence
 305 of dark matter, which interacts at least through gravity, allows one to understand
 306 these galactic rotation curves. Unfortunately, no particle in the Standard Model could
 307 possibly be the dark matter particle. The only candidate truly worth another look is
 308 the neutrino, but it has been shown that the neutrino content of the universe is simply
 309 too small to explain the galactic rotation curves [22, 64]. The experimental evidence

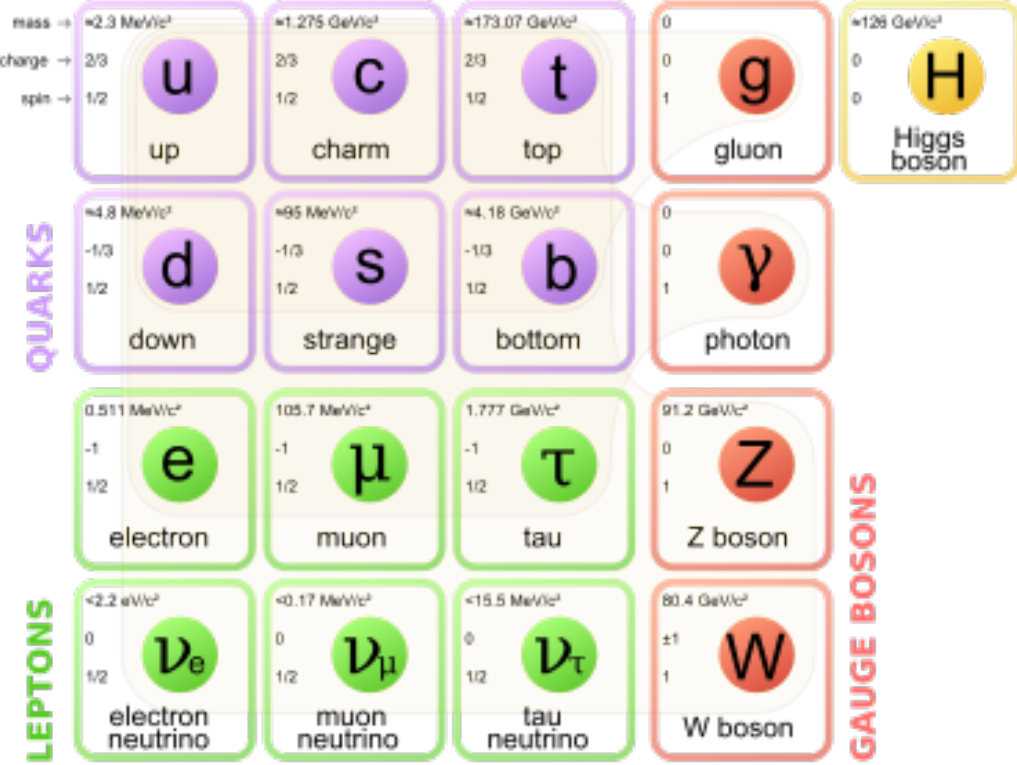


Figure 2.6: Particles of the Standard Model

310 from the galactic rotations curves thus show there *must* be additional physics beyond
 311 the Standard Model, which is yet to be understood.

312 In the next chapter, we will see how these problems can be alleviated by the theory
 313 of supersymmetry.

Supersymmetry

316 This chapter will introduce supersymmetry (SUSY) [15, 23–35]. We will begin by
 317 introducing the concept of a *superspace*, and discuss some general ingredients of
 318 supersymmetric theories. This will include a discussion of how the problems with the
 319 Standard Model described in Ch.2 are naturally fixed by these theories.

320 The next step is to discuss the particle content of the *Minimally Supersymmetric*
 321 *Standard Model* (MSSM). As its name implies, this theory contains the minimal
 322 additional particle content to make Standard Model supersymmetric. We then discuss
 323 the important phenomenological consequences of this theory, especially as it would
 324 be observed in experiments at the LHC.

325 **3.1 Supersymmetric theories : from space to
 326 superspace**

327 **Coleman-Mandula “no-go” theorem**

328 We begin the theoretical motivation for supersymmetry by citing the “no-go” theorem
 329 of Coleman and Mandula [65]. This theorem forbids *spin-charge unification*; it
 330 states that all quantum field theories which contain nontrivial interactions must be
 331 a direct product of the Poincaré group of Lorentz symmetries, the internal product
 332 from of gauge symmetries, and the discrete symmetries of parity, charge conjugation,
 333 and time reversal. The assumptions which go into building the Coleman-Mandula

theorem are quite restrictive, but there is one unique way out, which has become known as *supersymmetry* [26, 66]. In particular, we must introduce a *spinorial* group generator Q . Alternatively, and equivalently, this can be viewed as the addition of anti-commuting coordinates; space plus these new anti-commuting coordinates is then called *superspace* [67]. We will not investiage this view in detail, but it is also a quite intuitive and beautiful way to construct supersymmetry[15].

340 Supersymmetry transformations

A *supersymmetric* transformation Q transforms a bosonic state into a fermionic state, and vice versa :

$$Q |\text{Fermion}\rangle = |\text{Boson}\rangle \quad (3.1)$$

$$Q |\text{Boson}\rangle = |\text{Fermion}\rangle \quad (3.2)$$

To ensure this relation holds, Q must be an anticommuting spinor. Additionally, since spinors are inherently complex, Q^\dagger must also be a generator of the supersymmetry transformation. Since Q and Q^\dagger are spinor objects (with $s = 1/2$), we can see that supersymmetry must be a spacetime symmetry. The Haag-Lopuszanski-Sohnius extension [66] of the Coleman-Mandula theorem [65] is quite restrictive about the forms of such a symmetry. Here, we simply write the (anti-) commutation relations [15] :

$$Q_\alpha, Q_{\dot{\alpha}}^\dagger = -2\sigma_{\alpha\dot{\alpha}\mu} P_\mu \quad (3.3)$$

$$Q_\alpha, Q_{\dot{\beta}} = Q_{\dot{\alpha}}^\dagger, Q_{\dot{\beta}}^\dagger = 0 \quad (3.4)$$

$$[P^\mu, Q_\alpha] = [P^\mu, Q_{\dot{\alpha}}^\dagger] = 0 \quad (3.5)$$

343 **Supermultiplets**

344 In a supersymmetric theory, we organize single-particle states into irreducible
345 representations of the supersymmetric algebra which are known as *supermultiplets*.
346 Each supermultiplet contains a fermion state $|F\rangle$ and a boson state $|B\rangle$; these two
347 states are the known as *superpartners*. These are related by some combination of
348 Q and Q^\dagger , up to a spacetime transformation. Q and Q^\dagger commute with the mass-
349 squared operator $-P^2$ and the operators corresponding to the gauge transformations
350 [15]; in particular, the gauge interactions of the Standard Model. In an unbroken
351 supersymmetric theory, this means the states $|F\rangle$ and $|B\rangle$ have exactly the same mass,
352 electromagnetic charge, electroweak isospin, and color charges. One can also prove
353 [15] that each supermultiplet contains the exact same number of bosonic (n_B) and
354 fermion (n_F) degrees of freedom. We now explore the possible types of supermultiples
355 one can find in a renormalizable supersymmetric theory.

356 Since each supermultiplet must contain a fermion state, the simplest type of
357 supermultiplet contains a single Weyl fermion state ($n_F = 2$) which is paired with
358 $n_B = 2$ scalar bosonic degrees of freedom. This is most conveniently constructed as
359 single complex scalar field. We call this construction a *scalar supermultiplet* or *chiral*
360 *supermultiplet*. The second name is indicative; only chiral supermultiplets can contain
361 fermions whose right-handed and left-handed components transform differently under
362 the gauge interactions (as of course happens in the Standard Model).

363 The second type of supermultiplet we construct is known as a *gauge* supermul-
364 tiplet. We take a spin-1 gauge boson (which must be massless due to the gauge
365 symmetry, so $n_B = 2$) and pair this with a single massless Weyl spinor¹. The gauge
366 bosons transform as the adjoint representation of the their respective gauge groups;
367 their fermionic partners, which are known as gauginos, must also. In particular,
368 the left-handed and right-handed components of the gaugino fermions have the same

¹Choosing an $s = 3/2$ massless fermion leads to nonrenormalizable interactions.

369 gauge transformation properties.

370 Excluding gravity, this is the entire list of supermultiplets which can participate
371 in renormalizable interactions in what is known as $N = 1$ supersymmetry. This
372 means there is only one copy of the supersymmetry generators Q and Q^\dagger . This is
373 essentially the only “easy” phenomenological choice, since it is the only choice in four
374 dimensions which allows for the chiral fermions and parity violations built into the
375 Standard Model, and we will not look further into $N > 1$ supersymmetry in this thesis.

376 The primary goal, after understanding the possible structures of the multiplets
377 above, is to fit the Standard Model particles into a multiplet, and therefore make
378 predictions about their supersymmetric partners. We explore this in the next section.

379 **3.2 Minimally Supersymmetric Standard Model**

380 To construct what is known as the MSSM [[susyPrimer](#) , 68–71], we need a few
381 ingredients and assumptions. First, we match the Standard Model particles with
382 their corresponding superpartners of the MSSM. We will also introduce the naming
383 of the superpartners (also known as *sparticles*). We discuss a very common additional
384 restraint imposed on the MSSM, known as R –parity. We also discuss the concept of
385 soft supersymmetry breaking and how it manifests itself in the MSSM.

386 **Chiral supermultiplets**

387 The first thing we deduce is directly from Sec.?? . The bosonic superpartners
388 associated to the quarks and leptons *must* be spin 0, since the quarks and leptons must
389 be arranged in a chiral supermultiplet. This is essentially the note above, since the
390 chiral supermultiplet is the only one which can distinguish between the left-handed
391 and right-handed components of the Standard Model particles. The superpartners of
392 the quarks and leptons are known as *squarks* and *sleptons*, or *sfermions* in aggregate.

393 (for ‘‘scalar quarks’’, ‘‘scalar leptons’’, and ‘‘scalar fermion’’²). The ‘‘s-’’ prefix
 394 can also be added to the individual quarks i.e. *selectron*, *sneutrino*, and *stop*. The
 395 notation is to add a \sim over the corresponding Standard Model particle i.e. \tilde{e} , the
 396 selectron is the superpartner of the electron. The two-component Weyl spinors of the
 397 Standard Model must each have their own (complex scalar) partner i.e. e_L, e_R have
 398 two distinct partners : \tilde{e}_L, \tilde{e}_R . As noted above, the gauge interactions of any of the
 399 sfermions are identical to those of their Standard Model partners.

Due to the scalar nature of the Higgs, it must obviously lie in a chiral supermultiplet. To avoid gauge anomalies and ensure the correct Yukawa couplings to the quarks and leptons[15], we must add additional Higgs bosons to any supersymmetric theory. In the MSSM, we have two chiral supermultiplets. The SM (SUSY) parts of the multiplets are denoted $H_u(\tilde{H}_u)$ and $H_d(\tilde{H}_d)$. Writing out H_u and H_d explicitly:

$$H_u = \begin{pmatrix} H_u^+ \\ H_u^0 \end{pmatrix} \quad (3.6)$$

$$H_d = \begin{pmatrix} H_d^0 \\ H_d^- \end{pmatrix} \quad (3.7)$$

(3.8)

400 we see that H_u looks very similar to the SM Higgs with $Y = 1$, and H_d is symmetric
 401 to this with $+ \rightarrow -$, with $Y = -1$. The SM Higgs boson, h_0 , is a linear superposition
 402 of the neutral components of these two doublets. The SUSY parts of the Higgs
 403 multiplets, \tilde{H}_u and \tilde{H}_d , are each left-handed Weyl spinors. For generic spin-1/2
 404 sparticles, we add the ‘‘-ino’’ suffix. We then call the partners of the two Higgs
 405 collectively the *Higgsinos*.

²The last one should probably have bigger scare quotes.

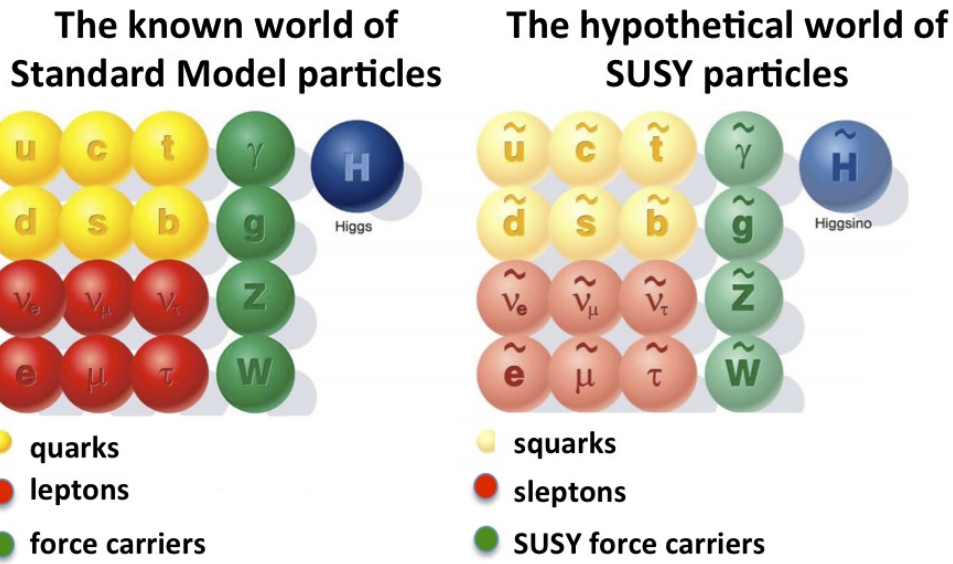


Figure 3.1: Particles of the MSSM

406 Gauge supermultiplets

407 The superpartners of the gauge bosons must all be in gauge supermultiplets since
 408 they contain a spin-1 particle. Collectively, we refer to the superpartners of the
 409 gauge bosons as the gauginos.

410 The first gauge supermultiplet contains the gluon, and its superpartner, which is
 411 known as the *gluino*, denoted \tilde{g} . The gluon is of course the SM mediator of $SU(3)_C$;
 412 the gluino is also a colored particle, subject to $SU(3)_C$. From the SM before EWSB,
 413 we have the four gauge bosons of the electroweak symmetry group $SU(2)_L \otimes U(1)_Y$:
 414 $W^{1,2,3}$ and B^0 . The superpartners of these particles are thus the *winos* $W^{\tilde{1},\tilde{2},\tilde{3}}$ and
 415 *bino* \tilde{B}^0 , where each is placed in another gauge supermultiplet with its corresponding
 416 SM particle. After EWSB, without breaking supersymmetry, we would also have the
 417 zino \tilde{Z}^0 and photino $\tilde{\gamma}$.

418 The entire particle content of the MSSM can be seen in Fig.3.1.

419 At this point, it's important to take a step back. Where are these particles?
 420 As stated above, supersymmetric theories require that the masses and all quantum



Figure 3.2: This Feynmann diagram shows how proton decay is induced in the MSSM, if one does not impose R -parity.

421 numbers of the SM particle and its corresponding sparticle are the same. Of course,
 422 we have not observed a selectron, squark, or wino. The answer, as it often is, is that
 423 supersymmetry is *broken* by the vacuum state of nature [15].

424 **R -parity**

This section is a quick aside to the general story. R – parity refers to an additional discrete symmetry which is often imposed on supersymmetric models. For a given particle state, we define

$$R = (-1)^{3(B-L)+2s} \quad (3.9)$$

425 where B, L is the baryon (lepton) number and s is the spin. The imposition of
 426 this symmetry forbids certain terms from the MSSM Lagrangian that would violate
 427 baryon and/or lepton number. This is required in order to prevent proton decay, as
 428 shown in Fig.3.2³. .

429 In supersymmetric models, this is a \mathbb{Z}_2 symmetry, where SM particles have $R = 1$
 430 and sparticles have $R = -1$. We will take R – parity as part of the definition of
 431 the MSSM. We will discuss later the *drastic* consequences of this symmetry on SUSY
 432 phenomenology

³Proton decay can actually be prevented by allowing only one of the four potential R-parity violating terms to survive.

433 **Soft supersymmetry breaking**

The fundamental idea of *soft* supersymmetry breaking[15, 34, 35, 72, 73] is that we would like to break supersymmetry without reintroducing the quadratic divergences we discussed at the end of Chapter 2. We write the Lagrangian in a form :

$$\mathcal{L}_{\text{MSSM}} = \mathcal{L}_{\text{SUSY}} + \mathcal{L}_{\text{soft}} \quad (3.10)$$

434 In this sense, the symmetry breaking is “soft”, since we have separated out the
 435 completely symmetric terms from those soft terms which will not allow the quadratic
 436 divergences to the Higgs mass.

437 The explicitly allowed terms in the soft-breaking Lagrangian are [35].

- 438 • Mass terms for the scalar components of the chiral supermultipletss
 439 • Mass terms for the Weyl spinor components of the gauge supermultipletss
 440 • Trilinear couplings of scalar components of chiral supermultiplets

In particular, using the field content described above for the MSSM, the softly-broken portion of the MSSM Lagrangian can be written

$$\mathcal{L}_{\text{soft}} = -\frac{1}{2} \left(M_3 \tilde{g} \tilde{g} + M_2 \tilde{W} \tilde{W} + M_1 \tilde{B} \tilde{B} + c.c. \right) \quad (3.11)$$

$$- \left(\tilde{u} a_u \tilde{Q} H_u - \tilde{d} a_d \tilde{Q} H_d - \tilde{e} a_e \tilde{L} H_d + c.c. \right) \quad (3.12)$$

$$- \tilde{Q}^\dagger m_Q^2 \tilde{Q} - \tilde{L}^\dagger m_L^2 \tilde{L} - \tilde{u} m_u^2 \tilde{u}^\dagger - \tilde{d} m_d^2 \tilde{d}^\dagger - \tilde{e} m_e^2 \tilde{e}^\dagger \quad (3.13)$$

$$- m_{H_u}^2 H_u^* H_u - m_{H_d}^2 H_d^* H_d - (b H_u H_d + cc). \quad (3.14)$$

441 where we have introduced the following notations :

442 1. M_3, M_2, M_1 are the gluino, wino, and bino masses.

443 2. a_u, a_d, a_e are complex 3×3 matrices in family space.

444 3. $m_Q^2, m_u^2, m_d^2, m_L^2, m_e^2$ are hermitian 3×3 matrices in family space.

445 4. $m_{H_u}^2, m_{H_d}^2, b$ are the SUSY-breaking contributions to the Higgs potential.

446 We have written matrix terms without any sort of additional notational decoration
 447 to indicate their matrix nature, and we now show why. The first term 1 are
 448 straightforward; these are just the straightforward mass terms for these fields. There
 449 are strong constraints on the off-diagonal terms for the matrices of 2 [74, 75]; for
 450 simplicity, we will assume that each $a_i, i = u, d, e$ is proportional to the Yukawa
 451 coupling matrix : $a_i = A_{i0}y_i$. The matrices in ?? can be similarly constrained by
 452 experiments [68, 75–82] Finally, we assume that the elements 4 contributing to the
 453 Higgs potential as well as all of the 1 terms must be real, which limits the possible
 454 CP-violating interactions to those of the Standard Model. We thus only consider
 455 flavor-blind, CP-conserving interactions within the MSSM.

The important mixing for mass and gauge interaction eigenstates in the MSSM occurs within electroweak sector, in a process akin to EWSB in the Standard Model. The neutral portions of the Higgsinos doublets and the neutral gauginos ($\tilde{H}_u^0, \tilde{H}_d^0, \tilde{B}^0, \tilde{W}^0$) of the gauge interaction basis mix to form what are known as the *neutralinos* of mass basis :

$$M_{\tilde{\chi}} = \begin{pmatrix} M_1 & 0 & -c_\beta s_W m_Z & s_\beta s_W m_Z \\ 0 & M_2 & c_\beta c_W m_Z & -s_\beta c_W m_Z \\ -c_\beta s_W m_Z & c_\beta c_W m_Z & 0 & -\mu \\ s_\beta s_W m_Z & -s_\beta c_W m_Z & -\mu & 0 \end{pmatrix} \quad (3.15)$$

456 where $s(c)$ are the sine and cosine of angles related to EWSB, which introduced
 457 masses to the gauginos and higgsinos. Diagonalization of this matrix gives the four
 458 neutralino mass states, listed without loss of generality in order of increasing mass :
 459 $\tilde{\chi}_{1,2,3,4}^0$.

460 The neutralinos, especially the lightest neutralino $\tilde{\chi}_1^0$, are important ingredients
 461 in SUSY phenomenology.

462 The same process can be done for the electrically charged gauginos with
463 the charged portions of the Higgsino doublets along with the charged winos
464 $(\tilde{H}_u^+, \tilde{H}_d^+, \tilde{W}^+, \tilde{W}^-)$. This leads to the *charginos*, again in order of increasing mass
465 : $\tilde{\chi}_{1,2}^\pm$.

466

3.3 Phenomenology

467 We are finally at the point where we can discuss the phenomenology of the MSSM,
468 in particular as it manifests itself at the energy scales of the LHC.

469 As noted above in Sec.3.2, the assumption of *R*–parity has important conse-
470 quences for MSSM phenomenology. The SM particles have $R = 1$, while the sparticles
471 all have $R = -1$. Simply, this is the “charge” of supersymmetry. Since the particles of
472 LHC collisions (pp) have total incoming $R = 1$, we must expect that all sparticles will
473 be produced in *pairs*. An additional consequence of this symmetry is the fact that the
474 lightest supersymmetric particle (LSP) is *stable*. Off each branch of the Feynmann
475 diagram shown in Fig., we have $R = -1$, and this can only decay to another sparticle
476 and a SM particle. Once we reach the lightest sparticle in the decay, it is absolutely
477 stable. This leads to the common signature E_T^{miss} for a generic SUSY signal.

478 For this thesis, we will be presenting an inclusive search for squarks and gluinos
479 with zero leptons in the final state. This is a very interesting decay channel⁴, due
480 to the high cross-sections of $\tilde{g}\tilde{g}$ and $\tilde{q}\tilde{q}$ decays, as can be seen in Fig.?? [83]. This
481 is a direct consequence of the fact that these are the colored particles of the MSSM.
482 Since the sparticles interact with the gauge groups of the SM in the same way as their
483 SM partners, the colored sparticles, the squarks and gluinos, are produced and decay
484 as governed by the color group $SU(3)_C$ with the strong coupling g_S . The digluino
485 production is particularly copious, due to color factor corresponding to the color octet

⁴Prior to Run1, probably the most *most* interesting SUSY decay channel.

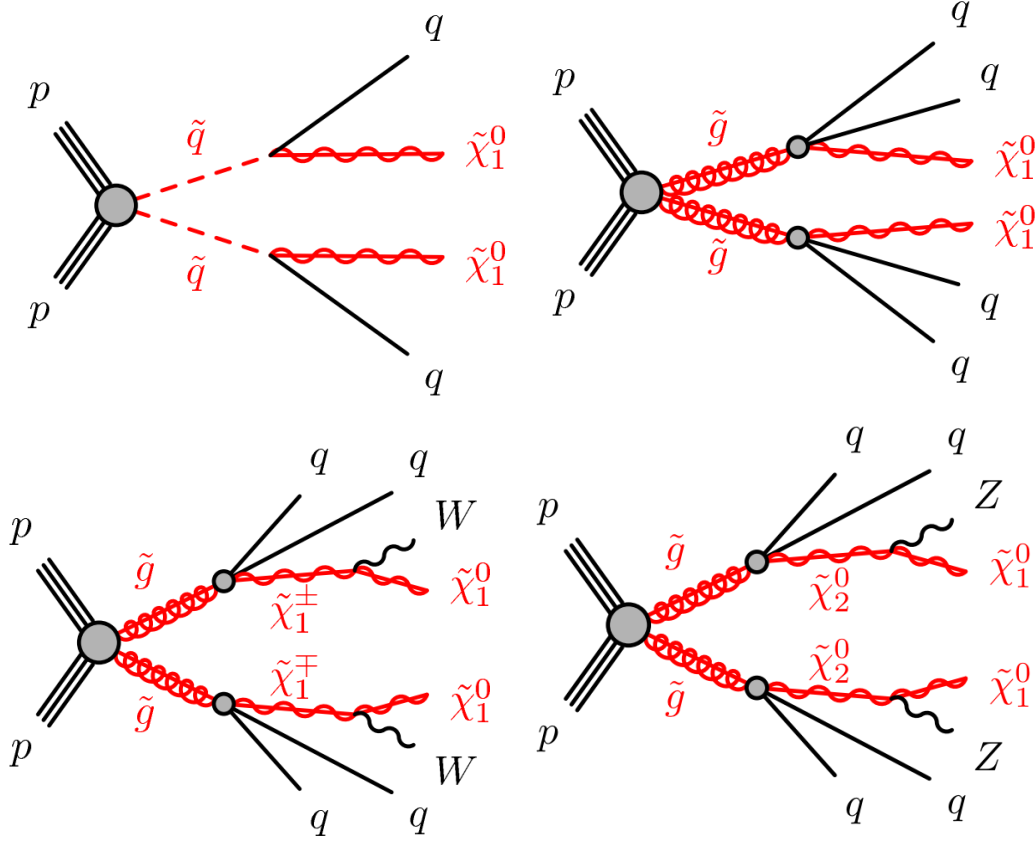


Figure 3.3: SUSY signals considered in this thesis

486 of $SU(3)C$.

487 In the case of disquark production, the most common decay mode of the squark in
 488 the MSSM is a decay directly to the LSP plus a single SM quark [15]. This means the
 489 basic search strategy of disquark production is two jets from the final state quarks,
 490 plus missing transverse energy for the LSPs. There are also cascade decays, the most
 491 common of which, and the only one considered in this thesis, is $\tilde{q} \rightarrow q\chi_1^\pm \rightarrow qW^\pm\chi_1^0$.

492 For digluino production, the most common decay is $\tilde{g} \rightarrow g\tilde{q}$, due to the large
 493 g_S coupling. The squark then decays as listed above. In this case, we generically
 494 search for four jets and missing transverse energy from the LSPs. We can also have
 495 the squark decay in association with a W^\pm or Z^0 ; in this thesis, we are interested in
 496 those cases where this vector boson goes hadronically.

497 In the context of experimental searches for SUSY, we often consider *simplified*

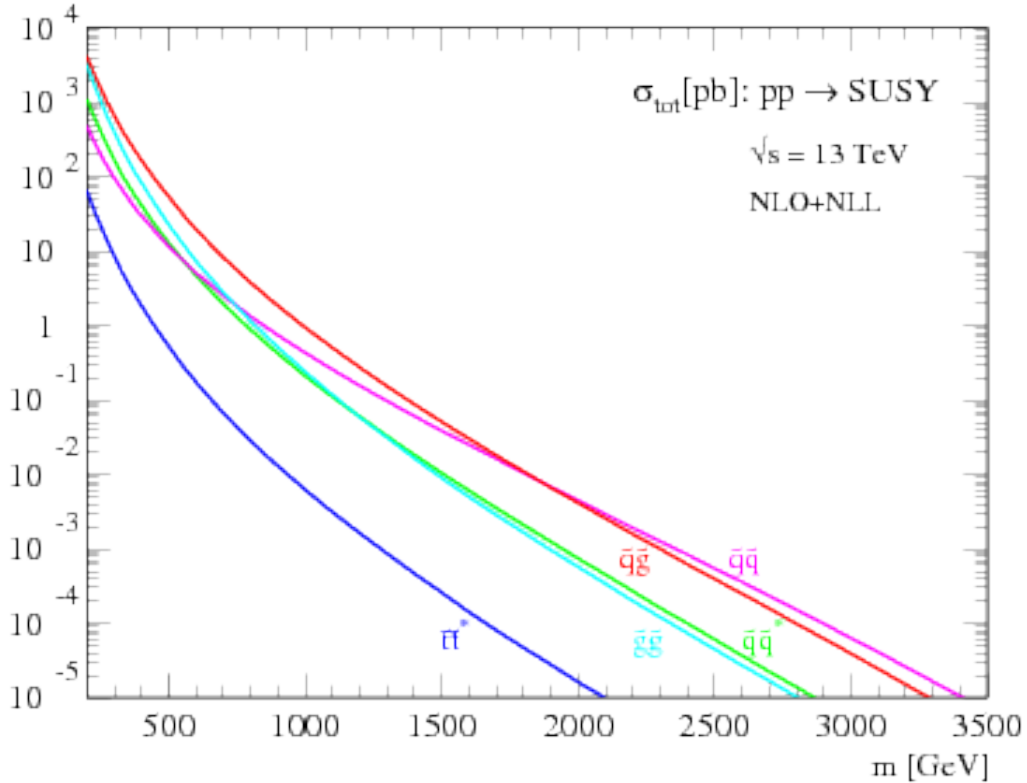


Figure 3.4: SUSY production cross-sections as a function of sparticle mass at $\sqrt{s} = 13 \text{ TeV}$.

498 *models*. These models make certain assumptions which allow easy comparisons of
 499 results by theorists and rival experimentalists. In the context of this thesis, the
 500 simplified models will make assumptions about the branching ratios described in the
 501 preceding paragraphs. In particular, we will often choose a model where the decay of
 502 interest occurs with 100% branching ratio. This is entirely for ease of interpretation
 503 by other physicists⁵, but it is important to recognize that these are more a useful
 504 comparison tool, especially with limits, than a strict statement about the potential
 505 masses of sought-after beyond the Standard Model particle.

⁵In the author's opinion, this often leads to more confusion than comprehension. We will revisit the shortcomings of simplified models in the Conclusion to this thesis.

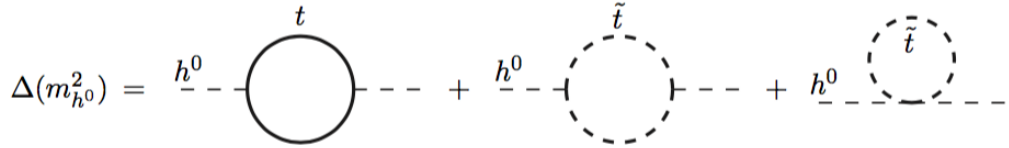


Figure 3.5: Loop diagrams correct the Higgs mass in the MSSM

506 3.4 How SUSY solves the problems with the SM

507 We now return to the issues with the Standard Model as described in Ch.2 to see
 508 how these issues are solved by supersymmetry.

509 Quadratic divergences to the Higgs mass

The quadratic divergences induced by the loop corrections to the Higgs mass, for example from the top Yukawa coupling, goes as

$$\delta m_H^2 \approx \left(\frac{m_t}{8\pi^2 \langle \phi \rangle_{VEV}} \right)^2 \Lambda_{Planck}^2. \quad (3.16)$$

510 The miraculous thing about SUSY is each of these terms *automatically* comes
 511 with a term which exactly cancels this contribution[15]. The fermions and bosons
 512 have opposite signs in this loop diagram to all orders in perturbation theory, which
 513 completely solves the hierarchy problem. This is the most well-motivated reason for
 514 supersymmetry.

515 Gauge coupling unification

516 An additional motivation for supersymmetry is seen by the gauge coupling unification
 517 high scales. In the Standard Model, as we saw the gauge couplings fail to unify at
 518 high energies. In the MSSM and many other forms of supersymmetry, the gauge
 519 couplings unify at high energy, as can be seen in Fig.???. This provides additional
 520 aesthetic motivation for supersymmetric theories.



Figure 3.6: The running of Standard Model gauge couplings; compare to Fig.2.4. The MSSM gauge couplings nearly intersect at high energies.

521 Dark matter

522 As we discussed previously, the lack of any dark matter candidate in the Standard
 523 Model naturally leads to beyond the Standard Model theories. In the Standard Model,
 524 there is a natural dark matter candidate in the lightest supersymmetric particle[15]
 525 The LSP would in dark matter experiments be called a *weakly-interacting massive*
 526 *particle* (WIMP), which is a type of cold dark matter [22, 84]. These WIMPs would
 527 only interact through the weak force and gravity, which is exactly as a model like the
 528 MSSM predicts for the neutralino. In Fig.3.7, we can see the current WIMP exclusions
 529 for a given mass. The range of allowed masses which have not been excluded for LSPs
 530 and WIMPs have significant overlap. This provides additional motivation outside of
 531 the context of theoretical details.



Figure 3.7: WIMP exclusions from direct dark matter detection experiments.

532 3.5 Conclusions

533 Supersymmetry is the most well-motivated theory for physics beyond the Standard
 534 Model. It provides a solution to the hierarchy problem, leads to gauge coupling
 535 unification, and provides a dark matter candidate consistent with galactic rotation
 536 curves. As noted in this chapter, due to the LSPs in the final state, most SUSY
 537 searches require a significant amount of missing transverse energy in combination
 538 with jets of high transverse momentum. However, there is some opportunity to do
 539 better than this, especially in final states where one has two weakly-interacting LSPs
 540 on opposite sides of some potentially complicated decay tree. We will see how this is
 541 done in Ch.??.

The Large Hadron Collider

544 The Large Hadron Collider (LHC) produces high-energy protons which are collided
 545 at the center of multiple large experiments at CERN on the outskirts of Geneva,
 546 Switzerland [85]. The LHC produces the highest energy collisions in the world,
 547 with design center-of-mass energy of $\sqrt{s} = 14$ TeV, which allows the experiments
 548 to investigate physics far beyond the reach of previous colliders. This chapter will
 549 summarize the basics of accelerator physics, especially with regards to discovering
 550 physics beyond the Standard Model. We will describe the CERN accelerator complex
 551 and the LHC.

552 **4.1 Basics of Accelerator Physics**

553 This section follows closely the presentation of [86].

Simple particle accelerators simply rely on the acceleration of charged particles in a static electric field. Given a field of strength E , charge q , and mass m , this is simply

$$a = \frac{qE}{m}. \quad (4.1)$$

554 For a given particle with a given mass and charge, this is limited by the static electric
 555 field which can be produced, which in turn is limited by electrical breakdown at high
 556 voltages.

557 There are two complementary solutions to this issue. First, we use the *radio*
 558 *frequency acceleration* technique. We call the devices used for this *RF cavities*. The

559 cavities produce a time-varied electric field, which oscillate such that the charged
 560 particles passing through it are accelerated towards the design energy of the RF
 561 cavity. This oscillation also induces the particles into *bunches*, since particles which
 562 are slightly off in energy from that induced by the RF cavity are accelerated towards
 563 the design energy.

Second, one bends the particles in a magnetic field, which allows them to pass through the same RF cavity over and over. This second process is often limited by *synchrotron radiation*, which describes the radiation produced when a charged particle is accelerated. The power radiated is

$$P \sim \frac{1}{r^2} \left(E/m \right)^4 \quad (4.2)$$

564 where r is the radius of curvature and E, m is the energy (mass) of the charged
 565 particle. Given an energy which can be produced by a given set of RF cavities (which
 566 is *not* limited by the mass of the particle), one then has two options to increase the
 567 actual collision energy : increase the radius of curvature or use a heavier particle.
 568 Practically speaking, the easiest options for particles in a collider are protons and
 569 electrons, since they are (obviously) copious in nature and do not decay¹. Given the
 570 dependence on mass, we can see why protons are used to reach the highest energies.
 571 The tradeoff for this is that protons are not point particles, and we thus we don't
 572 know the exact incoming four-vectors of the protons, as discussed in Ch.2.

The particle *beam* refers to the bunches all together An important property of a beam of a particular energy E , moving in uniform magnetic field B , containing particles of momentum p is the *beam rigidity* :

$$R \equiv rB = p/c. \quad (4.3)$$

573 The linear relation between r and p , or alternatively B and p have important
 574 consequences for LHC physics. For hadron colliders, this is the limiting factor on

¹Muon colliders are a really cool option at high energies, since the relativistic γ factor gives them a relatively long lifetime in the lab frame.

575 going to higher energy scales; one needs a proportionally larger magnetic field to
576 keep the beam accelerating in a circle.

577 Besides the rigidity of the beam, the most important quantities to characterize
578 a beam are known as the (normalized) *emittance* ϵ_N and the *betatron function* β .
579 These quantities determine the transverse size σ of a relativistic beam $v \gtrsim c$ beam :
580 $\sigma^2 = \beta^* \epsilon_N / \gamma_{\text{rel}}$, where β^* is the value of the betatron function at the collision point
581 and γ_{rel} is the Lorentz factor.

These quantities determine the *instantaneous luminosity* L of a collider, which combined with the cross-section σ of a particular physics process, give the rate of this physics process :

$$R = L\sigma. \quad (4.4)$$

The instantaneous luminosity L is given by :

$$L = \frac{f_{\text{rev}} N_b^2 F}{4\pi\sigma^2} = \frac{f_{\text{rev}} n N_b^2 \gamma_{\text{rel}} F}{4\pi\beta^* \epsilon_N}. \quad (4.5)$$

582 Here we have introduced the frequency of revolutions f_{rev} , the number of bunches n ,
583 the number of protons per bunch N_b^2 , and a geometric factor F related to the crossing
584 angle of the beams.

The *integrated luminosity* $\int L$ gives the total number of a particular physics process P , with cross-section σ_P .

$$N_P = \sigma_P \int L. \quad (4.6)$$

585 Due to this simple relation, one can also quantify the “amount of data delivered” by
586 a collider simply by $\int L$.

587 4.2 Accelerator Complex

588 The Large Hadron Collider is the last accelerator in a chain of accelerators which
589 together form the CERN accelerator complex, which can be seen in 4.1. The protons



Figure 4.1: The CERN accelerator complex.

begin their journey to annihilation in a hydrogen source, where they are subsequently ionized. The first acceleration occurs in the Linac 2, a linear accelerator composed of RF cavities. The protons leave the Linac 2 at an energy of 50 MeV and enter the Proton Synchrotron Booster (PSB). The PSB contains four superimposed rings, which accelerate the protons to 1.4 GeV. The protons are then injected into the Proton Synchrotron (PS). This synchrotron increases the energy up to 25 GeV. After leaving the PS, the protons enter the Super Proton Synchrotron (SPS). This is the last step before entering the LHC ring, and the protons are accelerated to 450 GeV. From the SPS, the protons are injected into the beam pipes of the LHC. The process to fill the LHC rings with proton bunches from start to finish typically takes about four minutes.

601 4.3 Large Hadron Collider

The Large Hadron Collider is the final step in the CERN accelerator complex, and produces the collisions analyzed in this thesis. From the point of view of experimentalists on the general-purpose ATLAS and CMS experiments, the main goal of the LHC is to deliver collisions at the highest possible energy, with the highest possible instantaneous luminosity. The LHC was installed in the existing 27 km tunnel used by the Large Electron Positron (LEP) collider [87]. This allowed the existing accelerator complex at CERN, described in the previous section, to be used as the injection system to prepare the protons up to 450 GeV. Many aspects of the LHC design were decided by this very fact, and specified the options allowed to increase the energy or luminosity. In particular, the radius of the tunnel was already specified; from Eq.4.3, this implies the momentum (or energy) of the beam is entirely determined by the magnetic field. Given the 27 km circumference of the LEP tunnel, one can calculate the required magnetic field to reach the 7 TeV per proton design energy of the LHC :

$$r = C/2\pi = 4.3 \text{ km} \quad (4.7)$$

$$\rightarrow B = \frac{p}{rc} = 5 \text{ T} \quad (4.8)$$

602 In fact, the LHC consists of 8 528 m straight portions consisting of RF cavities, used
603 to accelerate the particles, and 8 circular portions which bend the protons around the
604 LHC ring. These circular portions actually have a slightly smaller radius of curvature
605 $r = 2804 \text{ m}$, and we require $B = 8.33 \text{ T}$. To produce this large field, we need to use
606 superconducting magnets, as discussed in the next section.

607 Magnets

608 There are many magnets used by the LHC machine, but the most important are the
609 1232 dipole magnets; a schematic is shown in Fig.4.2 and a photograph is shown in



Figure 4.2: Schematic of an LHC dipole magnet.

610 Fig.4.3.

611 The magnets are made of Niobium and Titanium. The maximum field strength is
 612 10 T when cooled to 1.9 Kelvin. The magnets are cooled by superfluid helium, which
 613 is supplied by a large cryogenic system. Due to heating between the eight helium
 614 refrigerators and the beampipe, the helium is cooled in the refrigerators to 1.8 K.

615 A failure in the cooling system can cause what is known as a *quench*. If the
 616 temperature goes above the critical superconducting temperature, the metal loses its
 617 superconducting properties, which leads to a large resistance in the metal. This leads
 618 to rapid temperature increases, and can cause extensive damages if not controlled.

619 The dipole magnets are 16.5 meters long with a diameter of 0.57 meters. There
 620 are two individual beam pipes inside each magnet, which allows the dipoles to house
 621 the beams travelling in both directions around the LHC ring. They curve slightly,
 622 at an angle of 5.1 mrad, which carefully matches the curvature of the ring. The

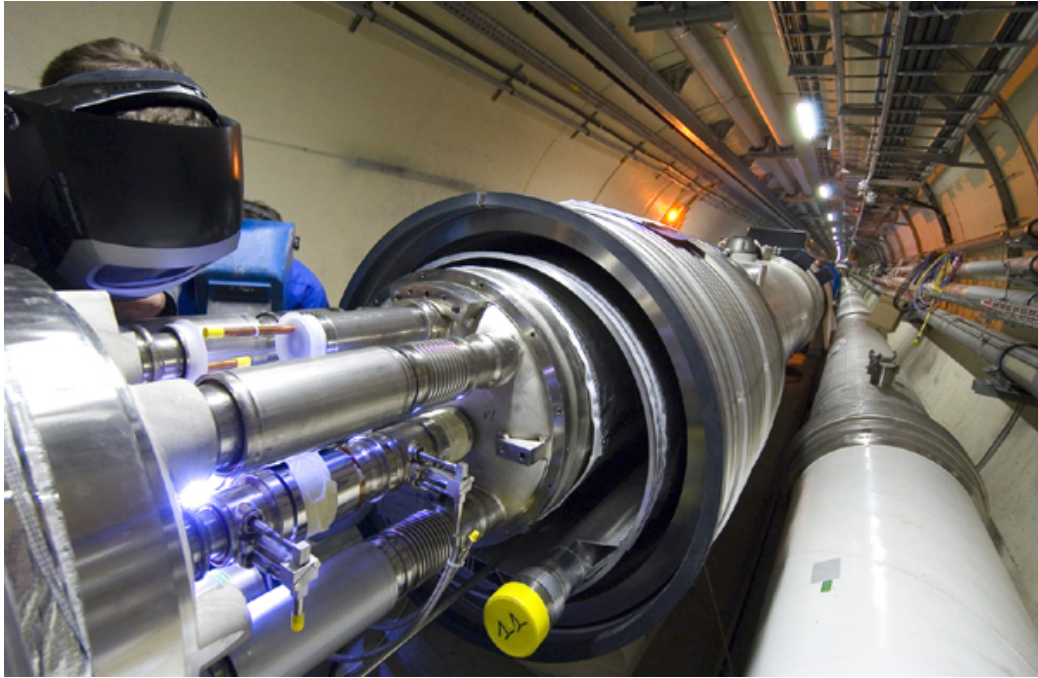


Figure 4.3: Photograph of a technician connecting an LHC dipole magnet.

623 beampipes inside of the magnets are held in high vacuum, to avoid stray particles
624 interacting with the beam.

625 **4.4 Dataset Delivered by the LHC**

626 In this thesis, we analyze the data delivered by the LHC to ATLAS in the 2015 and
627 2016 datasets. The beam parameters relevant to this dataset are available in Table
628 [4.1](#).

629 The peak instantaneous luminosity delivered in 2015 (2016) was $L =$
630 $5.2(11) \text{ cm}^{-2}\text{s}^{-1} \times 10^{33}$. One can note that the instantaneous luminosity delivered in
631 the 2016 dataset exceeds the design luminosity of the LHC. The total integrated
632 luminosity delivered was 13.3 fb^{-1} . In Figure [4.4](#), we display the integrated luminosity
633 as a function of day for 2015 and 2016.

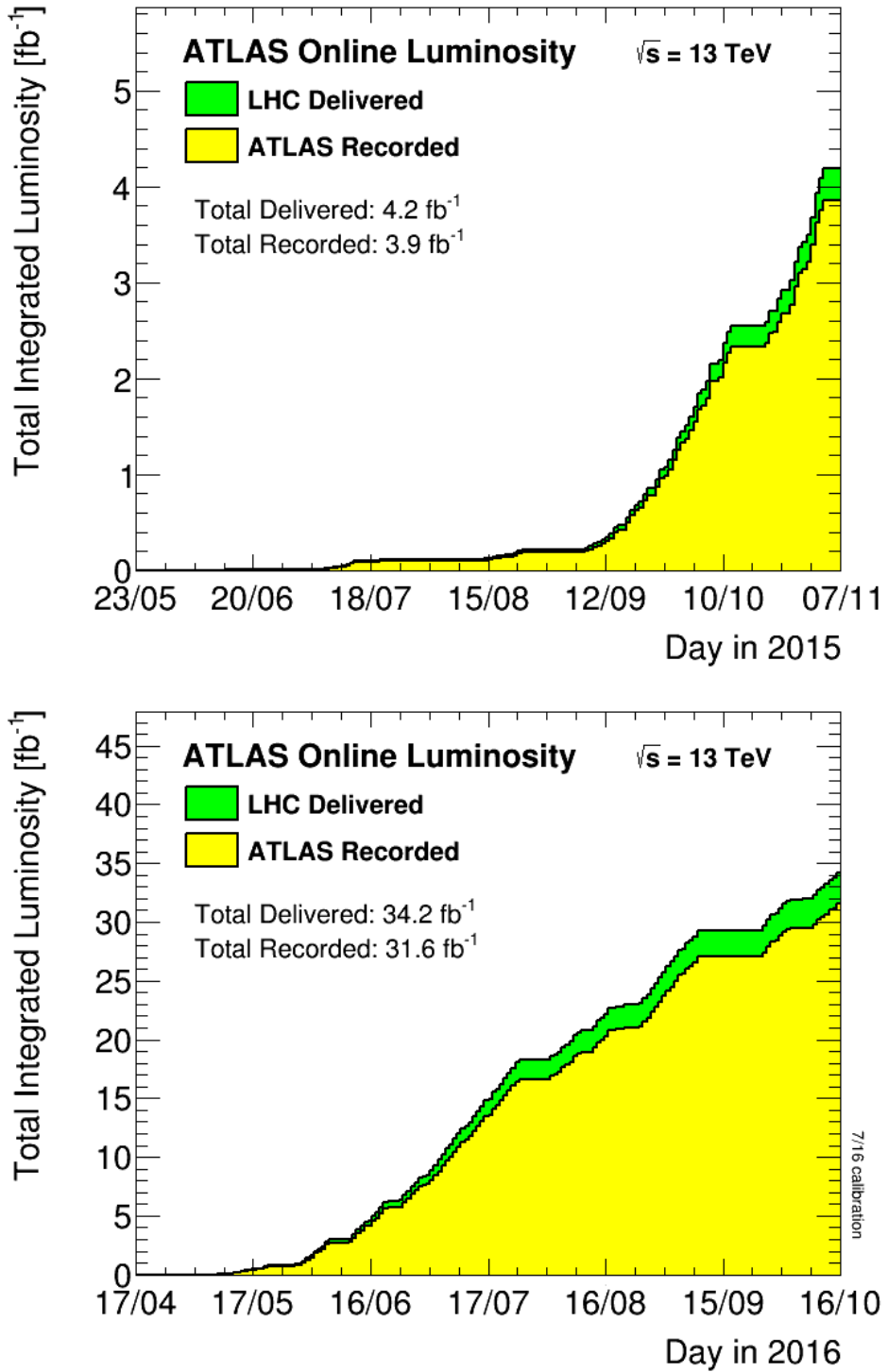


Figure 4.4: Integrated Luminosity delivered by the LHC and collected by ATLAS in the 2015 and 2016 datasets.

Parameter	Injection	Extraction
Energy (GeV)	450	7000
Rigidity (T-m)	3.8	23353
Bunch spacing (ns)	25	25
Design Luminosity ($\text{cm}^{-2}\text{s}^{-1} \times 10^3$)	-	1.0
Bunches per proton beam	2808	2808
Protons per bunch	1.15 e11	1.15 e11
Beam lifetime (hr)	-	10
Normalized Emittance ϵ_N (mm μrad)	3.3	3.75
Betatron function at collision point β^* (cm)	-	55

Table 4.1: Beam parameters of the Large Hadron Collider.

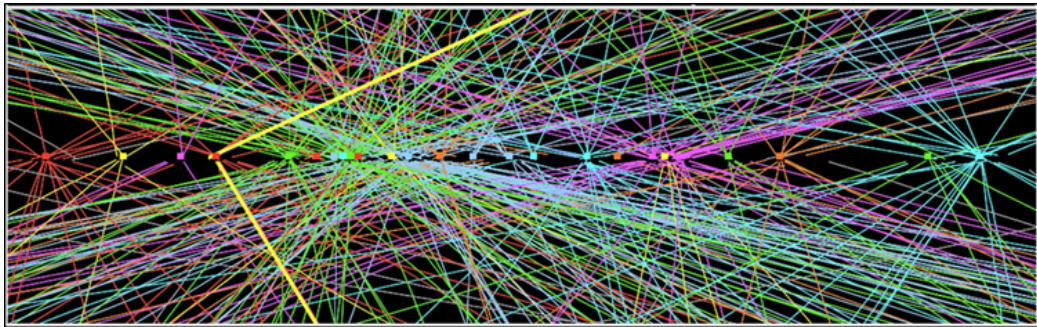


Figure 4.5: Simulated event with many pileup vertices.

634 Pileup

635 *Pileup* is the term for the additional proton-proton interactions which occur during
 636 each bunch crossing of the LHC. At the beginning of the LHC physics program, there
 637 had not been a collider which averaged more than a single interaction per bunch
 638 crossing. In the LHC, each bunch crossing (or *event*) generally contains multiple
 639 proton-proton interactions. An simulated event with many *vertices* can be seen in
 640 Fig.4.5. The so-called *primary vertex* (or *hard scatter vertex*) refers to the vertex
 641 which has the highest Σp_T^2 ; this summation occurs over the *tracks* in the detector,
 642 which we will describe later[**ATL-INDET-PUB-2009-001**]. We then distinguish
 643 between *in-time* pileup and *out-of-time* pileup. In-time pileup refers to the additional
 644 proton-proton interactions which occur in the event. Out-of-time pileup refers to
 645 effects related to proton-proton interactions previous bunch crossings.

646 We quantify in-time pileup by the number of “primary”² vertices in a particular
647 event. To quantify the out-of-time pileup, we use the average number of interactions
648 per bunch crossing $\langle \mu \rangle$ over some human-scale time. In Figure 4.6, we show the
649 distribution of μ for the dataset used in this thesis.

²The primary vertex is as defined above, but we unfortunately use the same name here.



Figure 4.6: Mean number of interactions per bunch crossing in the 2015 and 2016 datasets.

The ATLAS detector

652 The dataset analyzed in this thesis was taken by the ATLAS detector [88], which is
 653 located at the “Point 1” cavern of the LHC beampipe, just across the street from
 654 the main CERN campus. The much-maligned acronym stands for *A Toroidal LHC*
 655 *ApparatuS*. ATLAS is a massive cylindrical detector, with a radius of 12.5 m and a
 656 length of 44 m, with nearly hermitic coverage around the collision point. It consists
 657 of multiple subdetectors; each plays a role in ATLAS’s ultimate purpose of measuring
 658 the energy, momentum, and type of the particles produced in collisions delivered by
 659 the LHC. These subdetectors are immersed in a hybrid solenoid-toroid magnet system
 660 whichs forces charged particles to curve, which allows for precise measurements of
 661 their momenta. These magnetic fields are maximized in the central solenoid magnet,
 662 which contains a magnetic field of 2 T. A schematic of the detector can be seen in
 663 [5.1](#).

664 The *inner detector* (ID) lies closest to the collision point, and contains three
 665 separate subdetectors. It provides pseudorapidity¹coverage of $|\eta| < 2.5$ for charged
 666 particles to interact with the tracking material. The tracks reconstructed from the
 667 inner detector hits are used to reconstruct the primary vertices, as noted in Ch.??,

¹ATLAS uses a right-handed Cartesian coordinate system; the origin is defined by the nominal beam interaction point. The positive- z direction is defined by the incoming beam travelling counterclockwise around the LHC. The positive- x direction points towards the center of the LHC ring from the origin, and the positive- y direction points upwards towards the sky. For particles of transverse (in the $x - y$ plane) momentum $p_T = \sqrt{p_x^2 + p_y^2}$ and energy E , it is generally most convenient fully describe this particle’s kinematics as measured by the detector in the (p_T, ϕ, η, E) basis. The angle $\phi = \arctan(p_y/p_x)$ is the standard azimuthal angle, and $\eta = \ln \tan(\theta/2)$ is known as the pseudorapidity, and defined based on the standard polar angle $\theta = \arccos(p_z/p_T)$. For locations of i.e. detector elements, both (r, ϕ, η) and (z, ϕ, η) can be useful.



Figure 5.1: The ATLAS detector

and to determine the momenta of charged particles. The ATLAS *calorimeter* consists of two subdetectors, known as the *electromagnetic* and *hadronic* calorimeters. These detectors stop particles in their detector material, and measure the energy deposition inside, which measures the energy of the particles deposited. The calorimeters provide coverage out to pseudorapidity of $|\eta| < 4.9$. The muon spectrometer is aptly named; it is specifically used for muons, which are the only particles which generally reach the outer portions of the detector. In this region, we have the large tracking systems of the muon spectrometer, which provide precise measurements of muon momenta. The muon spectrometer has pseudorapidity coverage of $|\eta| < 2.7$.

5.1 Magnets

ATLAS contains multiple magnetic systems; primarily, we are concerned with the solenoid, used by the inner detector, and the toroids located outside of the ATLAS calorimeter. A schematic is shown in Fig.5.2. These magnetic fields are used to bend

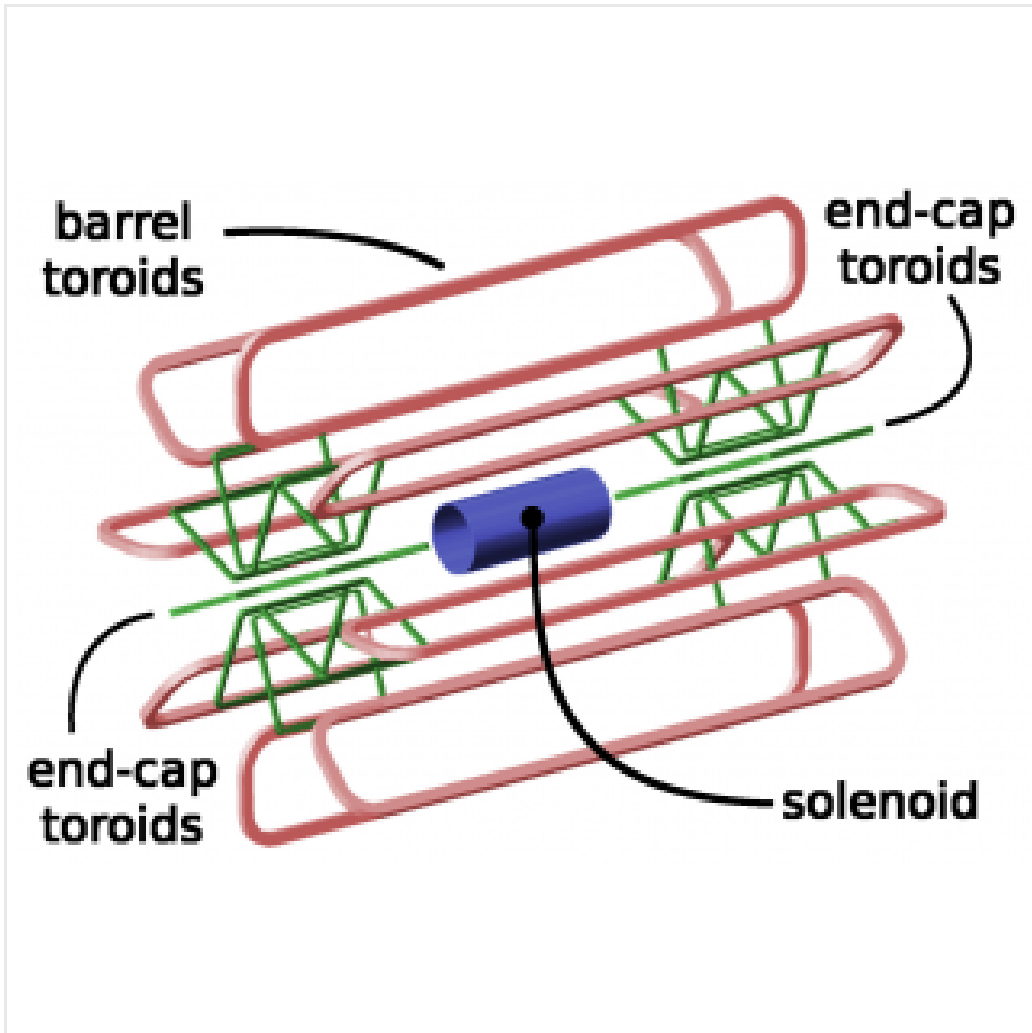


Figure 5.2: The ATLAS magnet system

681 charged particles under the Lorentz force, which subsequently allows one to measure
682 their momentum.

683 The ATLAS central solenoid is a 2.3 m diameter, 5.3 m long solenoid at the center
684 of the ATLAS detector. It produces a uniform magnetic field of 2 T; this strong field
685 is necessary to accurately measure the charged particles in this field. An important
686 design constraint for the central solenoid was the decision to place it in between the
687 inner detector and the calorimeters. To avoid excessive impacts on measurements in
688 the calorimetry, the central solenoid must be as transparent as possible².

²This is also one of the biggest functional differences between ATLAS and CMS; in CMS, the



Figure 5.3: The ATLAS inner detector

689 The toroid system consists of eight air-core superconducting barrel loops; these
 690 give ATLAS its distinctive shape. There are also two endcap air-core magnets. These
 691 produce a magnetic field in a region of approximately 26 m in length and 10 m of
 692 radius. The magnetic field in this region is non-uniform, due to the prohibitive costs
 693 of a solenoid magnet of that size.

694 **5.2 Inner Detector**

695 The ATLAS inner detector consists of three separate tracking detectors, which are
 696 known as, in order of increasing distance from the interaction point, the Pixel
 697 Detector, Semiconductor Tracker (SCT), and the Transition Radiation Tracker
 698 (TRT). When charged particles pass through these tracking layers, they produce
 699 *hits*, which using the known 2 T magnetic field, allows the reconstruction of *tracks*.
 700 Tracks are used as inputs for reconstruction of many higher-level physics objects,

solenoid is outside of the calorimeters.

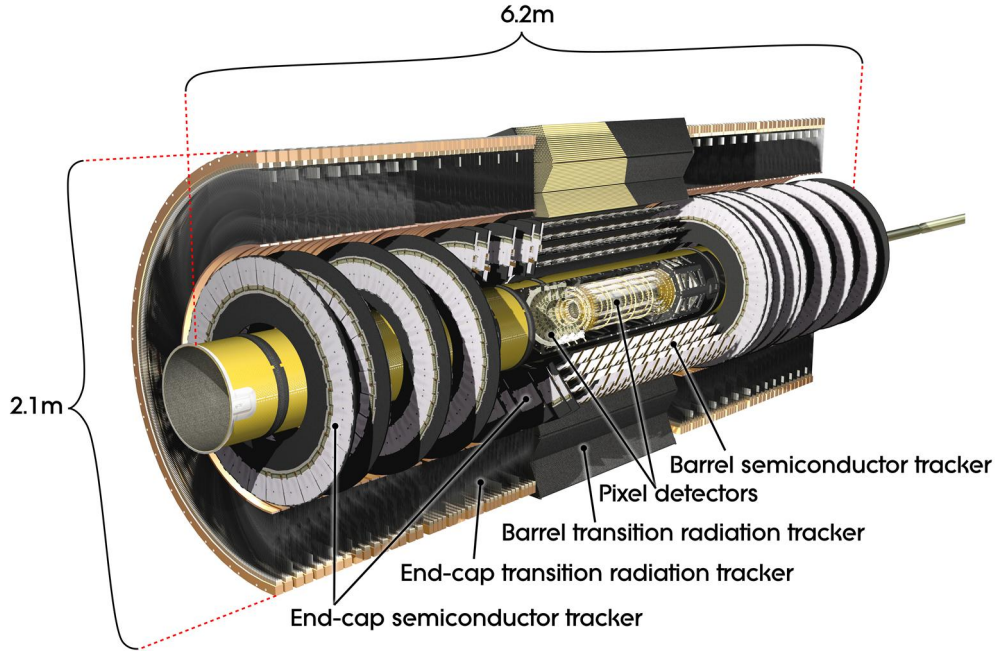


Figure 5.4: The ATLAS pixel detector

701 such as electrons, muons, photons, and E_T^{miss} . Accurate track reconstruction is thus
 702 crucial for precise measurements of charged particles.

703 Pixel Detector

704 The ATLAS pixel detector consists four layers of silicon “pixels”. This refers to the
 705 segmentation of the active medium into the pixels; compare to the succeeding silicon
 706 detectors, which will use silicon “strips”. This provides precise 3D hit locations. The
 707 layers are known as the “Insertable”³B-Layer (IBL), the B-Layer (or Layer-0), Layer-
 708 1, and Layer-2, in order of increasing distance from the interaction point. These
 709 layers are very close to the interaction point, and therefore experience a large amount
 710 of radiation.

711 Layer-1, Layer-2, and Layer-3 were installed with the initial construction of
 712 ATLAS. They contain front-end integrated electronics (FEI3s) bump-bonded to 1744

³Very often, the IBL is mistakenly called the Inner B-Layer, which would have been a much more sensible name.

713 silicon modules; each module is $250\ \mu\text{m}$ in thickness and contains 47232 pixels. These
714 pixels have planar sizes of $50 \times 400\ \mu^2$ or $50 \times 600\ \mu^2$, to provide highly accurate
715 location information. The FEI3s are mounted on long rectangular structures known
716 as staves, which encircle the beam pipe. A small tilt to each stave allows full coverage
717 in ϕ even with readout systems which are installed. These layers are at radia of 50.5
718 mm, 88.5 mm, and 122.5 mm from the interaction point.

719 The IBL was added to ATLAS after Run1 in 2012 at a radius of 33 mm from the
720 interaction point. The entire pixel detector was removed from the center of ATLAS
721 to allow an additional pixel layer to be installed. The IBL was required to preserve
722 the integrity of the pixel detector as radiation damage leads to inoperative pixels in
723 the other layers. The IBL consists of 448 FEI4 chips, arranged onto 14 staves. Each
724 FEI4 has 26880 pixels, of planar size $50 \times 250\ \mu\text{m}$. This smaller granularity was
725 required due to the smaller distance to the interaction point.

726 In total, a charged particle passing through the inner detector would expect to
727 leave four hits in the pixel detector.

728 Semiconductor Tracker

729 The SCT is directly beyond Layer-2 of the pixel detector. This is a silicon strip
730 detector, which do not provide the full 3D information of the pixel detector. The
731 dual-sensors of the SCT contain 2×768 individual strips; each strip has area $6.4\ \text{cm}^2$.
732 The SCT dual-sensor is then double-layered, at a relative angle of 40 mrad;
733 together these layers provide the necessary 3D information for track reconstruction.
734 There are four of these double-layers, at radia of 284 mm, 355 mm, 427 mm, and 498
735 mm. These double-layers provide hits comparable to those of the pixel detector, and
736 we have four additional hits to reconstruct tracks for each charged particle.

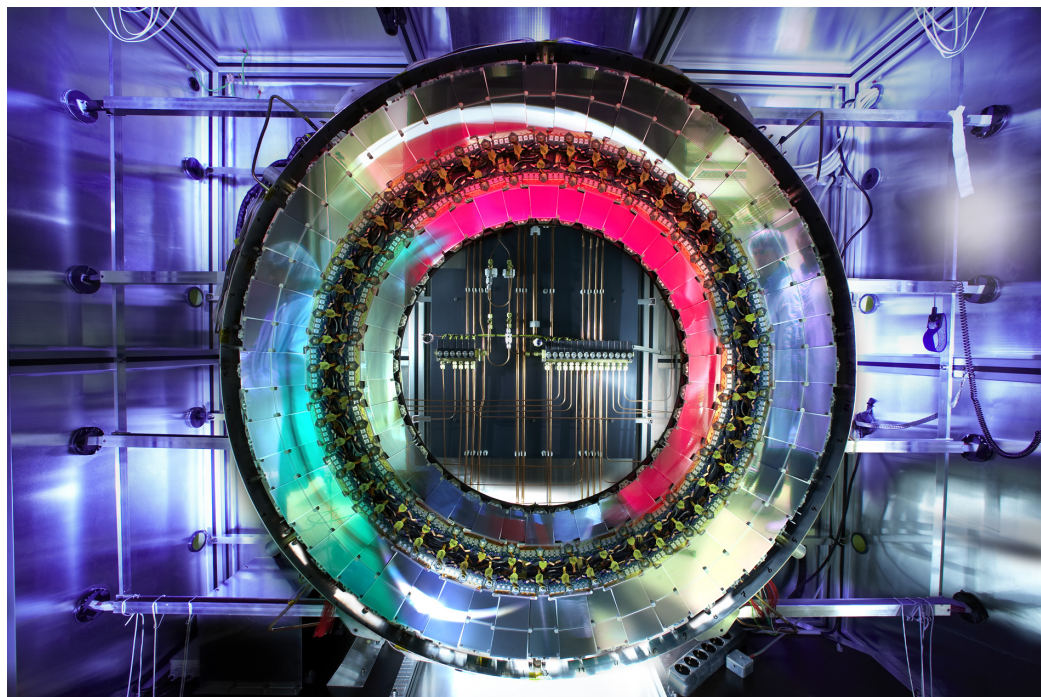


Figure 5.5: A ring of the Semiconductor Tracker

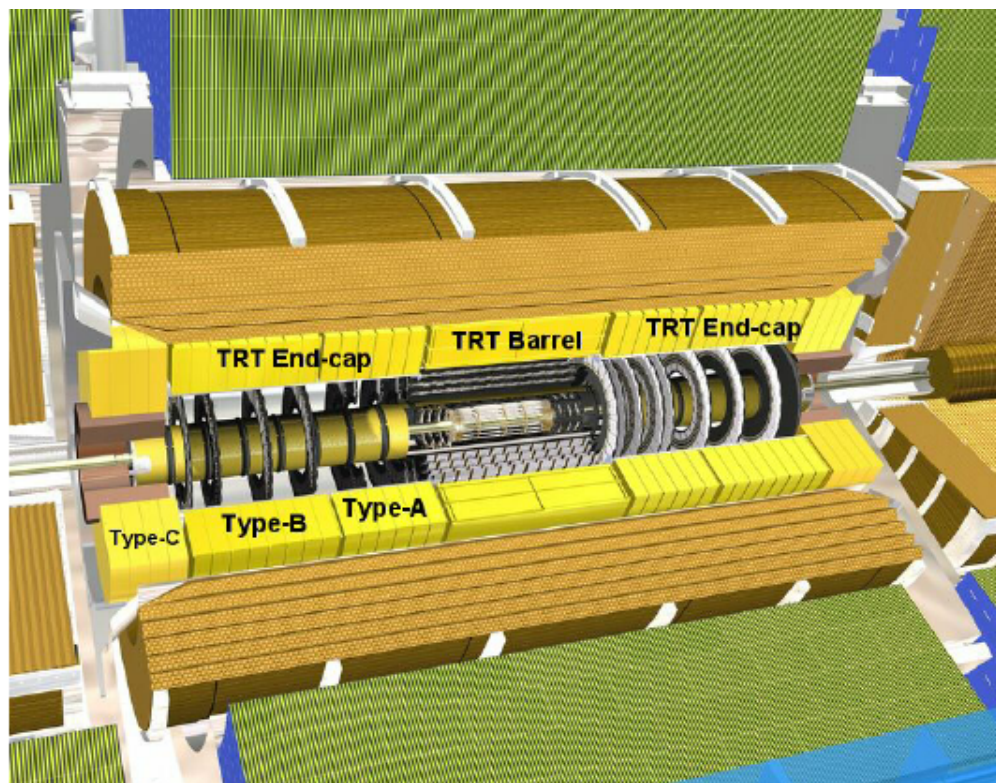


Figure 5.6: A schematic of the Transition Radiation Tracker

737 **Transition Radiation Tracker**

738 The Transition Radiation Tracker is the next detector radially outward from the SCT.
739 It contains straw drift tubes; these contain a tungsten gold-plated wire of $32\ \mu\text{m}$
740 diameter held under high voltage (-1530 V) with the edge of the Kapton-aluminum
741 tube. They are filled with a gas mixture of primarily xenon that is ionized when
742 a charged particle passes through the tube. The ions are collected by the “drift”
743 due to the voltage inside the tubes, which is read out by the electronics. This gives
744 so-called “continuous tracking” throughout the tube, due to the large number of ions
745 produced.

746 The TRT is so-named due to the *transition radiation* (TR) it induces. Due to
747 the dielectric difference between the gas and tubes, TR is induced. This is important
748 for distinguishing electrons from their predominant background of minimum ionizing
749 particles. Generally, electrons have a much larger Lorentz factor than minimum
750 ionizing particles, which leads to additional TR. This can be used as an additional
751 handle for electron reconstruction.

752 **5.3 Calorimetry**

753 The calorimetry of the ATLAS detector also includes multiple subdetectors; these sub-
754 detectors allow precise measurements of the electrons, photons, and hadrons produced
755 by the ATLAS detector. Generically, calorimeters work by stopping particles in their
756 material, and measuring the energy deposition. This energy is deposited as a cascade
757 particles induce from interactions with the detector material known *showers*. ATLAS
758 uses *sampling* calorimeters; these alternate a dense absorbing material, which induces
759 showers, with an active layer which measures energy depositions by the induced
760 showers. Since some energy is deposited into the absorption layers as well, the energy
761 depositions must be properly calibrated for the detector.

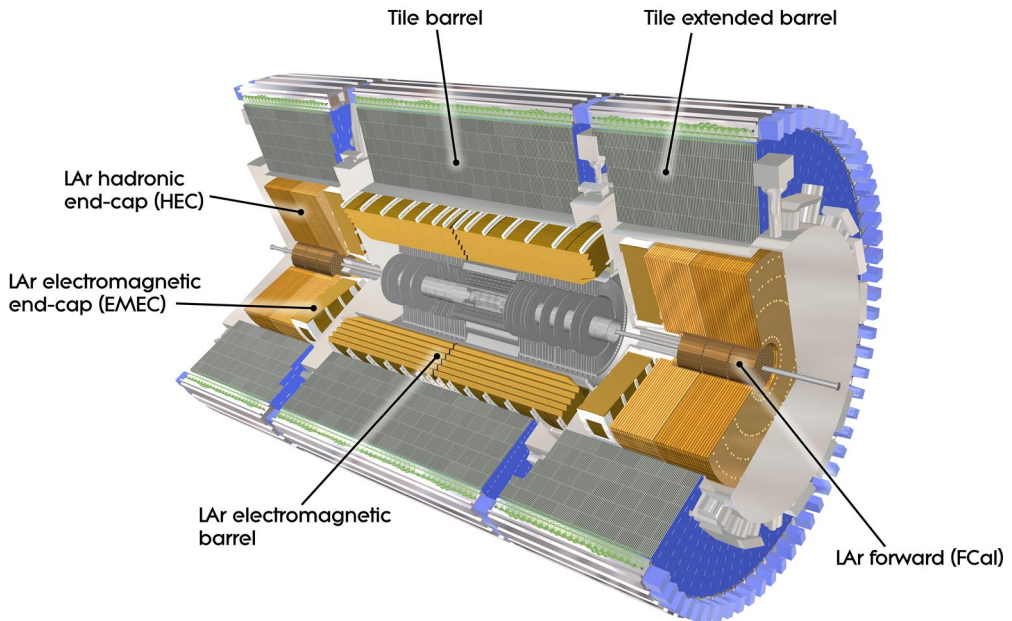


Figure 5.7: The ATLAS calorimeter

762 Electromagnetic objects (electrons and photons) and hadrons have much different
 763 interaction properties, and thus we need different calorimeters to accurately measure
 764 these different classes of objects; we can speak of the *electromagnetic* and *hadronic*
 765 calorimeters. ATLAS contains four separate calorimeters : the liquid argon (LAr)
 766 electromagnetic barrel calorimeter, the Tile barrel hadronic calorimeter, the LAr
 767 endcap electromagnetic calorimeter, the LAr endcap hadronic calorimeter, and the
 768 LAr Forward Calorimeter (FCal). Combined, these provide full coverage in ϕ up to
 769 $|\eta| < 4.9$, and can be seen in Fig.5.7.

770 **Electromagnetic Calorimeters**

771 The electromagnetic calorimeters of the ATLAS detector consist of the barrel and
 772 endcap LAr calorimeters. These are arranged into an ingenious “accordion” shape,
 773 shown in 5.8, which allows full coverage in ϕ and exceptional coverage in η while
 774 still allowing support structures for detector operation. The accordion is made of



Figure 5.8: A schematic of a subsection of the barrel LAr electromagnetic calorimeter

775 layers with liquid argon (active detection material) and lead (absorber) to induce
 776 electromagnetic showers. The LAr EM calorimeters are each more than 20 radiation
 777 lengths deep, which provides the high stopping power necessary to properly measure
 778 the electromagnetic showers.

779 The barrel component of the LAr EM calorimeter extends from the center of the
 780 detector out to $|\eta| < 1.475$. The calorimeter has a presampler, which measures the
 781 energy of any EM shower induced before the calorimeter. This has segmentation of
 782 $\Delta\eta = 0.025, \Delta\phi = .01$. There are three “standard” layers in the barrel, which have
 783 decreasing segmentation into calorimeter *cells* as one travels radially outward from
 784 the interaction point. The first layer has segmentation of $\Delta\eta = 0.003, \Delta\phi = .1$, and
 785 is quite thin relative to the other layers at only 4 radiation lengths deep. It provides
 786 precise η and ϕ measurements for incoming EM objects. The second layer is the
 787 deepest at 16 radiation lengths, with a segmentation of $\Delta\eta = 0.025, \Delta\phi = 0.025$. It



Figure 5.9: A schematic of Tile hadronic calorimeter

788 is primarily responsible for stopping the incoming EM particles, which dictates its
 789 large relative thickness, and measures most of the energy of the incoming particles.
 790 The third layer is only 2 radiation lengths deep, with a rough segmentation of $\Delta\eta =$
 791 0.05 , $\Delta\phi = .025$. The deposition in this layer is primarily used to distinguish hadrons
 792 interacting electromagnetically and entering the hadronic calorimeter from the strictly
 793 EM objects which are stopped in the second layer.

794 The barrel EM calorimeter has a similar overall structure, but extends from
 795 $1.4 < |\eta| < 3.2$. The segmentation in η is better in the endcap than the barrel;
 796 the ϕ segmentation is the same. In total, the EM calorimeters contain about 190000
 797 individual calorimeter cells.

798 Hadronic Calorimeters

799 The hadronic calorimetry of ATLAS sits directly outside the EM calorimetry. It
 800 contains three subdetectors : the barrel Tile calorimeter, the endcap LAr calorimeter,

801 and the Forward LAr Calorimeter. Similar to the EM calorimeters, these are
802 sampling calorimeters that alternate steel (dense material) with an active layer
803 (plastic scintillator).

804 The barrel Tile calorimeter extends out to $|\eta| < 1.7$. There are again three layers,
805 which combined give about 10 interactions length of distance, which provides excellent
806 stopping power for hadrons. This is critical to avoid excess *punchthrough* to the muon
807 spectrometer beyond the hadronic calorimeters. The first layer has a depth of 1.5
808 interaction lengths. The second layer is again the thickest at a depth of 4.1 interaction
809 lengths; most of the energy of incoming particle is deposited here. Both the first and
810 second layer have segmentation of about $\Delta\eta = 0.1, \Delta\phi = 0.1$. Generally, one does not
811 need as fine of granularity in the hadronic calorimeter, since the energy depositions
812 in the hadronic calorimeters will be summed into the composite objects we know as
813 jets. The third layer has a thickness of 1.8 interaction lengths, with a segmentation of
814 $\Delta\eta = 0.2, \Delta\phi = 0.1$. The use of multiple layers allows one to understand the induced
815 hadronic shower as it propagates through the detector material.

816 The endcap LAr hadronic calorimeter covers the region $1.5 < |\eta| < 3.2$. It is
817 again a sampling calorimeter; the active material is LAr with a copper absorbed. It
818 does not use the accordion shape of the other calorimeters; it has a “standard” flat
819 shape perpendicular to the interaction point. The segmentation varies with η . For
820 $1.5 < |\eta| < 2.5$, the cells are $\Delta\eta = 0.1, \Delta\phi = 0.1$; in the region $2.5 < |\eta| < 3.2$, the
821 cells are $\Delta\eta = 0.2, \Delta\phi = 0.2$ in size.

822 The final calorimeter in ATLAS is the forward LAr calorimeter. Of those
823 subdetectors which are used for standard reconstruction techniques, the FCal sits
824 at the most extreme values of $3.1 < |\eta| < 4.9$. The FCal itself is made of three
825 subdetectors; FCal1 is actually an electromagnetic module, while FCal2 and FCal3
826 are hadronic. The absorber in FCal1 is copper, with a liquid argon active medium.
827 FCal2 and FCal3 also use a liquid argon active medium, with a tungsten absorber.

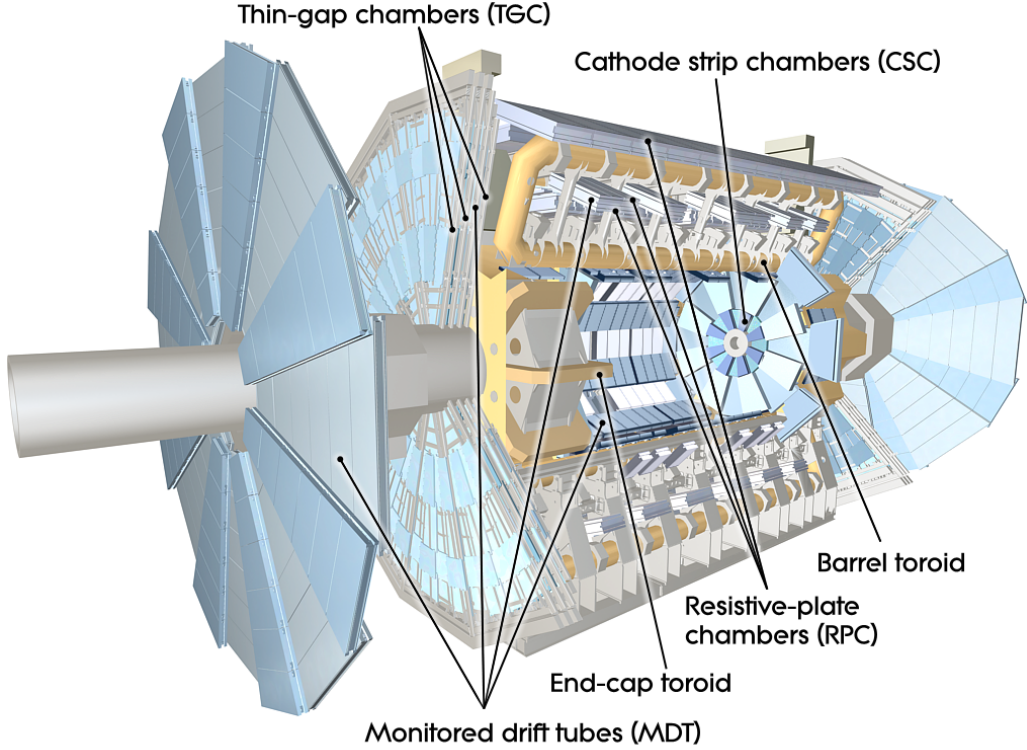


Figure 5.10: The ATLAS muon spectrometer

828 5.4 Muon Spectrometer

829 The muon spectrometer is the final major subdetector of the ATLAS detector.
830 The muon spectrometer sits outside the hadronic calorimetry, with pseudorapidity
831 coverage out to $|\eta| < 2.7$. The MS is a huge detector, with some detector elements
832 existing as far as 11 m in radius from the interaction point. This system is used
833 almost exclusively to measure the momenta of muons; these are the only measured
834 SM particles which consistently exit the hadronic calorimeters. These systems provide
835 a rough measurement, which is used in triggering (described in Ch.5.5), and a precise
836 measurement to be used in offline event reconstruction as described in Ch.???. The
837 MS produces tracks in a similar way to the ID; the hits in each subdetector are
838 recorded and then tracks are produced from these hits. Muon spectrometer tracks are
839 largely independent of the ID tracks due to the independent solenoidal and toroidal
840 magnet systems used in the ID and MS respectively. The MS consists of four separate

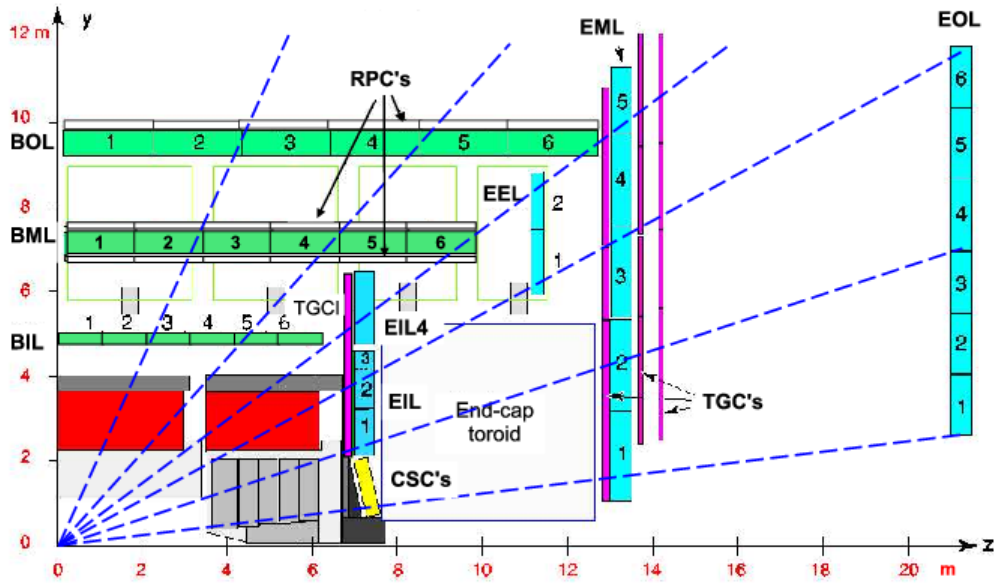


Figure 5.11: A schematic in z/η showing the location of the subdetectors of the muon spectrometer

841 subdetectors: the barrel region is covered by the Resistive Plate Chambers (RPCs)
 842 and Monitored Drift Tubes (MDTs) while the endcaps are covered by MDTs, Thin
 843 Gap Chambers (TGCs), and Cathode Strip Chambers (CSCs).

844 Monitored Drift Tubes

845 The MDT system is the largest individual subdetector of the MS. MDTs provide
 846 precision measurements of muon momenta as well as fast measurements used for
 847 triggers. There are 1088 MDT chambers providing coverage out to pseudorapidity
 848 $|\eta| < 2.7$; each consists of an aluminum tube containing an argon- CO_2 gas mixture.
 849 In the center of each tube there $50\mu\text{m}$ diameter tungsten-rhenium wire at a voltage of
 850 3080 V. A muon entering the tube will induce ionization in the gas, which will “drift”
 851 towards the wire due to the voltage. One measures this ionization as a current in the
 852 wire; this current comes with a time measurement related to how long it takes the
 853 ionization to drift to the wire.

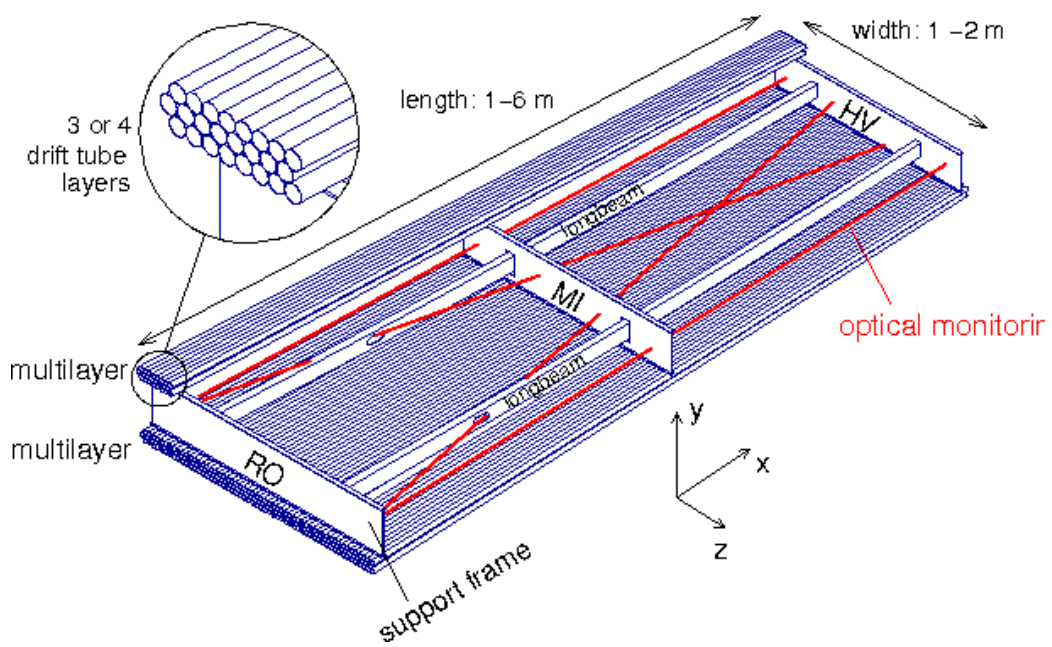


Figure 5.12: Schematic of a Muon Drift Tube chamber

854 These tubes are layered in a pattern shown in Fig.5.12. Combining the measure-
855 ments from the tubes in each layer gives good position resolution. The system consists
856 of three subsystems of these layers, at 5 m, 7m, and 9 m from the interaction point.
857 The innermost layer is directly outside the hadronic calorimeter. The combination of
858 these three measurements gives precise momenta measurements for muons.

859 **Resistive Plate Chambers**

860 The RPC system is alternated with the MDT system in the barrel; the first two layers
861 of RPC detectors surround the second MDT layer while the third is outside the final
862 MDT layer. The RPC system covers pseudorapidity $|\eta| < 1.05$. Each RPC consists
863 of two parallel plates at a distance of 2 mm surrounding a $\text{C}_2\text{H}_2\text{F}_4$ mixture. The
864 electric field between these plates is 4.9k kV/mm. Just as in the MDTs, an incoming
865 muon ionizes the gas, and the deposited ionization is collected by the detector (in this
866 case on the plates). It is quite fast, but with a relatively poor spatial resolution of
867 1 cm. Still, it can provide reasonable ϕ resolution due to its large distance from the
868 interaction point. This is most useful in triggering, where the timing requirements are
869 quite severe. The RPCs are also complement the MDTs by providing a measurement
870 of the non-bending coordinate.

871 **Cathode Strip Chambers**

872 The CSCs are used in place of MDTs in the first layer of the endcaps. This region, at
873 $2.0 < |\eta| < 2.7$, has higher particle multiplicity at the close distance to the interaction
874 point from low-energy photons and neutrons. The MDTs were not equip to deal with
875 the higher particle rate of this region, so the CSCs were designed to deal with this
876 deficiency.

877 Each CSC consists multiwire proportional chambers, oriented radially outward
878 from the interaction point. These chambers overlap partially in ϕ . The wires contain



Figure 5.13: Photo of the installation of Cathode Strip Chambers and Monitored Drift Tubes

879 a gas mixture of argon and CO₂, which is ionized when muons enter. The detectors
880 operate with a voltage of 1900 V, with much lower drift times than the MDTs. They
881 provide less hits than MDTs, but their lower drift times lower uptime and reduce the
882 amount of detector overload.

883 The CSCs are arranged into four planes on the wheels of the muon spectrometer,
884 as seen in Fig.???. There are 32 CSCs in total, with 16 on each side of the detector
885 in η .

886 **Thin Gap Chambers**

887 The TGCs serve the purpose of the RPCs in the endcap at pseudorapidity of $1.05 <$
888 $|\eta| < 2.4$; they provide fast measurements used in triggering. The TGCs are also
889 multiwire proportional chambers a la the CSCs. The fast readouts necessary for
890 trigger are provided by a high electric field and a small wire-to-wire distance of 1.8
891 mm. These detectors provide both η and ϕ information, allowing the trigger to use
892 as much information as possible when selecting events.



Figure 5.14: Photo of a muon Big Wheel, consisting of Thin Gap Chambers

893 5.5 Trigger System

894 The data rate delivered by the LHC is staggering [89]. In the 2016 dataset, the
895 collision rate was 40 MHz, meaning a *bunch spacing* of 25 ns. In each of the event,
896 as we saw in Ch.??, there are many proton-proton collisions. Most of the collisions
897 are uninteresting, such as elastic scattering of protons, or even inelastic scattering
898 leading to low-energy dijet events. These types of events have been studied in detail
899 in previous experiments.

900 Even if one is genuinely interested in these events, it's *impossible* to save all of
901 the information available in each event. If all events were written "to tape" (as the
902 jargon goes), ATLAS would store terabytes of data per second. We are limited to only
903 about 1000 Hz readout by computing processing time and storage space. We thus
904 implement a *trigger* which provides fast inspection of events to drastically reduce
905 the data rate from the 40 MHz provided by the LHC to the 1000 Hz we can write to
906 tape for further analysis.

907 The ATLAS trigger system consists of a two-level trigger, known as the Level-
908 1 trigger (L1 trigger) and the High-Level Trigger (HLT)⁴. Trigger selections are
909 organized into *trigger chains*, where events passing a particular L1 trigger are passed
910 to a corresponding HLT trigger. For example, one would require a particular high- p_T
911 muon at L1, with additional quality requirements at HLT. One can also use HLT
912 triggers as prerequisites for each other, as is done in some triggers requiring both jets
913 and E_T^{miss} .

914 **Level-1 Trigger**

915 The L1 trigger is hardware-based, and provides the very fast rejection needed to
916 quickly select events of interest. The L1 trigger uses only what is known as *prompt*
917 data to quickly identify interesting events. Only the calorimeters and the triggering
918 detectors (RPCs and TGCs) of the MS are fast enough to be considered at L1,
919 since the tracking reconstruction algorithms used by the ID and the more precise
920 MS detectors are very slow. This allows quick identification of events with the
921 most interesting physical objects : large missing transverse momentum and high-
922 p_T electrons, muons, and jets.

923 L1 trigger processing is done locally. This means that events are selected without
924 considering the entire available event. Energy deposits over some threshold are
925 reconstructed as *regions of interest*. These RoIs are then compared using pattern
926 recognition hardware to “expected” patterns for the given RoIs. Events with RoIs
927 matching these expected patterns are then handed to the HLT through the Central
928 Trigger Processor. This step alone lowers the data rate down by about three orders
929 of magnitude.

⁴In Run1, ATLAS ran with a three-level trigger system. The L1 was essentially as today; the HLT consisted of two separate systems known as the L2 trigger and the Event Filter (EF). This was changed to the simpler system used today during the shutdown between Run1 and Run2.

930 **High-Level Trigger**

931 The HLT performs the next step, taking the incoming data rate from the L1 trigger
932 of ~ 75 kHz down to the ~ 1 kHz that can be written to tape. The HLT really
933 performs much like a simplified offline reconstruction, using many common quality
934 and analysis cuts to eliminate uninteresting events. This is done by using computing
935 farms located close to the detector, which process events in parallel. Individually, each
936 event which enters the computing farms takes about 4 seconds to reconstruct; the
937 HLT reconstruction time also has a long tail, which necessitates careful monitoring
938 of the HLT to ensure smooth operation.

939 HLT triggers are targetted to a particular physics process, such as a E_T^{miss} trigger,
940 single muon trigger, or multijet trigger. The collection of all triggers is known as
941 the trigger *menu*. Since many low-energy particles are produced in collisions, it is
942 necessary to set a *trigger threshold* on the object of interest; this is really just a fancy
943 naming for a trigger p_T cut. Due to the changing luminosity conditions of the LHC,
944 these thresholds change constantly, mostly by increasing thresholds with increasing
945 instantaneous luminosity. This allows an approximately constant number of events to be
946 written for further analysis. Triggers which have rates higher than those designated
947 by the menu are *prescaled*. This means writing only some fraction of the triggered
948 events. Of course, for physics analyses, one wishes to investigate all data events
949 passing some set of analysis cuts, so often one uses the “lowest threshold unprescaled
950 trigger”. *Turn-on curves* allow one to select the needed offline analysis cut to ensure
951 the trigger is fully efficient. An example turn-on curve for the E_T^{miss} triggers used in
952 the signal region of this analysis is shown in ??.

953 The full set of the lowest threshold unprescaled triggers considered here can be
954 found in Table 5.1. These are the lowest unprescaled triggers associated to the SUSY
955 signal models and Standard Model backgrounds considered in this thesis. More
956 information can be found in [89].

Physics Object	Trigger	p_T (GeV)	Threshold	Level-1 Seed	Additional Requirements	Approximate Rate (Hz)
2015 Data						
E_T^{miss}	HLT_xe70	70	L1_XE50	-	60	
Muon	HLT_mu24_iloose_L1MU15	50	L1_MU15	isolated, loose	130	
Muon	HLT_mu50	50	L1_MU15	-	30	
Electron	HLT_e24_1hmedium_llbase_L1EM20VH		L1_EM20VH	medium OR isolated, loose	140	
Electron	HLT_e60_1hmedium	60	L1_EM20VH	medium	10	
Electron	HLT_e120_1hloose	120	L1_EM20VH	loose	<10	
Photon	HLT_g120_loose	120	L1_EM20VH	loose	20	
2016 Data						
E_T^{miss}	HLT_xe100_mht_L1XE5000		L1_XE50	-	180	
Muon	HLT_mu24_ivarmedium4		L1_MU20	medium	120	
Muon	HLT_mu50	50	L1_MU20	-	40	
Electron	HLT_e24_ltight_noD1_ivarloose		L1_EM22VHI	tight with no d_0 or loose	110	
Electron	HLT_e60_1hmedium_nd60		L1_EM22VHI	medium with no d_0	10	
Electron	HLT_e140_1hloose_noD0		L1_EM22VHI	loose with no d_0	<10	
Photon	HLT_g140_loose	140	L1_EM22VHI	loose	20	

Table 5.1: High-Level Triggers used in this thesis. Descriptions of loose, medium, tight, and isolated can be found in [89]. The d_0 cut refers to a quality cut on the vertex position; this was removed from many triggers in 2016 to increase sensitivity to displaced vertex signals. For most triggers, the increased thresholds in 2016 compared to 2016 were designed to keep the rate approximately equal. The exception is the E_T^{miss} triggers; see 5.5.

957 **Razor Triggers**

958 For the analysis presented in this thesis, the *razor triggers* were developed. These are
959 topological triggers, combining both jet and E_T^{miss} information to select interesting
960 events. In particular, they use the razor variable M_{Δ}^R which will be described in
961 Chapter ??.

962 Based on 2015 run conditions, these triggers would have allowed the use of a lower
963 offline E_T^{miss} cut with a similar rate to the nominal E_T^{miss} triggers. This can be seen
964 in the turn-on curves shown in Figure 5.15. The razor triggers are fully efficient at
965 nearly 100 GeV lower than the corresponding E_T^{miss} triggers in M_{Δ}^R .

966 There was a quite big change in the 2016 menu, which increased the rate given to
967 E_T^{miss} triggers drastically. This can be seen in the difference in rate shown between
968 E_T^{miss} triggers in 2015 and 2016 in Table 5.1. This allowed the E_T^{miss} triggers to
969 maintain a lower threshold throughout the dataset used in this thesis.

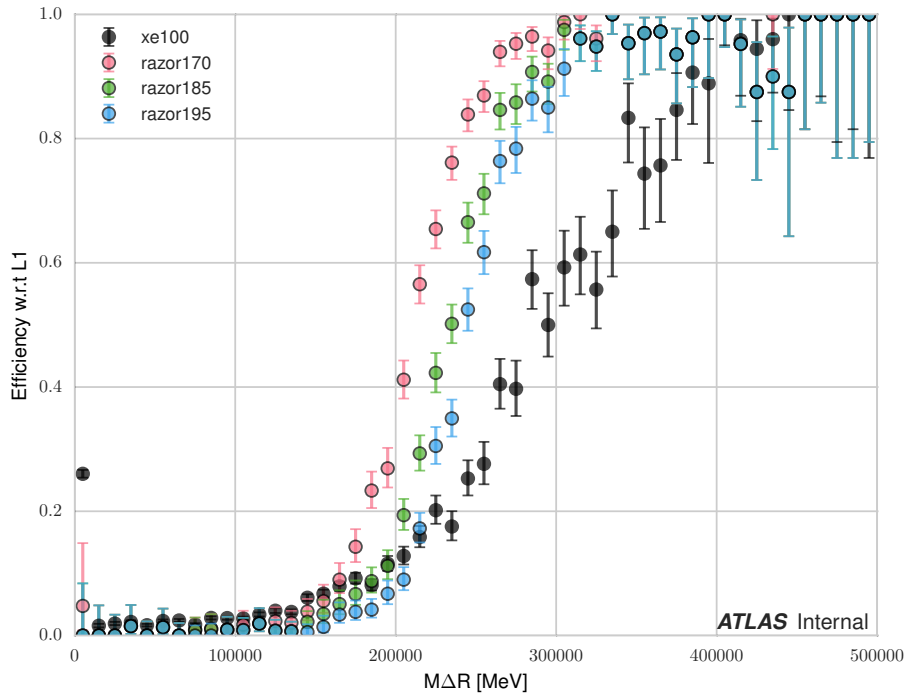
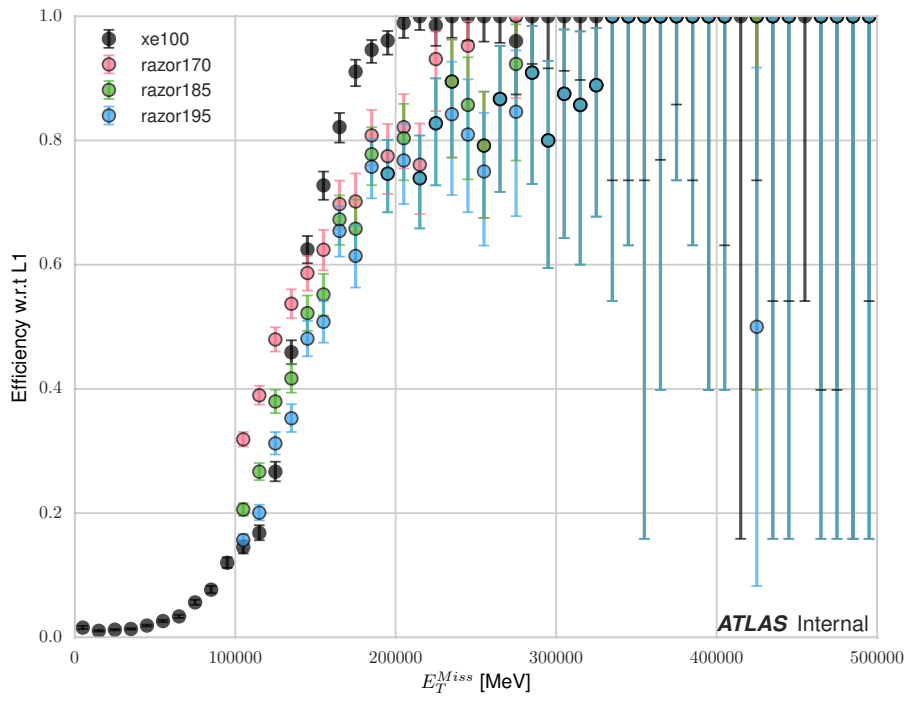


Figure 5.15: Turn-on curves for the razor triggers and nominal E_T^{miss} trigger. The razor triggers show a much sharper turn-on in M_{Δ}^R relative to the E_T^{miss} trigger. The converse is true for the E_T^{miss} triggers.

Object Reconstruction

972 This chapter describes the reconstruction algorithms used within ATLAS. We will
973 make the distinction between the “primitive” objects which are reconstructed from
974 the detector signals from the “composite” physics objects we use in measurements
975 and searches for new physics.

976 **6.1 Primitive Object Reconstruction**

977 The primitive objects reconstructed by ATLAS are *tracks* and (calorimeter) *clusters*.
978 These are reconstructed directly from tracking hits and calorimeter energy deposits
979 into cells. Tracks can be further divided into inner detector and muon spectrom-
980 eter tracks. Calorimeter clusters can be divided into sliding-window clusters and
981 topological clusters (topoclusters).

982 **Inner Detector Tracks**

983 Inner detector tracks are reconstructed from hits in the inner detector [90, 91] These
984 hits indicate that a charged particle has passed through the detector material. Due
985 to the 2 T solenoid in the inner detector, the hits associated with any individual
986 particle will be curved. The amount of curvature determines the momentum of the
987 particle. In any given event, there are upwards of 10^4 hits, making it impossible to do
988 any sort of combinatorics to reconstruct tracks. There are two algorithms used by
989 ATLAS track reconstruction, known as *inside-out* and *outside-in*.

990 ATLAS first employs the inside-out algorithm. One assumes the track begins
991 at the interaction point. Moving out from the interaction point, one creates track
992 seeds. Track seeds are proto-tracks constructed from three hits. These hits can be
993 distributed as three pixel hits, two pixel hits and one SCT hit, or three SCT hits.
994 One extrapolates the track and uses a combinatorial Kalman filter[90], which adds
995 the rest of the pixel and SCT hits to the seeds. This is done seed by seed, so it
996 avoids the combinatorial complexity involved with checking all hits with all seeds.
997 At this point, the algorithm applies an additional filter to avoid ambiguities from
998 nearby tracks. The TRT hits are added to the seeds using the same method. After
999 this procedure, all hits are associated to a track.

1000 The next step is to figure out the correct kinematics of the track. This is
1001 done by applying a fitting algorithm which outputs the best-fit track parameters
1002 by minimizing the track distance from hits, weighted by each hit's resolution. These
1003 parameters are $(d_0, z_0, \eta, \phi, q/p)$ where d_0 (z_0) is the transverse (longitudinal) impact
1004 parameter and q/p is the charge over the track momenta. This set of parameters
1005 uniquely defines the measurement of the trajectory of the charged particle associated
1006 to the track. An illustration of a track with these parameters is shown in Fig.6.1.

1007 The other track reconstruction algorithm is the outside-in algorithm. As the
1008 name implies, we start from the outside of the inner detector, in the TRT, and
1009 extend the tracks in toward the interaction point. One begins by seeding from
1010 TRT hits, and extending the track back towards the center of the detector. The
1011 same fitting procedure is used as in the inside-out algorithm to find the optimal
1012 track parameters. This algorithm is particularly important for finding tracks which
1013 originate from interactions with the detector material, especially the SCT. For tracks
1014 from primary vertices, this often finds the same tracks as the inside-out algorithm,
1015 providing an important check on the consistency of the tracking procedure.

1016 In the high luminosity environment of the LHC, even the tracks reconstructed

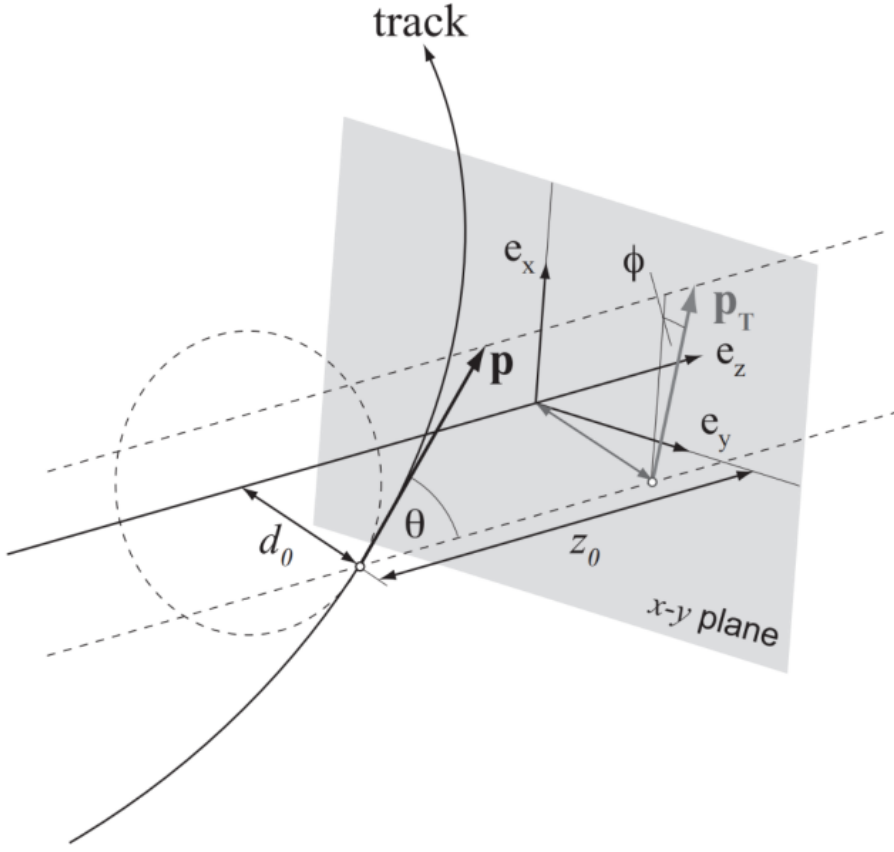


Figure 6.1: The parameters associated to a track.

from precision detectors such as those of ATLAS inner detector can sometimes lead to fake tracks from simple combinatoric chance. Several quality checks are imposed after track fitting which reduce this background. Seven silicon (pixel + SCT) hits are required for all tracks. No more than two *holes* are allowed in the pixel detector. Holes are expected measurements from the track that are missing in the pixel detector. Finally, tracks with poor fit quality, as measured by χ^2/ndf , are also rejected. Due to the high quality of the silicon measurements in the pixel detector and SCT, these requirements give good track reconstruction efficiency, as seen in Fig.6.2 for simulated events[92].



(a) Track reconstruction as a function of p_T . (b) Track reconstruction as a function of η .

Figure 6.2: Track reconstruction efficiency as a function of track p_T and η . The efficiency is defined as the number of reconstructed tracks divided by the number of generate charged particles.

1026 Sliding-window clusters

1027 The sliding-window algorithm is a way to combine calorimeter cells into composite
 1028 objects (clusters) to be used as inputs for other algorithms[93]. Sliding-window
 1029 clusters are the primary inputs to electron and photon reconstruction, as described
 1030 below. The electromagnetic calorimeter has high granularity, with a cell size of
 1031 $(\eta, \phi) = (.025, .025)$ in the coarsest second layer throughout most of the calorimeter.
 1032 The “window” consists of 3 by 5 cells in the (η, ϕ) space. All layers are added on
 1033 this same 2D space. One translates this window over the space and seeds a cluster
 1034 whenever the energy sum of the cells is maximized. If the seed energy is greater
 1035 than 2.5 GeV, this seed is called a sliding-window cluster. This choice was motivated
 1036 to optimize the reconstruction efficiency of proto-electrons and proto-photons while
 1037 rejecting fakes from electronic noise and additional particles from pileup vertices.

1038 Topological clusters

1039 Topoclusters are the output of the algorithm used within ATLAS to combine
1040 hadronic and electromagnetic calorimeter cells in a way which extracts signal from
1041 a background of significant electronic noise[94]. They are the primary input to the
1042 algorithms which reconstruct jets.

1043 Topological clusters are reconstructed from calorimeter cells in the following way.
1044 First, one maps all cells onto a single $\eta - \phi$ plane so one can speak of *neighboring*
1045 cells. Two cells are considered neighboring if they are in the same layer and directly
1046 adjacent, or if they are in adjacent layers and overlap in $\eta - \phi$ space. The *significance*
1047 ξ_{cell} of a cell during a given event is

$$\xi_{\text{cell}} = \frac{E_{\text{cell}}}{\sigma_{\text{noise},\text{cell}}} \quad (6.1)$$

1048 where $\sigma_{\text{noise},\text{cell}}$ is measured for each cell in ATLAS and E_{cell} measures the current
1049 energy level of the cell. One thinks of this as the measurement of the energy *over*
1050 *threshold* for the cell.

1051 Topocluster *seeds* are defined as calorimeter cells which have a significance $\xi_{\text{cell}} >$
1052 4. These are the inputs to the algorithm. One iteratively tests all cells adjacent
1053 to these seeds for $\xi_{\text{cell}} > 2$. Each cells passing this selection is then added to the
1054 topocluster, and the procedure is repeated. When the algorithm reaches the point
1055 where there are no additional adjacent cells with $\xi_{\text{cell}} > 2$, every positive-energy cell
1056 adjacent to the current proto-cluster is added. The collection of summed cells is a
1057 topocluster. An example of this procedure for a simulation dijet event is shown in
1058 Fig.6.3.

1059 There are two calibrations used for clusters[95]. These are known as the
1060 electromagnetic (EM) scale and the local cluster weighting (LCW) scale. The EM
1061 scale is the energy read directly out of the calorimeters as described. This scale
1062 is appropriate for electromagnetic processes. The LCW scale applies additional



Figure 6.3: Example of topoclustering on a simulated dijet event.

1063 scaling to the clusters based on the shower development. The cluster energy can be
1064 corrected for calorimeter non-compensation and the differences in the hadronic and
1065 electromagnetic calorimeters’ responses. This scale provides additional corrections
1066 that improve the accuracy of hadronic energy measurements. This thesis only uses
1067 the EM scale corrections. LCW scaling requires additional measurements that only
1068 became available with additional data. Due to the jet calibration procedure that
1069 we will describe below, it is also a relatively complicated procedure to rederive the
1070 “correct” jet energy.

1071 Muon Spectrometer Tracks

1072 Muon spectrometer tracks are fit using the same algorithms as the ID tracks, but
1073 different subdetectors. The tracks are seeded by hits in the MDTs or CSCs. After
1074 seeding in the MDTs and CSCs, the hits from all subsystems are refit as the final
1075 MS track. These tracks are used as inputs to the muon reconstruction, as we will see
1076 below.

1077 6.2 Physics Object Reconstruction and Quality

1078 Identification

1079 There are essentially six objects used in ATLAS searches for new physics: electrons,
1080 photons, muons, τ -jets, jets, and E_T^{miss} . The reconstruction of these objects is
1081 described here. In this thesis, τ lepton jets are not treated differently from other
1082 hadronic jets, and we will not consider their reconstruction algorithms. A very
1083 convenient summary plot is shown in Fig.6.4.

1084 One often wishes to understand “how certain” we are that a particular object
1085 is truly the underlying physics object. In ATLAS, we often generically consider, in



Figure 6.4: The interactions of particles with the ATLAS detector. Solid lines indicate the particle is interacting with the detector, while dashed lines are shown where the particle does not interact.

1086 order, *very loose*, *loose*, *medium*, and *tight* objects¹. These are ordered in terms of
 1087 decreasing object efficiency, or equivalently, decreasing numbers of fake objects. We
 1088 will also describe briefly the classification of objects into these categories.

1089 In this thesis, since we present a search for new physics in a zero lepton final state,
 1090 we will provide additional details about jet and E_T^{miss} reconstruction.

¹ These are not all used for all objects, but it's conceptually useful to think of these different categories.

1091 Electrons and Photons

1092 Reconstruction

1093 The reconstruction of electrons and photons (often for brevity called “electromagnetic
1094 objects”) is very similar [93, 96, 97]. This is because the reconstruction begins with
1095 the energy deposit in the calorimeter in the form of an electromagnetic shower. For
1096 any incoming e/γ , this induces many more electrons and photons in the shower. The
1097 measurement in the calorimeter is similar for these two objects.

1098 One begins the reconstruction of electromagnetic objects from the sliding-window
1099 clusters reconstructed from the EM calorimeter. These $E > 2.5$ GeV clusters the
1100 the primary seed for electrons and photons. One then looks for all ID tracks within
1101 $\Delta R < 0.3$, where $\Delta R = \sqrt{\Delta\eta^2 + \Delta\phi^2}$. We “match” the track and cluster if they are
1102 within $\Delta\phi < 0.2$ in the direction of track curvature, or $\Delta\phi < 0.05$ in the direction
1103 opposite the track curvature. Those track-cluster seeds with tracks pointing to the
1104 primary vertex are reconstructed as electrons.

1105 For photons, we have two options to consider, known as *converted* and *unconverted*
1106 photons. Due to the high energy of the LHC collisions, typical photons have energy
1107 $>\sim 1$ GeV. At this scale, photons interact almost exclusively via pair-production in
1108 the presence of the detector material, as shown in Fig.6.5 [56]. If the track-cluster seed
1109 has a track which does not point at the primary vertex, we reconstruct this object as a
1110 converted photon. This happens since the photon travels a distance before decay into
1111 two electrons, and see the tracks coming from this secondary vertex. Those clusters
1112 which do not have any associated tracks are then reconstruced as an unconverted
1113 photon.

1114 The final step in electromagnetic object reconstruction is the final energy value
1115 assigned to these objects. This process is different between electrons and photons due
1116 to their differing signatures in the EM calorimeter. In the barrel, electrons energies

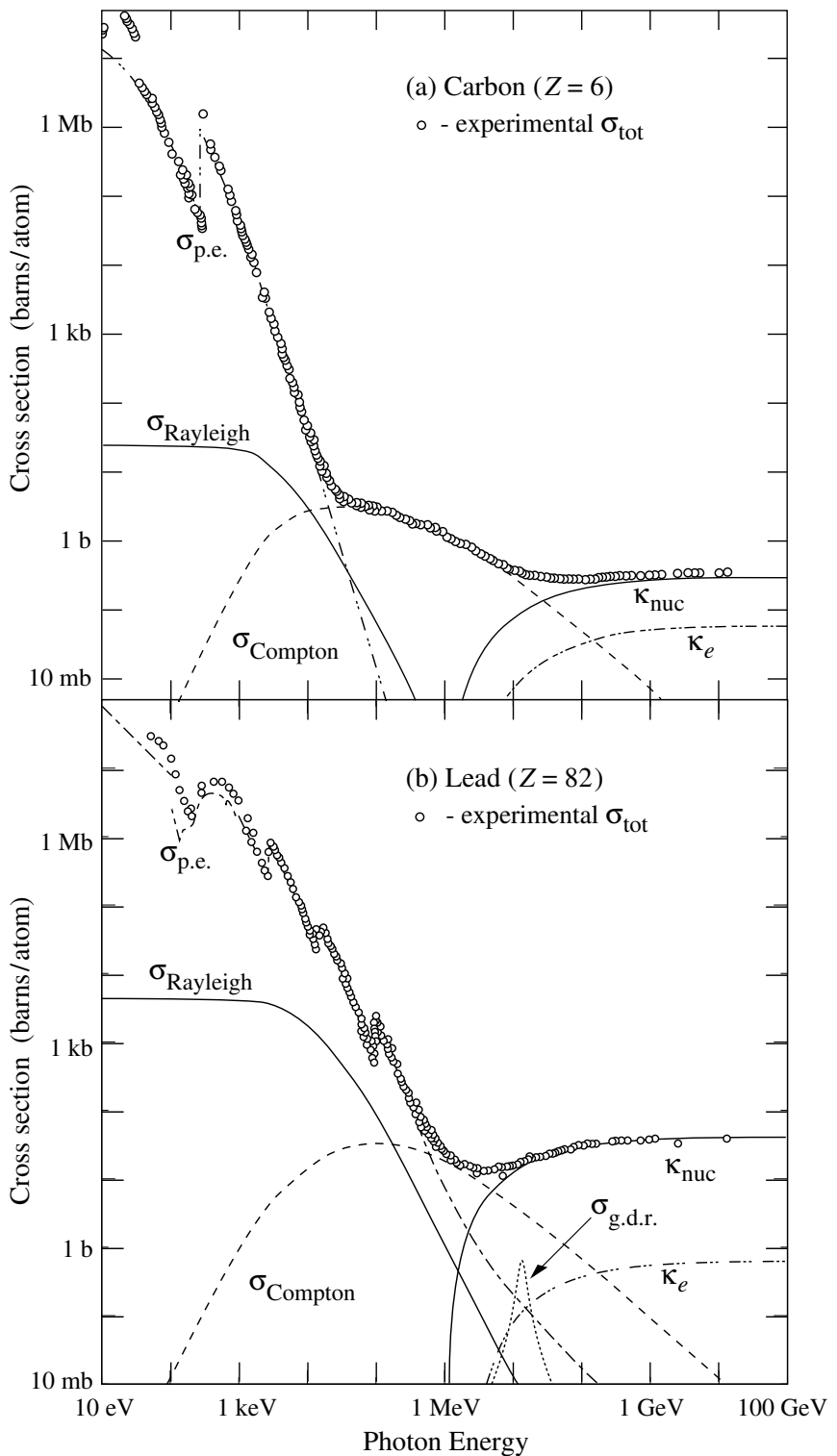


Figure 6.5: Photon total cross sections as a function of energy in carbon and lead, showing the contributions of different processes[56].

1117 are assigned as the sum of the 3 clusters in η and 7 clusters in ϕ to account for the
1118 electron curving in the ϕ direction. Barrel photons are assigned the energy sum of
1119 (3, 5) clusters in (η, ϕ) space. In the endcap, the effect of the magnetic field on the
1120 electrons is smaller, and there is a coarser granularity. Both objects sum the (5, 5)
1121 clusters for their final energy value.

1122 Quality Identification

1123 Electrons have a number of important backgrounds which can give fakes. Fake
1124 electrons come primarily from secondary vertices in hadron decays or misidentified
1125 hadronic jets. To reduce these backgrounds, quality requirements are imposed on
1126 electron candidates. Loose electrons have requirements imposed on the shower
1127 shapes in the electromagnetic calorimeter and on the quality of the associated ID
1128 track. There is also a requirement that there is a small energy deposition in the
1129 hadronic calorimeter behind the electron, to avoid jets being misidentified as electrons
1130 (low hadronic leakage). Medium and tight electrons have increasingly stronger
1131 requirements on these variables, and additional requirements on the isolation (as
1132 measured by ΔR) and matching of the ID track momentum and the calorimeter
1133 energy deposit.

1134 Photons are relatively straightforward to measure, since there are few background
1135 processes[98]. The primary one is pion decays to two photons, which can cause a jet
1136 to be misidentified as photon. Loose photons have requirements on the shower shape
1137 and hadronic leakage. Tight photons have tighter shower shape cuts, especially on
1138 the high granularity first layer of the EM calorimeter. The efficiency for unconverted
1139 tight photons as a function of p_T is shown in

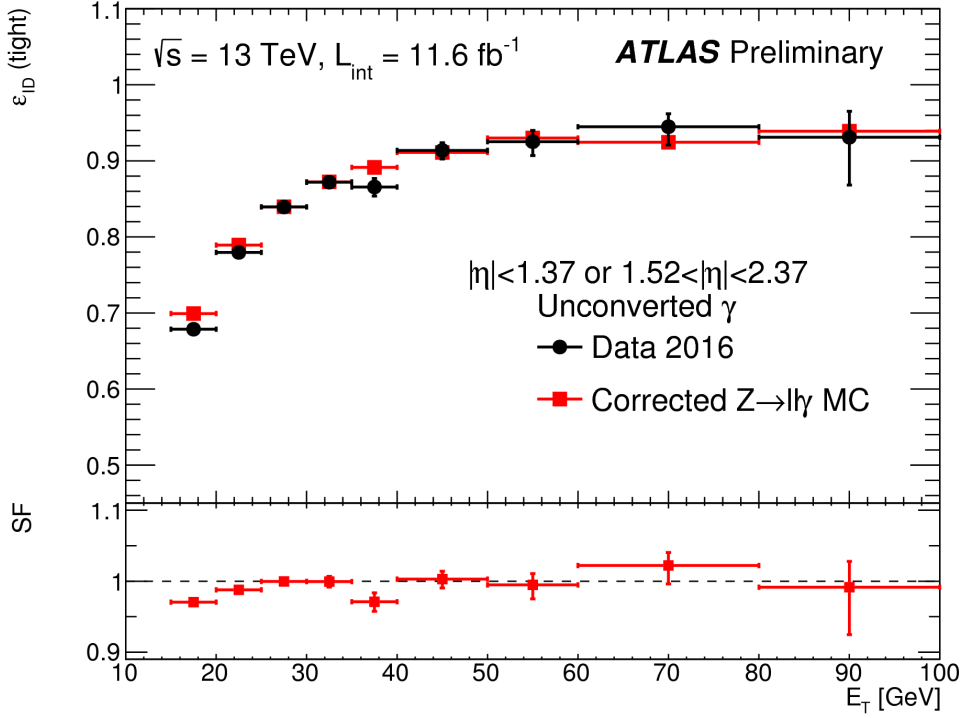


Figure 6.6: Unconverted photon efficiency as measured in [98].

1140 Muons

1141 Reconstruction

1142 Muons are reconstructed using measurements from all levels of the ATLAS detec-
 1143 tor[99]. They leave a ID track, a small, characteristic deposition in the EM calorime-
 1144 ter, and then a track in the muon spectrometer. The primary reconstruction technique
 1145 produces a so-called *combined* muon. “Combined” means using a combination of the
 1146 ID and MS tracks to produce the final reconstructed muon kinematics. This is done
 1147 by refitting the hits associated to both tracks, and using this refit track for the muon
 1148 kinematics. This process produces the best measured muons, although several other
 1149 worse algorithms are used when the full detector information is missing. An example
 1150 is in the region $2.5 < |\eta| < 2.7$ outside the ID acceptance, where MS tracks are used
 1151 without the corresponding ID tracks.

1152 **Quality Identification**

Several additional criteria are used to assure muon measurements are free of significant background contributions, especially from pion and kaon decays to muons. Muons produced via these decay processes are often characterized by a “kink”. Candidate muons with a poor fit quality, characterized by $\chi^2/\text{n.d.f.}$, are thus rejected. Additionally, the absolute difference in momentum measurements between the ID and MS provide another handle, since the other decay products from hadron decays carry away some amount of the initial hadron momentum. This is measured by

$$\rho' = \frac{|p_T^{\text{ID}} - p_T^{\text{MS}}|}{p_T^{\text{Combined}}}. \quad (6.2)$$

Additionally, there is a requirement on the q/p significance, defined as

$$S_{q/p} = \frac{|(q/p)^{\text{ID}} - (q/p)^{\text{MS}}|}{\sqrt{\sigma_{\text{ID}}^2 + \sigma_{\text{MS}}^2}}. \quad (6.3)$$

1153 The $\sigma_{\text{ID,MS}}$ in the denominator of Eq.6.3 are the uncertainties on the corresponding
1154 quantity from the numerator. Finally, cuts are placed on the number of hits in the
1155 various detector elements.

1156 Subsequently tighter cuts on these variables allow one to define the different muon
1157 identification criteria. Loose muons have the highest reconstruction efficiency, but
1158 the highest number of fake muons, since there are no requirements on the number
1159 of subdetector hits and the loosest requirements on the suite of quality variables.
1160 Medium muons consist of Loose muons with tighter cuts on the quality variables.
1161 They also require more than three MDT hits in at least two MDT layers. These are
1162 the default used by ATLAS analyses. Tight muons have stronger cuts than those of
1163 the medium selection, and reducing the reconstruction efficiency. The reconstruction
1164 efficiency as a function of p_T can be seen for Medium muons in Fig.6.7.

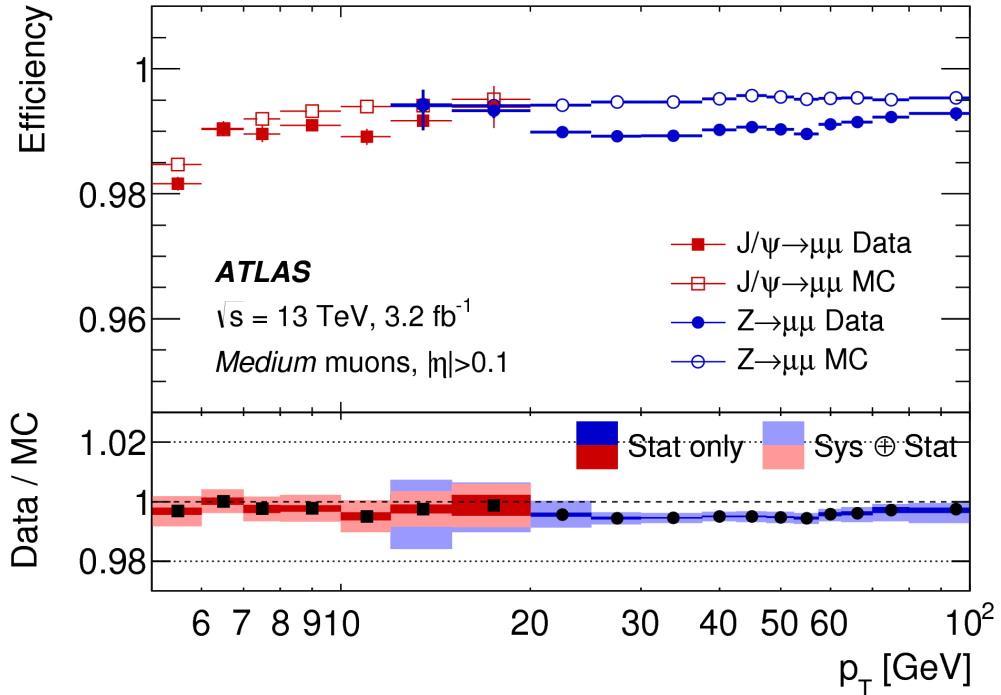


Figure 6.7: Medium muon efficiency as measured in [99].

1165 Jets

1166 Jets are composite objects corresponding to many physical particles [56, 100, 101]
 1167 This is a striking difference from the earlier particles. Fortunately, we normally (and
 1168 in this thesis) care about the original particle produced in primary collision. In the
 1169 SM, this corresponds to quarks and gluons. Due to the hadronization process, free
 1170 quarks and gluons spontaneously hadronize and produce a hadronic shower, which
 1171 we call a jet. These showers can be measured by the EM and hadronic calorimeters,
 1172 and the charged portions can be measured in the ID. The first question is how to
 1173 combine these measurements into a composite object representing the underlying
 1174 physical parton. This is done via jet algorithms.

1175 Jet Algorithms

1176 It might seem straightforward to combine the underlying physical particles into a
1177 jet. There are three important characteristics required for any jet reconstruction
1178 algorithm to be used by ATLAS.

- 1179 • Collinear safety - if any particle with four-vector p is replaced by two particles
1180 of p_1, p_2 with $p = p_1 + p_2$, the subsequent jet should not change

1181 • Radiative (infrared) safety - if any particle with four-vector p radiates a particle
1182 of energy $\alpha \rightarrow 0$, the subsequent jet should not change

1183 • Fast - the jet algorithm should be “fast enough” to be useable by ATLAS
1184 computing resources

1185 The first two requirements can be seen in terms of requirements on soft gluon emission.
1186 Since partons emit arbitrarily soft gluons freely, one should expect the algorithms
1187 to not be affected by this emission. The final requirement is of course a practical
1188 limitation.

The algorithms in use by ATLAS (and CMS) which satisfies these requirements are collectively known as the k_T algorithms [102–104]. These algorithms iteratively combine the “closest” objects, defined using the following distance measures :

$$d_{ij} = \min(k_{T,i}^{2p}, k_{T,j}^{2p}) \frac{\Delta_{ij}^2}{R^2} \quad (6.4)$$
$$d_{iB} = k_{Ti}^{2p}$$

1189 In Eq.6.4, k_T, i is the transverse momentum of i -th jet *constituent*, Δ_{ij} is the angular
1190 distance between the constituents. Both R and p are adjustable parameters: R is
1191 known as the (jet) *cone size* and p regulates the power of the energy versus the
1192 geometrical scales. The algorithm sequence, for a given set of objects i with four-
1193 vector k :

- 1194 1. Find the minimum distance in the set of all d_{ij} and d_{iB} .

1195 2. If the distance is one of the d_{ij} , combine the input pair of object i, j and return
1196 to (1). If the distance is one of the d_{iB} , remove the object from the list, call it
1197 a jet, and return to (1).

1198 This process ends when all objects i have been added to a jet.

1199 Any choice of (p, R) has the requirements of collinear and radiative safety. In
1200 essence, the choice is then to optimize based on speed and the potential for new
1201 physics discoveries. In ATLAS, we make the choice of $p = -1$ which is also known
1202 as the *anti- k_T* algorithm. The choice of $R = 0.4$ is used for the distance parameter of
1203 the jets.

1204 The primary “nice” quality of this algorithm can be seen with the following
1205 example. Consider three inputs to an anti- k_T algorithm, all with $\eta = 0$:

- 1206 • Object 1 : $(p_T, \phi) = (30 \text{ GeV}, 0)$
- 1207 • Object 2 : $(p_T, \phi) = (20 \text{ GeV}, -0.2)$
- 1208 • Object 3 : $(p_T, \phi) = (10 \text{ GeV}, 0.2)$
- 1209 • Object 4 : $(p_T, \phi) = (1 \text{ GeV}, 0.5)$

1210 . In the case shown, it seems natural to first combine the “bigger” objects 1 and 2.
1211 These then pick up the extra small object 3, and object 4 is not included in the jet.
1212 This is exactly what is done by the anti- k_T algorithm. The (normal) k_T algorithm with
1213 $p = 1$ instead combines the smallest objects, 3 and 4, first. Object 1 and 2 combine
1214 to form their own jet, instead of these jets picking up object 3. This behavior is not
1215 ideal due to the effects of pileup, as we will see in the next section.

1216 Jet Reconstruction

1217 In ATLAS, jets are reconstructed using multiple different objects as inputs, including
1218 tracks, “truth” objects, calorimeter clusters, and *particle flow objects* (PFOs). For

1219 physics analyses, ATLAS primarily uses jets reconstructed from calorimeter clusters,
1220 but we will describe the others here, as they are often used for derivations of
1221 systematic uncertainties or future prospects.

1222 Calorimeter jets are reconstructed using topoclusters using the anti- k_T algorithm
1223 with $R = 0.4$. The jet reconstruction algorithm is run on the collection of all
1224 topoclusters reconstructed as in Sec.6.1. Both EM and LCW scale clusters are used
1225 in the ATLAS reconstruction software and produce two sets of jets for analysis. As
1226 stated above, this thesis presents an analysis using jets reconstructed using EM scale
1227 clusters, which we refer to these as *EM jets*.

1228 Tracks can be used as inputs to jet reconstruction algorithms. Jets reconstructed
1229 from tracks are known as *track jets*. Since the ID tracks do not measure neutral
1230 objects, these jets measure an incorrect energy. However, these are still useful for
1231 checks and derivations of systematic uncertainties.

1232 *Truth* jets are reconstructed from *truth* particles. In this case, truth is jargon for
1233 simulation. In simulation, the actual simulated particles are available and used as
1234 inputs to the jet reconstruction algorithms. Similarly to track jets, these are not useful
1235 in and of themselves. Instead, truth jets are used for comparisons and derivations of
1236 systematic uncertainties.

1237 The last object used as inputs to jet reconstruction algorithms are *particle flow*
1238 *objects* (PFOs). These are used extensively as the primary input to jet particle
1239 reconstruction algorithms by the CMS collaboration[105]. Particle flow objects are
1240 reconstructed by associating tracks and clusters through a combination of angular
1241 distance measures and detector response measurements to create a composite object
1242 which contains information from both the ID and the calorimeters. For calorimeter
1243 clusters which do not have any associated ID track, the cluster is simply the PFO.
1244 The natural association between tracks and clusters provides easy pileup subtraction
1245 since tracks are easily associated to the primary vertex. This technique is generally

1246 used in CMS, and ATLAS has been slow to adopt the same. As pileup has increased,
1247 the utility of using PFOs as inputs to jet reconstruction has increased as well.

1248 **Jet Calibration**

1249 Jets as described in the last section are still *uncalibrated*. Even correcting the cluster
1250 energies using the LCW does not fully correct the jet energy, due to particles losing
1251 energy in the calorimeters. The solution to this is the *jet energy scale* (JES). The
1252 JES is a series of calibrations which on average restore the correct truth jet energy
1253 for a given reconstructed jet. These steps are shown in Fig.6.8 and described here.

1254 The first step is the origin correction. This adjusts the jet to point at the
1255 primary vertex. Next, is the jet-area based pileup correction. This step subtracts
1256 the “average” pileup as measured by the energy density ρ outside of the jets and
1257 assumes this is a good approximation for the pileup inside the jet. One then removes
1258 energy $\Delta E = \rho \times A_{\text{jet}}$ in this step. The residual pileup correction makes a final offset
1259 correction by parametrizing the change in jet energy as a function of the number of
1260 primary vertices N_{PV} and the average number of interactions μ .

1261 The next step is the most important single correction, known as the AbsoluteEta-
1262 JES step. Due to the use of non-compensation and sampling calorimeters in ATLAS,
1263 the measured energy of a jet is a fraction of the true energy of the outgoing parton.
1264 Additionally, due to the use of different technologies and calorimeters throughout the
1265 detector, there are directional biases induced by these effects. The correction bins a
1266 multiplicative factor in p_{T} and η which scales the reconstructed jets to corresponding
1267 truth jet p_{T} . This step does not entirely correct the jets, since it is entirely a
1268 simulation-based approach.

1269 The final steps are known as the global sequential calibration (GSC) and the
1270 residual in-situ calibration. The GSC uses information about the jet showering shape
1271 to apply additional corrections based on the expected shape of gluon or quark jets.

1272 The final step is the residual in-situ calibration, which is only applied to data. This
1273 step uses well-measured objects recoiling off a jet to provide a final correction to the
1274 jets in data. In the low p_T region ($20 \text{ GeV} \sim < p_{T,\text{jet}} \sim < 200 \text{ GeV}$), $Z \rightarrow ll$ events are
1275 used as a reference object. In the middle p_T region ($100 \text{ GeV} \sim < p_{T,\text{jet}} \sim < 600 \text{ GeV}$),
1276 the reference object is a photon, while in the high p_T region ($p_{T,\text{jet}} \sim > 200 \text{ GeV}$),
1277 the high p_T jet is compared to multiple smaller p_T jets. The reference object is this
1278 group of multijets. After this final correction, the data and MC scales are identical
1279 up to the corresponding uncertainties. The combined JES uncertainty as a function
1280 of p_T is shown in Fig.6.9.

1281 Jet Vertex Tagger

1282 The *jet vertex tagger* (JVT) technique is used to separate pileup jets from those
1283 associated to the hard primary vertex[106]. The technique for doing so first involves
1284 *ghost association*[107]. Ghost association runs the anti- k_T jet clustering algorithm on
1285 a combined collection of the topoclusters and tracks. The tracks *only* momenta are
1286 set to zero², with only the directional information is included. As discussed above,
1287 the anti- k_T algorithm is “big to small”; tracks are associated to the “biggest” jet near
1288 them in (η, ϕ) . This method uniquely associates each track to a jet, without changing
1289 the final jet kinematics.

1290 The JVT technique uses a combination of these track variables to determine the
1291 likelihood that the jet originated at the primary vertex. For jets which have associated
1292 tracks from ghost association, this value ranges from 0 (likely pileup jet) to 1 (likely
1293 hard scatter jet). Jets without associated tracks are assigned $\text{JVT} = -.1$. The
1294 working point of $\text{JVT} > .59$ is used for jets in this thesis.

²Well, not exactly zero, since zero momentum tracks wouldn’t have a well-defined (η, ϕ) coordinate, but set to a value obeying $p_{T,\text{track}} << 400 \text{ MeV} = p_{\text{track,min}}$. This is the minimum momentum for a track to reach the ATLAS inner detector.

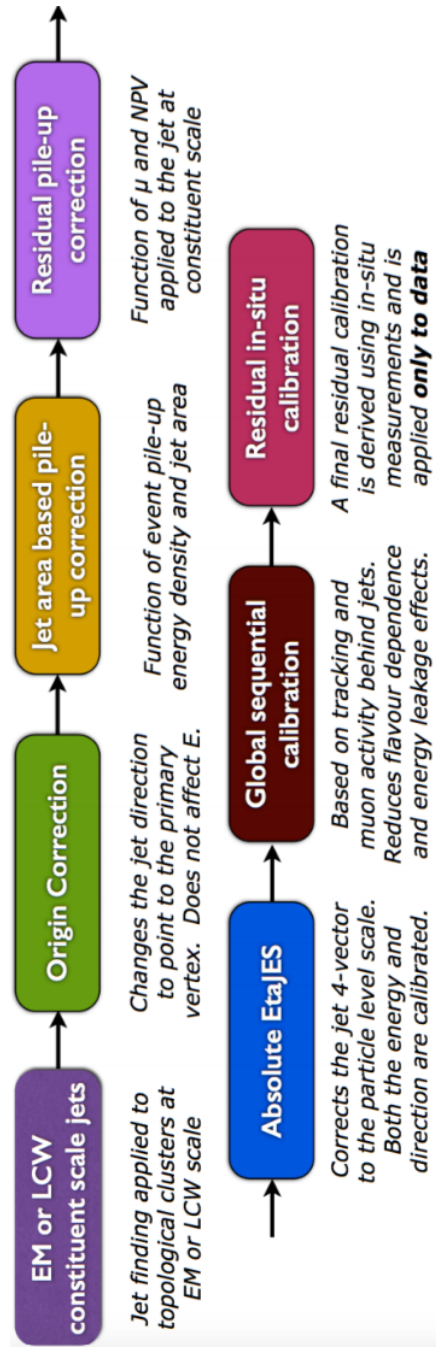


Figure 6.8: The steps used by ATLAS to calibrate jets

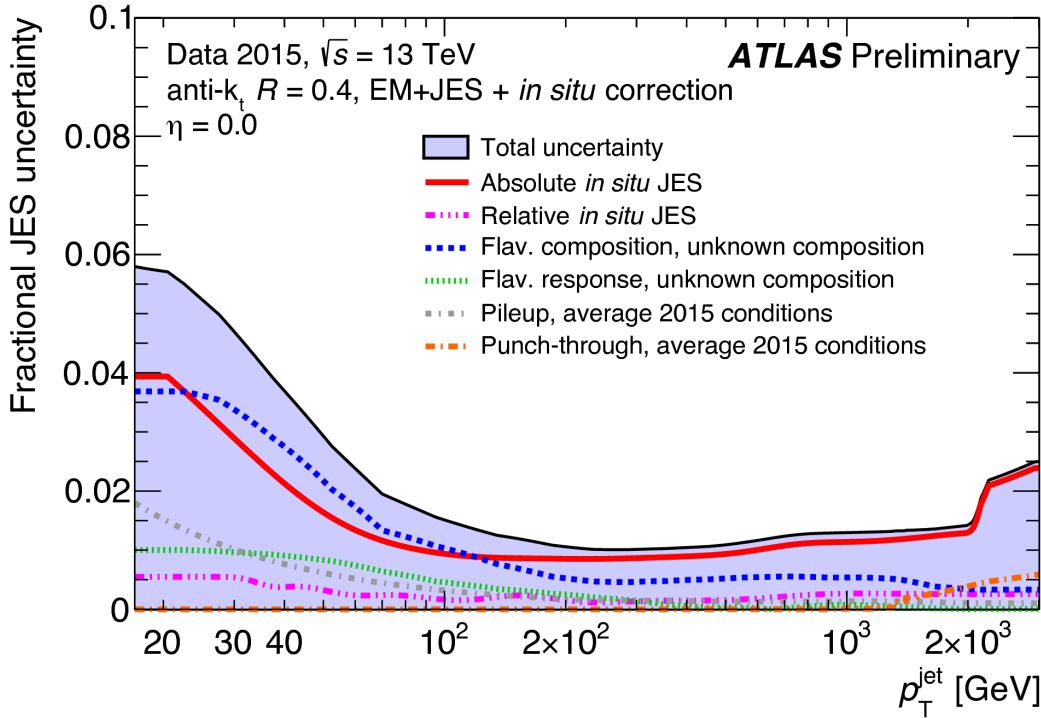


Figure 6.9: Combined jet energy scale uncertainty as a function of p_T at $\eta = 0$.

1295 B-jets

1296 Jets originating from bottom quarks (b-jets) are interesting physical phenomena that
 1297 can be *tagged* by the ATLAS detector[Aad:2015ydr, 108]. B-hadrons, which have
 1298 a comparatively long lifetime compared to hadrons consisting of lighter quarks, can
 1299 travel a macroscopic distance inside the ATLAS detector. The high-precision tracking
 1300 detectors identify the secondary vertices from these decays and the jet matched to
 1301 that vertex is called a *b-jet*. The “MV2c10” algorithm, based on boosted decision
 1302 trees, identifies these jets using a combination of variables sensitive to the difference
 1303 between light-quark and b-quark jets. The efficiency of this tagger is 77%, with a
 1304 rejection factor of 134 for light-quarks and 6 for charm jets.

1305 Missing Transverse Momentum

1306 Missing transverse momentum E_T^{miss} [109] is a key observable in searches for new
1307 physics, especially in SUSY searches[110, 111]. However, E_T^{miss} is not a uniquely
1308 defined object when considered from the detector perspective (as compared to the
1309 Feynammn diagram), and it is useful to understand the choices that affect the
1310 performance of this observable in searches for new physics.

1311 E_T^{miss} Definitions

Hard objects refers to all physical objects as defined in the previous sections. The
 E_T^{miss} reconstruction procedure uses these hard objects and the *soft term* to provide
a value and direction of the missing transverse momentum. The $E_{x(y)}^{\text{miss}}$ components
are calculated as:

$$E_{x(y)}^{\text{miss}} = E_{x(y)}^{\text{miss, } e} + E_{x(y)}^{\text{miss, } \gamma} + E_{x(y)}^{\text{miss, jets}} + E_{x(y)}^{\text{miss, } \mu} + E_{x(y)}^{\text{miss, soft}}, \quad (6.5)$$

1312 where each value $E_{x(y)}^{\text{miss, } i}$ is the negative vectorial sum of the calibrated objects defined
1313 in the previous sections.

1314 For purposes of E_T^{miss} reconstruction, we must assign an ordering of *overlap*
1315 *removal*. This is to avoid double counting of the underlying primitive objects (clusters
1316 and tracks) which are inputs to the reconstruction of the physics objects. We resolve
1317 this in the following order : electrons, photons , jets and muons. This is motivated
1318 by the performance of the reconstruction of these objects in the calorimeters.

1319 The soft term $E_{x(y)}^{\text{miss, soft}}$ contains all of the primitive objects which are not
1320 associated to any of the reconstructed physics objects. Of course, we need to choose
1321 which primitive object to use. The primary choices which have been used within
1322 ATLAS are the *calorimeter-based soft term* (CST) and the *track-based soft term*
1323 (TST). Based on the soft term choice, we then call E_T^{miss} built with a CST (TST)

1324 soft term simply CST (TST) E_T^{miss} . An additional option, which will be important
1325 as pileup continues to increase, particle flow E_T^{miss} (PFlow E_T^{miss}).

1326 The CST E_T^{miss} was used for much of the early ATLAS data-taking. CST E_T^{miss} is
1327 built from the calibrated hard objects, combined with the calorimeter clusters which
1328 are *not* assigned to any of those hard objects. In the absence of pileup, it provides the
1329 best answer for the “true” E_T^{miss} in a given event, due to the impressive hermiticity of
1330 the calorimeters. Unfortunately, the calorimeters do not know “where” from where
1331 their energy deposition came, and thus CST is susceptible to drastically reduced
1332 performance as pileup is increased.

1333 TST E_T^{miss} is the standard for ATLAS searches as currently performed by ATLAS.
1334 TST E_T^{miss} is built by using the calibrated hard objects and the soft term is built from
1335 the tracks which are not assigned to any of those hard objects. In particular, due
1336 to the impressive track-vertex association efficiency, one chooses tracks which only
1337 come from the primary vertex. This drastically reduces the pileup contributions to
1338 the E_T^{miss} measurement. However, since the ID tracking system is unable to measure
1339 neutral objects, the TST E_T^{miss} is “wrong”. This bias is important to understand for
1340 many measurements. However, in most searches for new physics, the soft E_T^{miss} is
1341 generally a small fraction of the total E_T^{miss} , and thus this bias is not particularly
1342 hurtful.

1343 PFlow E_T^{miss} uses the PFOs described above to build the E_T^{miss} . The PFOs which
1344 are assigned to hard objects are calibrated, and the PFOs which are not assigned
1345 to any hard object are added to the soft term. In this context, it is convenient to
1346 distinguish between “charged” and “neutral” PFOs. Charged PFOs can be seen as a
1347 topocluster which has an associated track, while neutral PFOs do not. This charged
1348 PFO is essentially a topocluster that we are “sure” comes from the primary vertex.
1349 The neutral PFOs are in the same status as the original topoclusters. Thus a “full”
1350 PFlow E_T^{miss} should have performance somewhere between TST E_T^{miss} and CST E_T^{miss} ³.

1351 A *charged* PFlow E_T^{miss} should for sanity be the same as TST.

1352 **Measuring E_T^{miss} Performance : event selection**

1353 The question is now straightforward: how do we compare these different algorithms?
1354 We compare these algorithms in $Z \rightarrow \ell\ell + \text{jets}$ and $W \rightarrow \ell\nu + \text{jets}$ events. Due to
1355 the presence of leptons, these events are well-measured “standard candles”. Here
1356 we present the results in early 2015 data with $Z \rightarrow \mu\mu$ and $W \rightarrow e\nu$ events, as
1357 shown in [112, 113]. This result was important to assure the integrity of the E_T^{miss}
1358 measurements at the higher energy and pileup environment of Run-2.

1359 The $Z \rightarrow \ell\ell$ selection is used to measure the intrinsic E_T^{miss} resolution of the
1360 detector. The only possible source of neutrinos in these decays is from heavy-flavor
1361 decays inside of jets, and thus $Z \rightarrow \ell\ell$ events they have very low E_T^{miss} . This provides
1362 an ideal event topology to understand the modelling of E_T^{miss} mismeasurement.
1363 Candidate $Z \rightarrow \mu\mu$ events are first required to pass a muon or electron trigger, as
1364 described in Table 5.1. Offline, the selection of $Z \rightarrow \mu\mu$ events requires exactly two
1365 medium muons. The muons are required to have opposite charge and $p_T > 25 \text{ GeV}$,
1366 and mass of the dimuon system is required to be consistent with the Z mass
1367 $|m_{ll} - m_Z| < 25 \text{ GeV}$.

$W \rightarrow \ell\nu$ events are an important topology to evaluate the E_T^{miss} modelling in
an event with real E_T^{miss} . This E_T^{miss} is from the neutrino, which is not detected.
The E_T^{miss} in these events has a characteristic distribution with a peak at $\frac{1}{2}m_W$. The
selection of $W \rightarrow e\nu$ events begins with the selection of exactly one electron of medium
quality. A selection on TST $E_T^{\text{miss}} > 25 \text{ GeV}$ drastically reduces the background from
multijet events where the jet fakes an electron. The transverse mass is used to select

³Naively, due to approximate isospin symmetry, about 2/3 of the hadrons will be charged and 1/3 will be neutral.

the $W \rightarrow e\nu$ events :

$$m_T = \sqrt{2p_T^\ell E_T^{\text{miss}}(1 - \cos \Delta\phi)}, \quad (6.6)$$

1368 where $\Delta\phi$ is the difference in the ϕ between the E_T^{miss} and the electron. m_T is required
1369 to be greater than 50 GeV.

1370 There are two main ingredients to investigate : the E_T^{miss} resolution and the E_T^{miss}
1371 scale.

1372 Measuring E_T^{miss} Performance in early 2015 data : metrics

1373 To compare these algorithms we use the E_T^{miss} resolution, E_T^{miss} scale, and the
1374 linearity. Representative distributions of TST E_x^{miss} , E_y^{miss} , and E_T^{miss} from early
1375 2015 datataking are shown in Fig.6.10.

The E_T^{miss} resolution is an important variable due to the fact that the bulk of the distributions associated to $E_{x(y)}^{\text{miss}}$ are Gaussian distributed [Aad2012]. However, to properly measure the tails of this distribution, especially when considering non-calorimeter based soft terms, it is important to use the root-mean square as the proper measure of the resolution. This is strictly larger than a resolution as measured using a fit to a Gaussian, due to the long tails from i.e. track mismeasurements. The resolution is measured with respect to two separate variables : $\sum E_T$ and N_{PV} . $\sum E_T$ is an important measure of the “total event activity”. It is defined as

$$\sum E_T = \sum p_T^e + \sum p_T^\gamma + \sum p_T^\tau + \sum p_T^{\text{jets}} + \sum p_T^\mu + \sum p_T^{\text{soft}}. \quad (6.7)$$

1376 The measurement as a function of N_{PV} is useful to understand the degradation of
1377 E_T^{miss} performance with increasing pileup. Figure 6.11 shows the E_T^{miss} resolution in
1378 the early 2015 data. The degradation of the E_T^{miss} performance is shown as a function
1379 of pileup N_{PV} and total event activity $\sum E_T$.

Another important performance metric is the E_T^{miss} scale, or how “right” we are in our E_T^{miss} calculation. This can be off in various directions, as CST E_T^{miss} contains

additional particles from pileup, while soft neutral particles⁴ are ignored by TST E_T^{miss} .

To measure this in data, we again use $Z \rightarrow \mu\mu$ events, where the $Z \rightarrow \mu\mu$ system is treated as a well-measured reference object. The component of E_T^{miss} which is in the same direction as the reconstructed $Z \rightarrow \mu\mu$ system is sensitive to potential biases in the detector response. The unit vector \mathbf{A}_Z of the Z system is defined as

$$\mathbf{A}_Z = \frac{\vec{p}_T^{\ell^+} + \vec{p}_T^{\ell^-}}{|\vec{p}_T^{\ell^+} + \vec{p}_T^{\ell^-}|}, \quad (6.8)$$

where $\vec{p}_T^{\ell^+}$ and $\vec{p}_T^{\ell^-}$ are the transverse momenta of the leptons from the Z boson decay. The relevant scale metric is then the mean value of the \vec{E}_T^{miss} projected onto \mathbf{A}_Z : $\langle \vec{E}_T^{\text{miss}} \cdot \mathbf{A}_Z \rangle$. In Figure 6.12, the scale is shown for the early 2015 dataset. The negative bias, which is maximized at about 5 GeV, is a reflection of two separate effects. The soft neutral particles are missed by the tracking system, and thus ignored in TST E_T^{miss} . Missed particles due to the limited ID acceptance can also affect the scale.

For events with real E_T^{miss} , one can also look at the *linearity* in simulation. This is defined as

$$\text{linearity} = \left\langle \frac{E_T^{\text{miss}} - E_T^{\text{miss,Truth}}}{E_T^{\text{miss,Truth}}} \right\rangle. \quad (6.9)$$

$E_T^{\text{miss,Truth}}$ refers to “truth” particles as defined before, or the magnitude of the vector sum of all noninteracting particles. The linearity is expected to be zero if the E_T^{miss} is reconstructed at the correct scale.

1390 Particle Flow Performance

As described above, the resolution, scale, and linearity are the most important metrics to understand the performance of the different E_T^{miss} algorithms. In this section, we present comparisons of the different algorithms, including particle flow, in simulation

⁴“Soft” here means those particles which are not hard enough to be reconstructed as their own particle, using the reconstruction algorithms above.

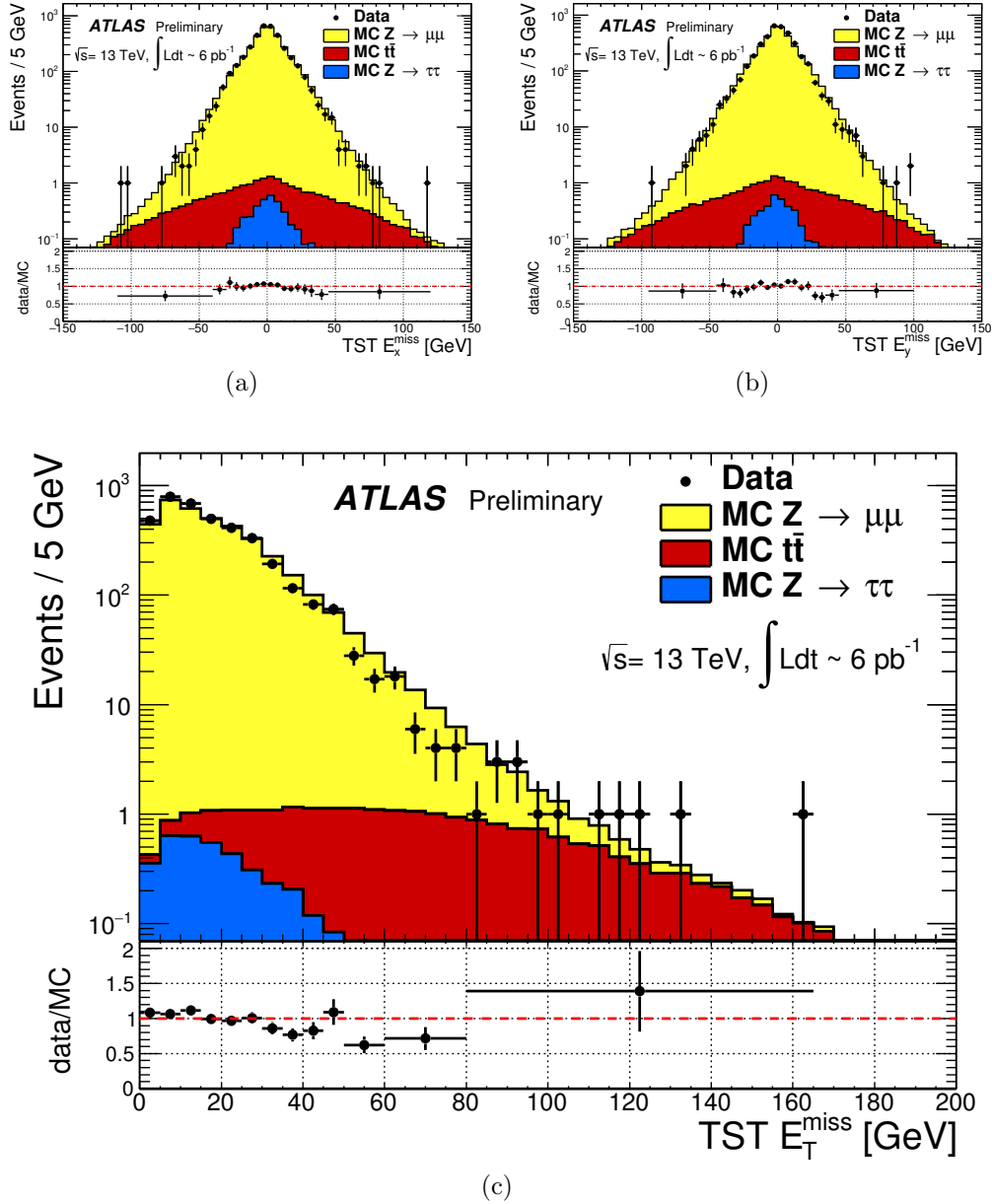


Figure 6.10: TST E_{x}^{miss} , E_{y}^{miss} , and $E_{\text{T}}^{\text{miss}}$ distributions of early $\sqrt{s} = 13$ TeV data compared with simulation after the $Z \rightarrow \mu\mu$ selection described in Sec. 6.2. The data sample consists of 6 pb^{-1} .

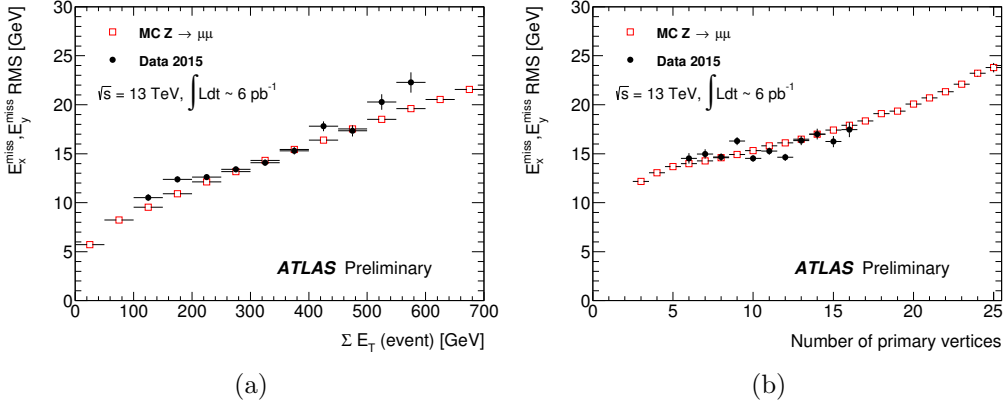


Figure 6.11: Resolution of TST E_T^{miss} of early $\sqrt{s} = 13$ TeV data compared with simulation after the $Z \rightarrow \mu\mu$ selection described in Sec.6.2. The data sample consists of 6 pb^{-1} .

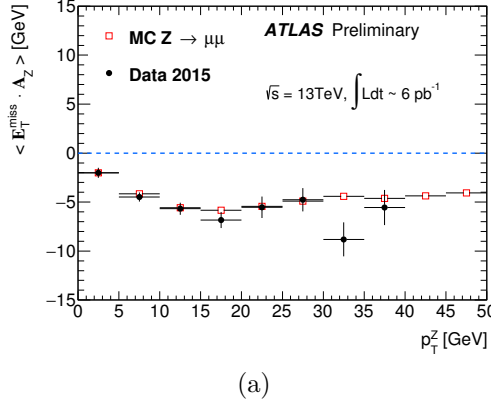


Figure 6.12: Scale of TST E_T^{miss} of early $\sqrt{s} = 13$ TeV data compared with simulation after the $Z \rightarrow \mu\mu$ selection described in Sec.6.2. The data sample consists of 6 pb^{-1} .

1394 and using a data sample from 2015 of 80 pb^{-1} . In these plots, ‘‘MET_PFlow-TST’’
1395 refers to charged PFlow E_T^{miss} , while the other algorithms are as described above.

1396 Figures ?? show the resolution and scale in simulated $Z \rightarrow \mu\mu$ events. The
1397 resolution curves follow the ‘‘intuitive’’ behavior discussed before. Due to the high
1398 pileup in 2015 run conditions, the CST E_T^{miss} resolution is poor, and becomes even
1399 poorer with increasing pileup and event activity. The ‘‘regular’’ PFlow E_T^{miss} shows
1400 reduces pileup and event activity dependence as compared to the CST. As stated
1401 earlier, the E_T^{miss} from the PFlow algorithm can be seen as a hybrid of TST E_T^{miss}

1402 and CST E_T^{miss} . The charged PFOs ($\sim 2/3$) are pileup suppressed, while the neutral
1403 PFOs (or topoclusters) are not. Both charged PFlow and TST E_T^{miss} show only a
1404 small residual dependence on N_{PV} and $\sum E_T$, since they have fully pileup suppressed
1405 inputs through the track associations.

1406 The scale plots are shown for $Z + \text{jets}$ events and Z events with no jets. For the
1407 nonsuppressed CST, the scale continues to worsen with increasing p_T^Z . It is almost
1408 always the worst performing algorithm. The standard PFlow algorithm performs the
1409 second worst in the region of high p_T^Z , but is the best at low p_T^Z . The most exciting note
1410 in this plot is the improved scale of the charged PFlow E_T^{miss} compared to the TST
1411 E_T^{miss} . Considering the resolution is essentially identical, the PFlow algorithm is better
1412 picking up the contributions from additional neutral particles. In events with no jets,
1413 the soft term is essentially the only indication of the E_T^{miss} mismeasurement, since
1414 the muons will be well-measured. In this case, the pileup effects cancel, on average,
1415 due to the $U(1)_\phi$ symmetry of the ATLAS detector, and CST performs rather well
1416 compared to the more complicated track-based algorithms. The full PFlow algorithm
1417 performs best, since it provides a small amount of pileup suppression on the neutral
1418 components from CST.

1419 The resolution and linearity are shown in simulated $W \rightarrow e\nu$ events in Figure ???.
1420 The resolution in $W \rightarrow e\nu$ events shows a similar qualitative behavior to that shown
1421 in $Z \rightarrow \mu\mu$ events. The CST E_T^{miss} has the worst performance, with charged PFlow
1422 E_T^{miss} performing best. The surprise here is that the scale associated to TST E_T^{miss} in
1423 these events is best throughout the space parameterized by $E_T^{\text{miss,Truth}}$, except for one
1424 bin at $40 \text{ GeV} < E_T^{\text{miss,Truth}} < 50 \text{ GeV}$. The scale in these events is best measured
1425 using a track-based soft term.

1426 The resolution also investigated in real data passing the $Z \rightarrow \mu\mu$ selection
1427 described above. A comparison of the E_T^{miss} between real data and simulation for
1428 each algorithm is presented in Figure 6.16. The resolution as a function of $\sum E_T$ and

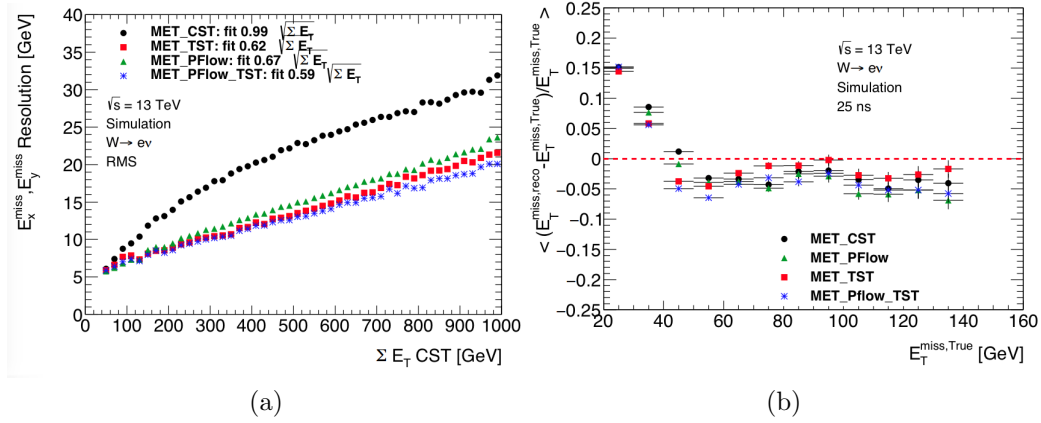


Figure 6.13: Comparison of E_T^{miss} resolution and linearity using different E_T^{miss} algorithms with simulated $W \rightarrow e\nu$ events.

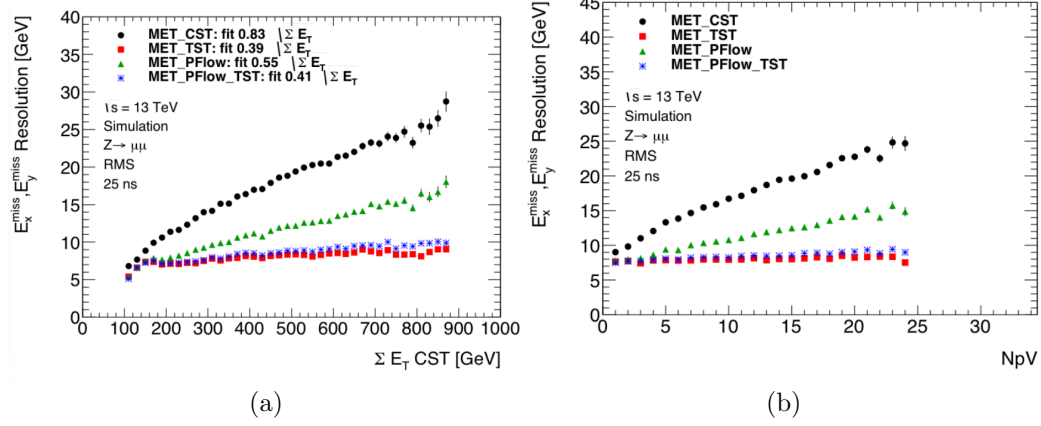


Figure 6.14: Comparison of E_T^{miss} resolution using different E_T^{miss} algorithms with simulated $Z \rightarrow \mu\mu$ events.

1429 N_{PV} is shown in Figure 6.17 for this dataset. Overall, this plot shows the same general
 1430 features as the simulation dataset in terms of algorithm performance. However, the
 1431 performance of all algorithms seems to be significantly worse in data. This is likely due
 1432 to simplifications made in the simulation: soft interactions that cannot be simulated
 1433 can have a significant effect on an event level variable such as the E_T^{miss} resolution.

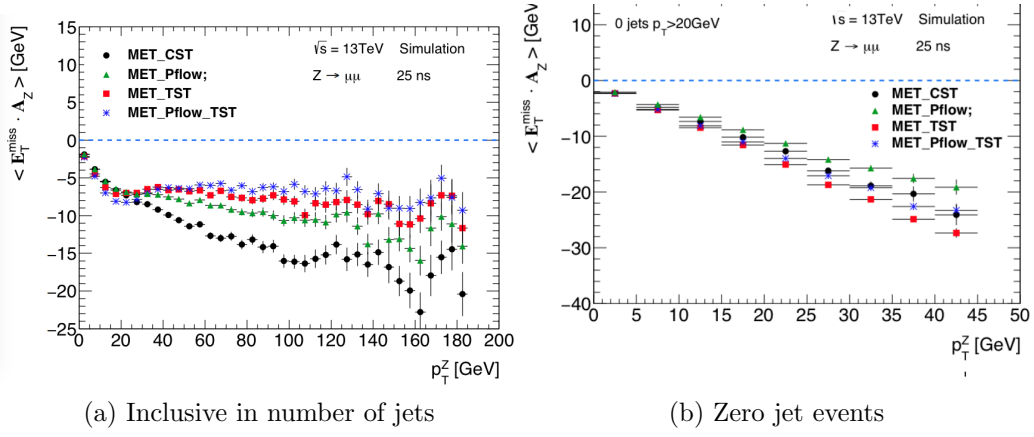


Figure 6.15: Comparison of E_T^{miss} scale using different E_T^{miss} algorithms with simulated $Z \rightarrow \mu\mu$ events.

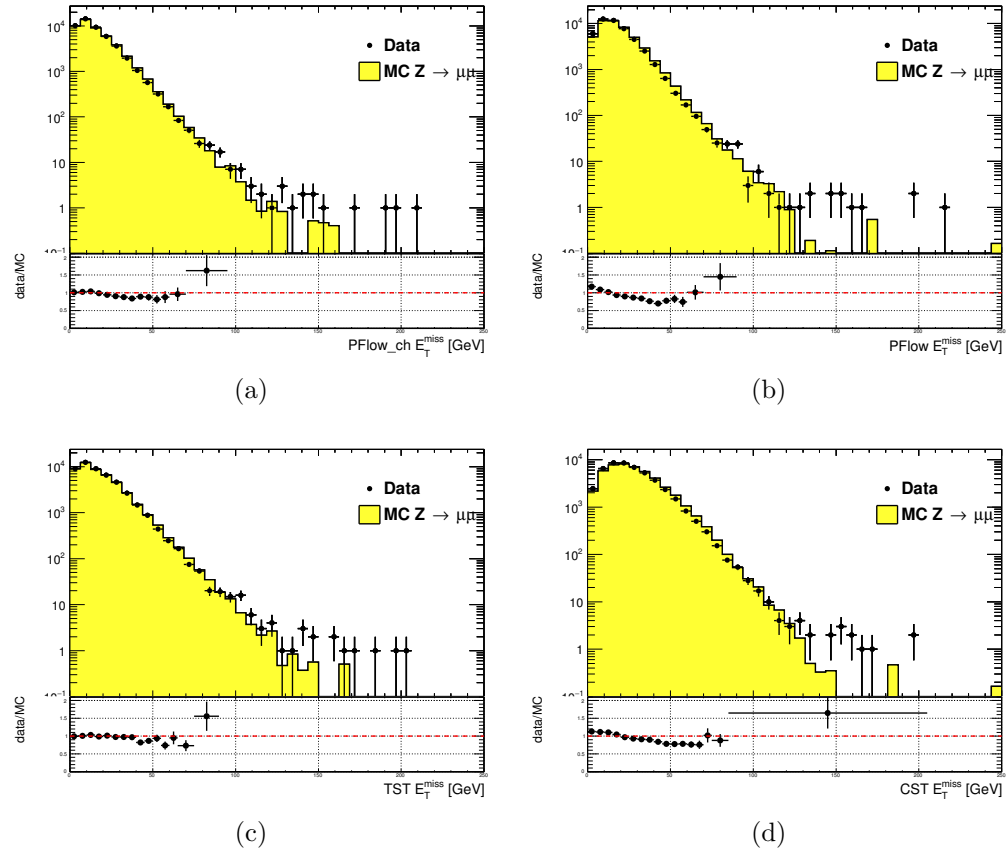


Figure 6.16: Comparison of E_T^{miss} distributions using different E_T^{miss} algorithms with a data sample of 80 pb^{-1} after the $Z \rightarrow \mu\mu$ selection described in Sec.6.2

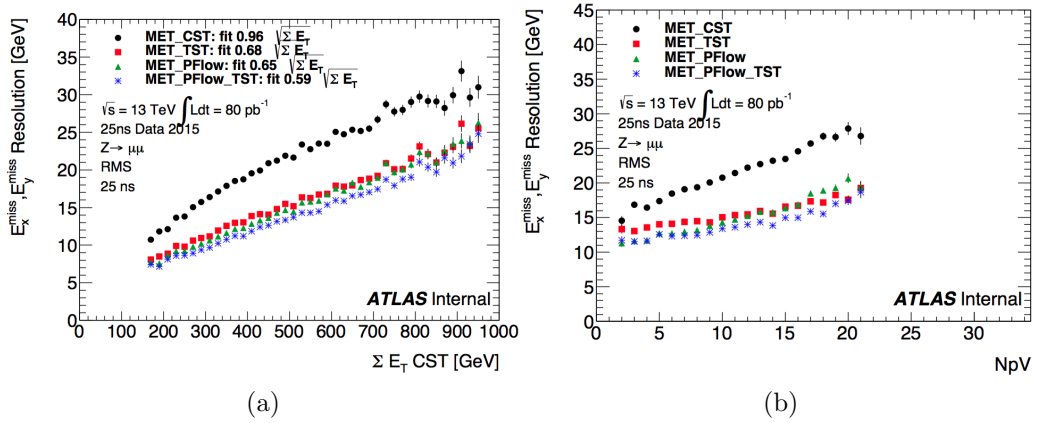


Figure 6.17: Comparison of E_T^{miss} resolution using different E_T^{miss} algorithms with a data sample of 80 pb^{-1} after the $Z \rightarrow \mu\mu$ selection described in Sec.6.2

1434

Chapter 7

1435

Recursive Jigsaw Reconstruction

1436 *Recursive Jigsaw Reconstruction* (RJR) [Jackson:2016mfb,1437 **ATLAS-CONF-2016-078]** is a novel algorithm used for the analysis presented in
1438 this thesis. RJR is the conceptual successor to the razor technique [Rogan:2010kb,1439 **Buckley:2013kua**], which has been used successfully in many new physics searches

1440 [37, 38, 40, 41, 47, 114]. In this chapter, we will first present the razor technique,

1441 and describe razor variables. We will then present the RJR algorithm. After the

1442 description of the algorithm, we will describe the precise RJR variables used by this

1443 thesis and attempt to provide some physical intuition of what they describe.

1444

7.1 Razor variables

1445

Motivation

1446 In this thesis, we consider SUSY models where gluinos and squarks are pair-produced.

1447 Pair-production is a consequence of the *R*-parity imposed in many SUSY models.1448 *R*–parity violation is highly constrained by limits on proton decay**TODO: CitE**, and

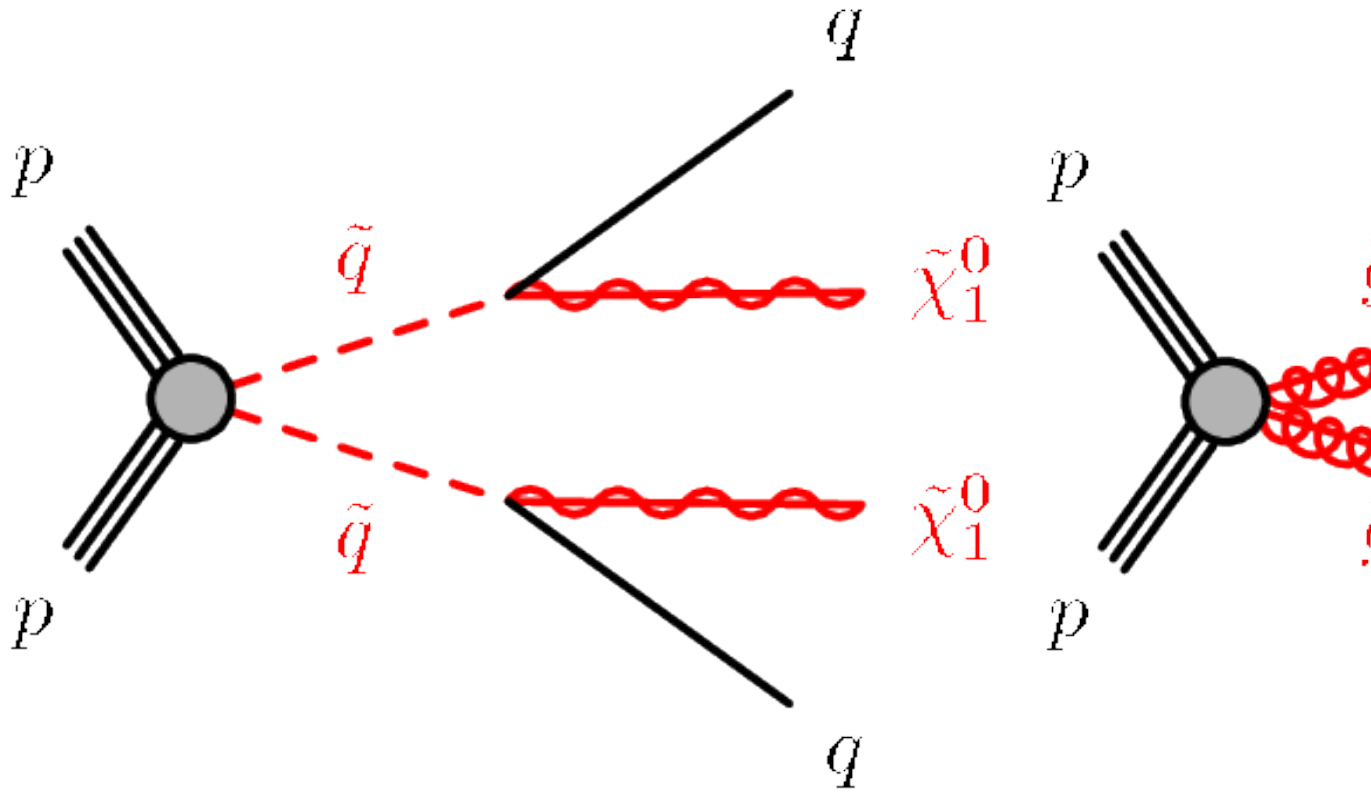
1449 is often assumed in SUSY model building. The Feynmann diagrams considered are

1450 shown in Fig.7.1.**TODO: Check on W production thing, LO naming.**1451 As discussed previously, the consequences of this \mathbb{Z}_2 symmetry are drastic. To un-

1452 derstand the utility of the razor variables, the stability of the lightest supersymmetric

1453 particle is very important. In many SUSY models, including the ones considered in

1454 this thesis, this is the lightest neutralino $\tilde{\chi}_1^0$. This means that on either side of a



(a) Disquark production

Figure 7.1: Leading order Feynman diagrams for the SUSY signals considered in this thesis

1455 SUSY decay process, where we begin with disparticle production, we have a final
 1456 state particle which is not detected. Generically, this leads to E_T^{miss} . Selections based
 1457 on E_T^{miss} are very good at reducing dominant backgrounds, for example from QCD
 1458 backgrounds.

1459 However, there are limitations to searches based on E_T^{miss} . Due to jet mismeas-
 1460 surements, instrumental failures, finite detector acceptance, nongaussian tails in the
 1461 detector response, and production of neutrinos inside of jets, there are many sources of
 1462 “fake” E_T^{miss} which does not correspond to a Standard Model neutrino or new physics
 1463 object such as an LSP. An additional limitation is the complete lack of longitudinal
 1464 information. As events from i.e. QCD backgrounds tend to have higher boosts along

1465 the z -direction, this is ignoring an important handle in searches for new physics.
 1466 Finally, E_T^{miss} is only one object, which is a measurement for *two* separate LSPs.
 1467 **TODO: say somethign else here** The *razor variables* (M_{Δ}^R, R^2) are more robust than
 1468 standard variables against these effects.

1469 **Derivation of the razor variables**

1470 To derive the razor variables (M_{Δ}^R, R^2), we start with a generic situation of the pair
 1471 production of heavy sparticles with mass m_{Heavy} .¹ Each sparticle decays to a number
 1472 of observable objects (in this thesis, jets), and an unobservable \tilde{chi}_1^0 of mass $m_{\tilde{chi}_1^0}$. We
 1473 will combine all of the jets into a *megajet*; this process will be described below. We
 1474 begin by analyzing the decay in the “rough-approximation”, or in modern parlance,
 1475 *razor frame* (R -frame). This is the frame where each sparticle is at rest.

In the R -frame, the decay is straightforward to analyze. By construction, there are in fact two R -frames, and they have identical kinematics. Each megajet has energy E_1^R, E_2^R in the frame of its parent sparticle, and we define a characteristic mass M_R :

$$E_1^R = E_2^R = \frac{m_{\text{Heavy}}^2 - m_{\tilde{chi}_1^0}^2}{2m_{\text{Heavy}}} \quad (7.1)$$

$$M_R = 2 \times E_1^R = 2 \times E_2^R = \frac{m_{\text{Heavy}}^2 - m_{\tilde{chi}_1^0}^2}{m_{\text{Heavy}}} \quad (7.2)$$

1476 For cases where $m_{\text{Heavy}} \gg m_{\tilde{chi}_1^0}$, M_R is an estimator of m_{Heavy} . This scenario
 1477 happens in the SM, such as in $t\bar{t}$ and WW events, where the \tilde{chi}_1^0 is instead a neutrino.

1478 The question now is how to use this simple derivation in the lab frame, where we
 1479 actually have measurements. There are two related issues: how to combine the jets
 1480 into the megajets, and how to “transform” to the R -frame.

To construct the megajets, the procedure is the following. For a given set of jets $j_i, i = 0, \dots, n_{\text{jet}}$, we construct *all* combinations of their four-momenta such that there

¹The razor variables have undergone confusing notational changes over the years. We will be self-consistent, but the notation used here may be different from references.

is at least one jet inside each megajet. Among this set of possible megajets $\{J_{1,2}\}$, we make the following unique choice for the megajets. We minimize the following quantity:

$$m_{J_1}^2 + m_{J_2}^2. \quad (7.3)$$

1481 In modern parlance, this is known as a *jigsaw*. It is important to note, this is a *choice*.

We now describe how we translate our megajet kinematics, measured in the lab frame, to the R -frame. This is a two-step procedure. We perform two *boosts*: a longitudinal boost β_L and a transverse boost β_T . Schematically,

$$J_1^R \xrightarrow{\beta_T} J_1^{CM} \xrightarrow{\beta_T} J_1^{\text{lab}} \quad (7.4)$$

$$J_2^R \xrightarrow{-\beta_T} J_2^{CM} \xrightarrow{\beta_T} J_2^{\text{lab}} \quad (7.5)$$

$$(7.6)$$

1482 The $J_{1,2}^{\text{lab}}$ correspond directly to those in the megajet construction. We drop the
 1483 “lab” designation for the rest of the discussion. The question is how to compute the
 1484 magnitudes of these boosts, given the missing degrees of freedom.

For the transverse boost β_T , recall the two megajets have equal energies in their R -frame by construction. This constraint can be reexpressed as a constraint on the magnitude of this boost, in terms of the boost velocity β_L (and Lorentz factor γ_L):

$$\beta_T = \frac{\gamma_L(E_1^- E_2) - \gamma_L \beta_L(p_{1,z} - p_{2,z})}{\hat{\beta}_T \cdot (\vec{p}_{1,T} - \vec{p}_{2,T})} \quad (7.7)$$

1485 where we have denoted the lab frame four-vectors as $p_i = (E_i, \vec{p}_{i,T}, p_z)$.

1486 7.2 Recursive Jigsaw Reconstruction

1487 The algorithm proceeds by the imposition of a particular *decay tree*, which corre-
 1488 sponds to a simplified Feynmann diagram. At each step in this decay tree, we can
 1489 calculate variables of interest, through a series of simplifying assumptions. In order
 1490 to

¹⁴⁹¹ **7.3 Variables used in the search for zero lepton**

¹⁴⁹² **SUSY**

1493

Chapter 8

1494

Title of Chapter 1

1495

Chapter 9

1496

Title of Chapter 1

1497 Here you can write some introductory remarks about your chapter. I like to give each
1498 sentence its own line.

1499 When you need a new paragraph, just skip an extra line.

1500 **9.1 Object reconstruction**

1501 **Photons, Muons, and Electrons**

1502 **Jets**

1503 **Missing transverse momentum**

1504 Probably longer, show some plots from the PUB note that we worked on

1505 **9.2 Signal regions**

1506 **Gluino signal regions**

1507 **Squark signal regions**

1508 **Compressed signal regions**

1509 **9.3 Background estimation**

1510 **Z vv**

1511 **W ev**

1512 **ttbar**

1513

Chapter 10

1514

Title of Chapter 1

1515 Here you can write some introductory remarks about your chapter. I like to give each

1516 sentence its own line.

1517 When you need a new paragraph, just skip an extra line.

1518 **10.1 Statistical Analysis**

1519 maybe to be moved to an appendix

1520 **10.2 Signal Region distributions**

1521 **10.3 Pull Plots**

1522 **10.4 Systematic Uncertainties**

1523 **10.5 Exclusion plots**

1524

Conclusion

1525 Here you can write some introductory remarks about your chapter. I like to give each
1526 sentence its own line.

1527 When you need a new paragraph, just skip an extra line.

1528 **10.6 New Section**

1529 By using the asterisk to start a new section, I keep the section from appearing in the
1530 table of contents. If you want your sections to be numbered and to appear in the
1531 table of contents, remove the asterisk.

Bibliography

- 1533 [1] O. Perdereau, *Planck 2015 cosmological results*,
1534 AIP Conf. Proc. **1743** (2016) p. 050014.
- 1535 [2] N. Aghanim et al.,
1536 *Planck 2016 intermediate results. LI. Features in the cosmic microwave*
1537 *background temperature power spectrum and shifts in cosmological parameters*
1538 (2016), arXiv: [1608.02487 \[astro-ph.CO\]](https://arxiv.org/abs/1608.02487).
- 1539 [3] J. S. Schwinger,
1540 *On Quantum electrodynamics and the magnetic moment of the electron*,
1541 Phys. Rev. **73** (1948) p. 416.
- 1542 [4] S. Laporta and E. Remiddi,
1543 *The Analytical value of the electron (g-2) at order alpha**3 in QED*,
1544 Phys. Lett. **B379** (1996) p. 283, arXiv: [hep-ph/9602417 \[hep-ph\]](https://arxiv.org/abs/hep-ph/9602417).
- 1545 [5] S. Schael et al., *Precision electroweak measurements on the Z resonance*,
1546 Phys. Rept. **427** (2006) p. 257, arXiv: [hep-ex/0509008 \[hep-ex\]](https://arxiv.org/abs/hep-ex/0509008).
- 1547 [6] S. L. Glashow, *Partial Symmetries of Weak Interactions*,
1548 Nucl. Phys. **22** (1961) p. 579.
- 1549 [7] S. Weinberg, *A Model of Leptons*, Phys. Rev. Lett. **19** (1967) p. 1264.
- 1550 [8] A. Salam, *Weak and Electromagnetic Interactions*,
1551 Conf. Proc. **C680519** (1968) p. 367.
- 1552 [9] M. Gell-Mann, *A Schematic Model of Baryons and Mesons*,
1553 Phys. Lett. **8** (1964) p. 214.
- 1554 [10] G. Zweig, “An SU(3) model for strong interaction symmetry and its
1555 breaking. Version 2,” *DEVELOPMENTS IN THE QUARK THEORY OF*
1556 *HADRONS. VOL. 1. 1964 - 1978*, ed. by D. Lichtenberg and S. P. Rosen,
1557 1964 p. 22,
1558 URL: <http://inspirehep.net/record/4674/files/cern-th-412.pdf>.

- 1559 [11] S. Weinberg, *Implications of Dynamical Symmetry Breaking*,
1560 Phys. Rev. **D13** (1976) p. 974.
- 1561 [12] S. Weinberg, *Implications of Dynamical Symmetry Breaking: An Addendum*,
1562 Phys. Rev. **D19** (1979) p. 1277.
- 1563 [13] E. Gildener, *Gauge Symmetry Hierarchies*, Phys. Rev. **D14** (1976) p. 1667.
- 1564 [14] L. Susskind, *Dynamics of Spontaneous Symmetry Breaking in the*
1565 *Weinberg-Salam Theory*, Phys. Rev. **D20** (1979) p. 2619.
- 1566 [15] S. P. Martin, “A Supersymmetry Primer,” 1997,
1567 eprint: [arXiv:hep-ph/9709356](https://arxiv.org/abs/hep-ph/9709356).
- 1568 [16] V. C. Rubin and W. K. Ford Jr., *Rotation of the Andromeda Nebula from a*
1569 *Spectroscopic Survey of Emission Regions*, Astrophys. J. **159** (1970) p. 379.
- 1570 [17] M. S. Roberts and R. N. Whitehurst,
1571 “*The rotation curve and geometry of M31 at large galactocentric distances*,
1572 Astrophys. J. **201** (1970) p. 327.
- 1573 [18] V. C. Rubin, N. Thonnard, and W. K. Ford Jr.,
1574 *Rotational properties of 21 SC galaxies with a large range of luminosities and*
1575 *radii, from NGC 4605 /R = 4kpc/ to UGC 2885 /R = 122 kpc/*,
1576 Astrophys. J. **238** (1980) p. 471.
- 1577 [19] V. C. Rubin et al., *Rotation velocities of 16 SA galaxies and a comparison of*
1578 *Sa, Sb, and SC rotation properties*, Astrophys. J. **289** (1985) p. 81.
- 1579 [20] A. Bosma,
1580 *21-cm line studies of spiral galaxies. 2. The distribution and kinematics of*
1581 *neutral hydrogen in spiral galaxies of various morphological types.*,
1582 Astron. J. **86** (1981) p. 1825.
- 1583 [21] M. Persic, P. Salucci, and F. Stel, *The Universal rotation curve of spiral*
1584 *galaxies: 1. The Dark matter connection*,
1585 Mon. Not. Roy. Astron. Soc. **281** (1996) p. 27,
1586 arXiv: [astro-ph/9506004](https://arxiv.org/abs/astro-ph/9506004) [astro-ph].
- 1587 [22] M. Lisanti, “Lectures on Dark Matter Physics,” 2016,
1588 eprint: [arXiv:1603.03797](https://arxiv.org/abs/1603.03797).
- 1589 [23] H. Miyazawa, *Baryon Number Changing Currents*,
1590 Prog. Theor. Phys. **36** (1966) p. 1266.

- 1591 [24] J.-L. Gervais and B. Sakita, *Generalizations of dual models*,
 1592 *Nucl. Phys.* **B34** (1971) p. 477.
- 1593 [25] J.-L. Gervais and B. Sakita,
 1594 *Field Theory Interpretation of Supergauges in Dual Models*,
 1595 *Nucl. Phys.* **B34** (1971) p. 632.
- 1596 [26] Yu. A. Golfand and E. P. Likhtman, *Extension of the Algebra of Poincare
 1597 Group Generators and Violation of p Invariance*,
 1598 *JETP Lett.* **13** (1971) p. 323, [*Pisma Zh. Eksp. Teor. Fiz.* **13**, 452 (1971)].
- 1599 [27] A. Neveu and J. H. Schwarz, *Factorizable dual model of pions*,
 1600 *Nucl. Phys.* **B31** (1971) p. 86.
- 1601 [28] A. Neveu and J. H. Schwarz, *Quark Model of Dual Pions*,
 1602 *Phys. Rev.* **D4** (1971) p. 1109.
- 1603 [29] D. V. Volkov and V. P. Akulov, *Is the Neutrino a Goldstone Particle?*
 1604 *Phys. Lett.* **B46** (1973) p. 109.
- 1605 [30] J. Wess and B. Zumino,
 1606 *A Lagrangian Model Invariant Under Supergauge Transformations*,
 1607 *Phys. Lett.* **B49** (1974) p. 52.
- 1608 [31] A. Salam and J. A. Strathdee, *Supersymmetry and Nonabelian Gauges*,
 1609 *Phys. Lett.* **B51** (1974) p. 353.
- 1610 [32] S. Ferrara, J. Wess, and B. Zumino, *Supergauge Multiplets and Superfields*,
 1611 *Phys. Lett.* **B51** (1974) p. 239.
- 1612 [33] J. Wess and B. Zumino, *Supergauge Transformations in Four-Dimensions*,
 1613 *Nucl. Phys.* **B70** (1974) p. 39.
- 1614 [34] J. D. Lykken, “Introduction to supersymmetry,” *Fields, strings and duality. Proceedings, Summer School, Theoretical Advanced Study Institute in Elementary Particle Physics, TASI’96, Boulder, USA, June 2-28, 1996*, 1996
 1615 p. 85, arXiv: [hep-th/9612114](https://arxiv.org/abs/hep-th/9612114) [hep-th],
 1616 URL: http://lss.fnal.gov/cgi-bin/find_paper.pl?pub=96-445-T.
- 1619 [35] A. Kobakhidze, “Intro to SUSY,” 2016, URL: <https://indico.cern.ch/event/443176/page/5225-pre-susy-programme>.
- 1621 [36] G. R. Farrar and P. Fayet, *Phenomenology of the Production, Decay, and
 1622 Detection of New Hadronic States Associated with Supersymmetry*,
 1623 *Phys. Lett.* **B76** (1978) p. 575.

- 1624 [37] ATLAS Collaboration,
 1625 *Search for the electroweak production of supersymmetric particles in*
 1626 $\sqrt{s} = 8 \text{ TeV}$ *pp collisions with the ATLAS detector,*
 1627 *Phys. Rev. D* **93** (2016) p. 052002, arXiv: [1509.07152 \[hep-ex\]](#).
- 1628 [38] ATLAS Collaboration, *Summary of the searches for squarks and gluinos*
 1629 *using $\sqrt{s} = 8 \text{ TeV}$ pp collisions with the ATLAS experiment at the LHC,*
 1630 *JHEP* **10** (2015) p. 054, arXiv: [1507.05525 \[hep-ex\]](#).
- 1631 [39] ATLAS Collaboration, *ATLAS Run 1 searches for direct pair production of*
 1632 *third-generation squarks at the Large Hadron Collider,*
 1633 *Eur. Phys. J. C* **75** (2015) p. 510, arXiv: [1506.08616 \[hep-ex\]](#).
- 1634 [40] CMS Collaboration, *Search for supersymmetry with razor variables in pp*
 1635 *collisions at $\sqrt{s} = 7 \text{ TeV}$, Phys. Rev. D* **90** (2014) p. 112001,
 1636 arXiv: [1405.3961 \[hep-ex\]](#).
- 1637 [41] CMS Collaboration, *Inclusive search for supersymmetry using razor variables*
 1638 *in pp collisions at $\sqrt{s} = 7 \text{ TeV}$, Phys. Rev. Lett.* **111** (2013) p. 081802,
 1639 arXiv: [1212.6961 \[hep-ex\]](#).
- 1640 [42] CMS Collaboration, *Search for Supersymmetry in pp Collisions at 7 TeV in*
 1641 *Events with Jets and Missing Transverse Energy,*
 1642 *Phys. Lett. B* **698** (2011) p. 196, arXiv: [1101.1628 \[hep-ex\]](#).
- 1643 [43] CMS Collaboration, *Search for Supersymmetry at the LHC in Events with*
 1644 *Jets and Missing Transverse Energy, Phys. Rev. Lett.* **107** (2011) p. 221804,
 1645 arXiv: [1109.2352 \[hep-ex\]](#).
- 1646 [44] CMS Collaboration, *Search for supersymmetry in hadronic final states using*
 1647 *M_{T2} in pp collisions at $\sqrt{s} = 7 \text{ TeV}$, JHEP* **10** (2012) p. 018,
 1648 arXiv: [1207.1798 \[hep-ex\]](#).
- 1649 [45] CMS Collaboration, *Searches for supersymmetry using the M_{T2} variable in*
 1650 *hadronic events produced in pp collisions at 8 TeV, JHEP* **05** (2015) p. 078,
 1651 arXiv: [1502.04358 \[hep-ex\]](#).
- 1652 [46] CMS Collaboration, *Search for new physics with the M_{T2} variable in all-jets*
 1653 *final states produced in pp collisions at $\sqrt{s} = 13 \text{ TeV}$ (2016),*
 1654 arXiv: [1603.04053 \[hep-ex\]](#).
- 1655 [47] ATLAS Collaboration, *Multi-channel search for squarks and gluinos in*
 1656 $\sqrt{s} = 7 \text{ TeV}$ *pp collisions with the ATLAS detector at the LHC,*
 1657 *Eur. Phys. J. C* **73** (2013) p. 2362, arXiv: [1212.6149 \[hep-ex\]](#).

- 1658 [48] Y. Grossman, “Introduction to the SM,” 2016, URL: <https://indico.fnal.gov/sessionDisplay.py?sessionId=3&confId=11505#20160811>.
- 1659
- 1660 [49] () .
- 1661 [50] P. W. Higgs, *Broken Symmetries and the Masses of Gauge Bosons*,
1662 *Phys. Rev. Lett.* **13** (1964) p. 508.
- 1663 [51] ATLAS Collaboration, *Observation of a new particle in the search for the*
1664 *Standard Model Higgs boson with the ATLAS detector at the LHC*,
1665 *Phys. Lett. B* **716** (2012) p. 1, arXiv: [1207.7214 \[hep-ex\]](https://arxiv.org/abs/1207.7214) .
- 1666 [52] CMS Collaboration, *Observation of a new boson at a mass of 125 GeV with*
1667 *the CMS experiment at the LHC*, *Phys. Lett. B* **716** (2012) p. 30,
1668 arXiv: [1207.7235 \[hep-ex\]](https://arxiv.org/abs/1207.7235) .
- 1669 [53] A. Chodos et al., *A New Extended Model of Hadrons*,
1670 *Phys. Rev. D* **9** (1974) p. 3471.
- 1671 [54] A. Chodos et al., *Baryon Structure in the Bag Theory*,
1672 *Phys. Rev. D* **10** (1974) p. 2599.
- 1673 [55] J. C. Collins, D. E. Soper, and G. F. Sterman,
1674 *Factorization of Hard Processes in QCD*,
1675 *Adv. Ser. Direct. High Energy Phys.* **5** (1989) p. 1,
1676 arXiv: [hep-ph/0409313 \[hep-ph\]](https://arxiv.org/abs/hep-ph/0409313) .
- 1677 [56] K. A. Olive et al., *Review of Particle Physics*,
1678 *Chin. Phys. C* **38** (2014) p. 090001.
- 1679 [57] N. Cabibbo, *Unitary Symmetry and Leptonic Decays*,
1680 *Phys. Rev. Lett.* **10** (1963) p. 531, [,648(1963)].
- 1681 [58] M. Kobayashi and T. Maskawa,
1682 *CP Violation in the Renormalizable Theory of Weak Interaction*,
1683 *Prog. Theor. Phys.* **49** (1973) p. 652.
- 1684 [59] W. F. L. Hollik, *Radiative Corrections in the Standard Model and their Role*
1685 *for Precision Tests of the Electroweak Theory*,
1686 *Fortsch. Phys.* **38** (1990) p. 165.
- 1687 [60] D. Yu. Bardin et al.,
1688 *ELECTROWEAK RADIATIVE CORRECTIONS TO DEEP INELASTIC*
1689 *SCATTERING AT HERA! CHARGED CURRENT SCATTERING*,
1690 *Z. Phys. C* **44** (1989) p. 149.

- 1691 [61] D. C. Kennedy et al.,
 1692 *Electroweak Cross-Sections and Asymmetries at the Z0*,
 1693 *Nucl. Phys.* **B321** (1989) p. 83.
- 1694 [62] A. Sirlin, *Radiative Corrections in the SU(2)-L x U(1) Theory: A Simple*
 1695 *Renormalization Framework*, *Phys. Rev.* **D22** (1980) p. 971.
- 1696 [63] S. Fanchiotti, B. A. Kniehl, and A. Sirlin,
 1697 *Incorporation of QCD effects in basic corrections of the electroweak theory*,
 1698 *Phys. Rev.* **D48** (1993) p. 307, arXiv: [hep-ph/9212285 \[hep-ph\]](#).
- 1699 [64] C. Quigg, “Cosmic Neutrinos,” *Proceedings, 35th SLAC Summer Institute on*
 1700 *Particle Physics: Dark matter: From the cosmos to the Laboratory (SSI*
 1701 *2007): Menlo Park, California, July 30- August 10, 2007*, 2008,
 1702 arXiv: [0802.0013 \[hep-ph\]](#),
 1703 URL: http://lss.fnal.gov/cgi-bin/find_paper.pl?conf=07-417.
- 1704 [65] S. R. Coleman and J. Mandula, *All Possible Symmetries of the S Matrix*,
 1705 *Phys. Rev.* **159** (1967) p. 1251.
- 1706 [66] R. Haag, J. T. Lopuszanski, and M. Sohnius,
 1707 *All Possible Generators of Supersymmetries of the s Matrix*,
 1708 *Nucl. Phys.* **B88** (1975) p. 257.
- 1709 [67] A. Salam and J. A. Strathdee, *On Superfields and Fermi-Bose Symmetry*,
 1710 *Phys. Rev.* **D11** (1975) p. 1521.
- 1711 [68] S. Dimopoulos and H. Georgi, *Softly Broken Supersymmetry and SU(5)*,
 1712 *Nucl. Phys.* **B193** (1981) p. 150.
- 1713 [69] S. Dimopoulos, S. Raby, and F. Wilczek,
 1714 *Supersymmetry and the Scale of Unification*, *Phys. Rev.* **D24** (1981) p. 1681.
- 1715 [70] L. E. Ibanez and G. G. Ross,
 1716 *Low-Energy Predictions in Supersymmetric Grand Unified Theories*,
 1717 *Phys. Lett.* **B105** (1981) p. 439.
- 1718 [71] W. J. Marciano and G. Senjanovic,
 1719 *Predictions of Supersymmetric Grand Unified Theories*,
 1720 *Phys. Rev.* **D25** (1982) p. 3092.
- 1721 [72] L. Girardello and M. T. Grisaru, *Soft Breaking of Supersymmetry*,
 1722 *Nucl. Phys.* **B194** (1982) p. 65.

- 1723 [73] D. J. H. Chung et al.,
 1724 *The Soft supersymmetry breaking Lagrangian: Theory and applications*,
 1725 Phys. Rept. **407** (2005) p. 1, arXiv: [hep-ph/0312378 \[hep-ph\]](#).
- 1726 [74] J. Hisano et al., *Lepton flavor violation in the supersymmetric standard*
 1727 *model with seesaw induced neutrino masses*, Phys. Lett. **B357** (1995) p. 579,
 1728 arXiv: [hep-ph/9501407 \[hep-ph\]](#).
- 1729 [75] F. Gabbiani et al., *A Complete analysis of FCNC and CP constraints in*
 1730 *general SUSY extensions of the standard model*,
 1731 Nucl. Phys. **B477** (1996) p. 321, arXiv: [hep-ph/9604387 \[hep-ph\]](#).
- 1732 [76] F. Gabbiani and A. Masiero,
 1733 *FCNC in Generalized Supersymmetric Theories*,
 1734 Nucl. Phys. **B322** (1989) p. 235.
- 1735 [77] J. S. Hagelin, S. Kelley, and T. Tanaka, *Supersymmetric flavor changing*
 1736 *neutral currents: Exact amplitudes and phenomenological analysis*,
 1737 Nucl. Phys. **B415** (1994) p. 293.
- 1738 [78] J. S. Hagelin, S. Kelley, and V. Ziegler, *Using gauge coupling unification and*
 1739 *proton decay to test minimal supersymmetric SU(5)*,
 1740 Phys. Lett. **B342** (1995) p. 145, arXiv: [hep-ph/9406366 \[hep-ph\]](#).
- 1741 [79] D. Choudhury et al.,
 1742 *Constraints on nonuniversal soft terms from flavor changing neutral currents*,
 1743 Phys. Lett. **B342** (1995) p. 180, arXiv: [hep-ph/9408275 \[hep-ph\]](#).
- 1744 [80] R. Barbieri and L. J. Hall, *Signals for supersymmetric unification*,
 1745 Phys. Lett. **B338** (1994) p. 212, arXiv: [hep-ph/9408406 \[hep-ph\]](#).
- 1746 [81] B. de Carlos, J. A. Casas, and J. M. Moreno,
 1747 *Constraints on supersymmetric theories from mu —> e gamma*,
 1748 Phys. Rev. **D53** (1996) p. 6398, arXiv: [hep-ph/9507377 \[hep-ph\]](#).
- 1749 [82] J. A. Casas and S. Dimopoulos,
 1750 *Stability bounds on flavor violating trilinear soft terms in the MSSM*,
 1751 Phys. Lett. **B387** (1996) p. 107, arXiv: [hep-ph/9606237 \[hep-ph\]](#).
- 1752 [83] C. Borschensky et al., *Squark and gluino production cross sections in pp*
 1753 *collisions at $\sqrt{s} = 13, 14, 33$ and 100 TeV*,
 1754 Eur. Phys. J. **C74** (2014) p. 3174, arXiv: [1407.5066 \[hep-ph\]](#).
- 1755 [84] M. Klasen, M. Pohl, and G. Sigl, *Indirect and direct search for dark matter*,
 1756 Prog. Part. Nucl. Phys. **85** (2015) p. 1, arXiv: [1507.03800 \[hep-ph\]](#).

- 1757 [85] L. Evans and P. Bryant, *LHC Machine*, JINST **3** (2008) S08001.
- 1758 [86] V. Shiltsev, “Accelerator Physics and Technology,” 2016,
 1759 URL: [https://indico.fnal.gov/sessionDisplay.py?sessionId=3&](https://indico.fnal.gov/sessionDisplay.py?sessionId=3&confId=11505#20160811)
 1760 [confId=11505#20160811](#).
- 1761 [87] *LEP design report*, Copies shelved as reports in LEP, PS and SPS libraries,
 1762 Geneva: CERN, 1984, URL: <https://cds.cern.ch/record/102083>.
- 1763 [88] ATLAS Collaboration,
 1764 *The ATLAS Experiment at the CERN Large Hadron Collider*,
 1765 JINST **3** (2008) S08003.
- 1766 [89] ATLAS Collaboration, *2015 start-up trigger menu and initial performance*
 1767 *assessment of the ATLAS trigger using Run-2 data*,
 1768 ATL-DAQ-PUB-2016-001, 2016,
 1769 URL: <https://cds.cern.ch/record/2136007/>.
- 1770 [90] ATLAS Collaboration, *Performance of the ATLAS Inner Detector Track and*
 1771 *Vertex Reconstruction in High Pile-Up LHC Environment*,
 1772 ATLAS-CONF-2012-042, 2012,
 1773 URL: <https://cds.cern.ch/record/1435196>.
- 1774 [91] ATLAS Collaboration, *Early Inner Detector Tracking Performance in the*
 1775 *2015 Data at $\sqrt{s} = 13 \text{ TeV}$* , ATL-PHYS-PUB-2015-051, 2015,
 1776 URL: <https://cds.cern.ch/record/2110140>.
- 1777 [92] K Hamano, A Morley, and A Salzburger,
 1778 “Track Reconstruction Performance and Efficiency Estimation using different
 1779 ID geometry samples,” tech. rep. ATL-COM-PHYS-2012-1541,
 1780 plots for a poster at HCP: CERN, 2012,
 1781 URL: <https://cds.cern.ch/record/1489674>.
- 1782 [93] ATLAS Collaboration,
 1783 *Electron reconstruction and identification efficiency measurements with the*
 1784 *ATLAS detector using the 2011 LHC proton–proton collision data*,
 1785 Eur. Phys. J. C **74** (2014) p. 2941, arXiv: [1404.2240 \[hep-ex\]](https://arxiv.org/abs/1404.2240).
- 1786 [94] ATLAS Collaboration, *Topological cell clustering in the ATLAS calorimeters*
 1787 *and its performance in LHC Run 1* (2016), arXiv: [1603.02934 \[hep-ex\]](https://arxiv.org/abs/1603.02934).
- 1788 [95] ATLAS Collaboration, *Jet energy resolution in proton–proton collisions at*
 1789 *$\sqrt{s} = 7 \text{ TeV}$ recorded in 2010 with the ATLAS detector*,
 1790 Eur. Phys. J. C **73** (2013) p. 2306, arXiv: [1210.6210 \[hep-ex\]](https://arxiv.org/abs/1210.6210).

- 1791 [96] M. Aaboud et al., *Measurement of the photon identification efficiencies with*
 1792 *the ATLAS detector using LHC Run-1 data* (2016),
 1793 arXiv: [1606.01813 \[hep-ex\]](https://arxiv.org/abs/1606.01813).
- 1794 [97] ATLAS Collaboration, *Electron and photon energy calibration with the*
 1795 *ATLAS detector using LHC Run 1 data*, Eur. Phys. J. C **74** (2014) p. 3071,
 1796 arXiv: [1407.5063 \[hep-ex\]](https://arxiv.org/abs/1407.5063).
- 1797 [98] “Electron and photon energy calibration with the ATLAS detector using
 1798 data collected in 2015 at $\sqrt{s} = 13$ TeV,”
 1799 tech. rep. ATL-PHYS-PUB-2016-015, CERN, 2016,
 1800 URL: <https://cds.cern.ch/record/2203514>.
- 1801 [99] ATLAS Collaboration, *Muon reconstruction performance of the ATLAS*
 1802 *detector in proton–proton collision data at $\sqrt{s} = 13$ TeV* (2016),
 1803 arXiv: [1603.05598 \[hep-ex\]](https://arxiv.org/abs/1603.05598).
- 1804 [100] ATLAS Collaboration, *Jet energy measurement with the ATLAS detector in*
 1805 *proton–proton collisions at $\sqrt{s} = 7$ TeV*, Eur. Phys. J. C **73** (2013) p. 2304,
 1806 arXiv: [1112.6426 \[hep-ex\]](https://arxiv.org/abs/1112.6426).
- 1807 [101] ATLAS Collaboration,
 1808 *Jet energy measurement and its systematic uncertainty in proton–proton*
 1809 *collisions at $\sqrt{s} = 7$ TeV with the ATLAS detector*,
 1810 Eur. Phys. J. C **75** (2015) p. 17, arXiv: [1406.0076 \[hep-ex\]](https://arxiv.org/abs/1406.0076).
- 1811 [102] S. D. Ellis and D. E. Soper,
 1812 *Successive combination jet algorithm for hadron collisions*,
 1813 Phys. Rev. **D48** (1993) p. 3160, arXiv: [hep-ph/9305266 \[hep-ph\]](https://arxiv.org/abs/hep-ph/9305266).
- 1814 [103] M. Cacciari and G. P. Salam, *Dispelling the N^3 myth for the k_t jet-finder*,
 1815 Phys. Lett. **B641** (2006) p. 57, arXiv: [hep-ph/0512210 \[hep-ph\]](https://arxiv.org/abs/hep-ph/0512210).
- 1816 [104] M. Cacciari, G. P. Salam, and G. Soyez,
 1817 *The Anti- $k(t)$ jet clustering algorithm*, JHEP **04** (2008) p. 063,
 1818 arXiv: [0802.1189 \[hep-ph\]](https://arxiv.org/abs/0802.1189).
- 1819 [105] *Particle-Flow Event Reconstruction in CMS and Performance for Jets, Taus, and MET* (2009).
- 1821 [106] ATLAS Collaboration,
 1822 *Tagging and suppression of pileup jets with the ATLAS detector*,
 1823 ATLAS-CONF-2014-018, 2014,
 1824 URL: <https://cds.cern.ch/record/1700870>.

- 1825 [107] M. Cacciari, G. P. Salam, and G. Soyez, *The Catchment Area of Jets*,
 1826 JHEP **04** (2008) p. 005, arXiv: [0802.1188 \[hep-ph\]](https://arxiv.org/abs/0802.1188).
- 1827 [108] “Optimisation of the ATLAS b -tagging performance for the 2016 LHC Run,”
 1828 tech. rep. ATL-PHYS-PUB-2016-012, CERN, 2016,
 1829 URL: <https://cds.cern.ch/record/2160731>.
- 1830 [109] G. Aad et al., *Performance of algorithms that reconstruct missing transverse*
 1831 *momentum in $\sqrt{s} = 8$ TeV proton-proton collisions in the ATLAS detector*
 1832 (2016), arXiv: [1609.09324 \[hep-ex\]](https://arxiv.org/abs/1609.09324).
- 1833 [110] ATLAS Collaboration,
 1834 *Prospects for Supersymmetry discovery based on inclusive searches at a*
 1835 *7 TeV centre-of-mass energy with the ATLAS detector*,
 1836 ATL-PHYS-PUB-2010-010, 2010,
 1837 URL: <https://cds.cern.ch/record/1278474>.
- 1838 [111] ATLAS Collaboration,
 1839 *Expected sensitivity studies for gluino and squark searches using the early*
 1840 *LHC 13 TeV Run-2 dataset with the ATLAS experiment*,
 1841 ATL-PHYS-PUB-2015-005, 2015, URL:
 1842 [https://atlas.web.cern.ch/Atlas/GROUPS/PHYSICS/PUBNOTES/ATL-](https://atlas.web.cern.ch/Atlas/GROUPS/PHYSICS/PUBNOTES/ATL-PHYS-PUB-2015-005)
 1843 [PHYS-PUB-2015-005](https://atlas.web.cern.ch/Atlas/GROUPS/PHYSICS/PUBNOTES/ATL-PHYS-PUB-2015-005).
- 1844 [112] ATLAS Collaboration, *Expected performance of missing transverse*
 1845 *momentum reconstruction for the ATLAS detector at $\sqrt{s} = 13$ TeV*,
 1846 ATL-PHYS-PUB-2015-023, 2015,
 1847 URL: <https://cds.cern.ch/record/2037700>.
- 1848 [113] ATLAS Collaboration,
 1849 *Performance of missing transverse momentum reconstruction with the*
 1850 *ATLAS detector in the first proton–proton collisions at $\sqrt{s} = 13$ TeV*,
 1851 ATL-PHYS-PUB-2015-027, 2015,
 1852 URL: <https://cds.cern.ch/record/2037904>.
- 1853 [114] CMS Collaboration, *Search for supersymmetry using razor variables in*
 1854 *events with b -tagged jets in pp collisions at $\sqrt{s} = 8$ TeV*,
 1855 Phys. Rev. D **91** (2015) p. 052018, arXiv: [1502.00300 \[hep-ex\]](https://arxiv.org/abs/1502.00300).

1856

The Standard Model

1857 In this appendix, we provide a brief overview of the basic ingredients involved in
1858 construction of the Standard Model Lagrangian : quantum field theory, symmetries,
1859 and symmetry breaking.

1860 **Quantum Field Theory**

1861 **TODO: cite Yuval's lectures and notes somehow**

1862 In this section, we provide a brief overview of the necessary concepts from
1863 Quantum Field Theory (QFT).

1864 In modern physics, the laws of nature are described by the “action” S , with the
1865 imposition of the principle of minimum action. **TODO: cite** The action is the integral
1866 over the spacetime coordinates of the “Lagrangian density” \mathcal{L} , or Lagrangian for
1867 short. The Lagrangian is a function of “fields”; general fields will be called $\phi(x^\mu)$,
1868 where the indices μ run over the space-time coordinates. We can then write the action
1869 S as

$$S = \int d^4x \mathcal{L}[\phi_i(x^\mu), \partial_\mu \phi_i(x^\mu)] \quad (10.1)$$

1870 where we have an additional summation over i (of the different fields). Generally,
1871 we impose the following constraints on the Lagrangian :

1872 1. Translational invariance - The Lagrangian is only a function of the fields ϕ and
1873 their derivatives $\partial_\mu \phi$

1874 2. Locality - The Lagrangian is only a function of one point x_μ in spacetime.

1875 3. Reality condition - The Lagrangian is real to conserve probability.

1876 4. Lorentz invariance - The Lagrangian is invariant under the Poincarégroup of

1877 spacetime.

1878 5. Analyticity - The Lagrangian is an analytical function of the fields; this is to

1879 allow the use of perturbation theory.

1880 6. Invariance and Naturalness - The Lagrangian is invariant under some internal

1881 symmetry groups; in fact, the Lagrangian will have *all* terms allowed by the

1882 imposed symmetry groups. **TODO: maybe add in ref here**

1883 7. Renormalizability - The Lagrangian will be renormalizable - in practice, this

1884 means there will not be terms with more than power 4 in the fields.

1885 The key item from the point of view of this thesis is that of “Invariance and

1886 Natural”. We impose a set of “symmetries” and then our Lagrangian is the most

1887 general which is allowed by those symmetries.

1888 **Symmetries**

1889 Symmetries can be seen as the fundamental guiding concept of modern physics.

1890 Symmetries are described by “groups”. **TODO: cite?**. To illustrate the importance

1891 of symmetries and their mathematical description, groups, we start here with two of

1892 the simplest and most useful examples : \mathbb{Z}_2 and $U(1)$.

1893 **\mathbb{Z}_2 symmetry**

1894 \mathbb{Z}_2 symmetry is the simplest example of a “discrete” symmetry. Consider the most

1895 general Lagrangian of a single real scalar field $\phi(x_\mu)$

$$\mathcal{L}_\phi = \frac{1}{2}\partial_\mu\phi\partial^\mu\phi - \frac{m^2}{2}\phi^2 - \frac{\mu}{2\sqrt{2}}\phi^3 - \lambda\phi^4 \quad (10.2)$$

Now we *impose* the symmetry

$$\mathcal{L}(\phi) = \mathcal{L}(-\phi) \quad (10.3)$$

1896 This has the effect of restricting the allowed terms of the Lagrangian. In particular,
 1897 we can see the term $\phi^3 \rightarrow -\phi^3$ under the symmetry transformation, and thus must
 1898 be disallowed by this symmetry. This means under the imposition of this particular
 1899 symmetry, our Lagrangian should be rewritten as

$$\mathcal{L}_\phi = \frac{1}{2}\partial_\mu\phi\partial^\mu\phi - \frac{m^2}{2}\phi^2 - \lambda\phi^4 \quad (10.4)$$

1900 The effect of this symmetry is that the total number of ϕ particles can only change
 1901 by even numbers, since the only interaction term $\lambda\phi^4$ is an even power of the field.
 1902 This symmetry is often imposed in supersymmetric theories, as we will see in Chapter
 1903 3.

1904 **$U(1)$ symmetry**

1905 $U(1)$ is the simplest example of a continuous (or *Lie*) group. Now consider a theory
 1906 with a single complex scalar field $\phi = \text{Re } \phi + i \text{Im } \phi$

$$\mathcal{L}_\phi = \delta_{i,j} \frac{1}{2}\partial_\mu\phi_i\partial^\mu\phi_j - \frac{m^2}{2}\phi_i\phi_j - \frac{\mu}{2\sqrt{2}}\phi_i\phi_j\phi_k\phi_l - \lambda\phi_i\phi_j\phi_k\phi_l \quad (10.5)$$

1907 where $i, j, k, l = \text{Re}, \text{Im}$. In this case, we impose the following $U(1)$ symmetry
 1908 : $\phi \rightarrow e^{i\theta}, \phi^* \rightarrow e^{-i\theta}$. We see immediately that this again disallows the third-order
 1909 terms, and we can write a theory of a complex scalar field with $U(1)$ symmetry as

$$\mathcal{L}_\phi = \partial_\mu\phi\partial^\mu\phi^* - \frac{m^2}{2}\phi\phi^* - \lambda(\phi\phi^*)^2 \quad (10.6)$$

1910 Local symmetries

1911 The two examples considered above are “global” symmetries in the sense that the
 1912 symmetry transformation does not depends on the spacetime coordinate x_μ . We know
 1913 look at local symmetries; in this case, for example with a local $U(1)$ symmetry, the
 1914 transformation has the form $\phi(x_\mu) \rightarrow e^{i\theta(x_\mu)}\phi(x_\mu)$. These symmetries are also known
 1915 as “gauge” symmetries; all symmetries of the Standard Model are gauge symmetries.

There are wide-ranging consequences to the imposition of local symmetries. To begin, we note that the derivative terms of the Lagrangian 10.2 are *not* invariant under a local symmetry transformation

$$\partial_\mu \phi(x_\mu) \rightarrow \partial_\mu(e^{i\theta(x_\mu)}\phi(x_\mu)) = (1 + i\theta(x_\mu))e^{i\theta(x_\mu)}\phi(x_\mu) \quad (10.7)$$

1916 TODO: GET THIS RIGHT

1917 This leads us to note that the kinetic terms of the Lagrangian are also not invariant
 1918 under a gauge symmetry. This would lead to a model with no dynamics, which is
 1919 clearly unsatisfactory.

1920 Let us take inspiration from the case of global symmetries. We need to define a
 1921 so-called “covariant” derivative D^μ such that

$$D^\mu \phi \rightarrow e^{iq\theta(x^\mu)D^\mu}\phi \quad (10.8)$$

$$D^\mu \phi^* \rightarrow e^{-iq\theta(x^\mu)D^\mu}\phi^* \quad (10.9)$$

$$(10.10)$$

1922 Since ϕ and ϕ^* transforms with the opposite phase, this will lead the invariance
 1923 of the Lagrangian under our local gauge transformation. This D^μ is of the following
 1924 form

$$D^\mu = \partial_\mu - igqA^\mu \quad (10.11)$$

1925 where A^μ is a vector field we introduce with the transformation law

$$A^\mu \rightarrow A^\mu - \frac{1}{g} \partial_\mu \theta \quad (10.12)$$

1926 and g is the coupling constant associated to vector field. This vector field A^μ is
1927 also known as a “gauge” field.

1928 Since we need to add all allowed terms to the Lagrangian, we define

$$F^{\mu\nu} = A^\mu A^\nu - A^\nu A^\mu \quad (10.13)$$

1929 and then we must also add the kinetic term :

$$\mathcal{L}_{\text{gauge}} = -\frac{1}{4} F^{\mu\nu} F_{\mu\nu} \quad (10.14)$$

1930 The most general renormalizable Lagrangian with fermion and scalar fields can
1931 be written in the following form

$$\mathcal{L} = \mathcal{L}_{\text{kin}} + \mathcal{L}_\phi + \mathcal{L}_\psi + \mathcal{L}_{\text{Yukawa}} \quad (10.15)$$

1932 Symmetry breaking and the Higgs mechanism

1933 Here we view some examples of symmetry breaking. We investigate breaking of a
1934 global $U(1)$ symmetry and a local $U(1)$ symmetry. The SM will break the electroweak
1935 symmetry $SU(2)xU(1)$, and in Chapter 3 we will see how supersymmetry must also
1936 be broken.

1937 There are two ideas of symmetry breaking

- 1938 • Explicit symmetry breaking by a small parameter - in this case, we have a small
1939 parameter which breaks an “approximate” symmetry of our Lagrangian. An
1940 example would be the theory of the single scalar field 10.2, when $\mu \ll m^2$ and

1941 $\mu \ll \lambda$. In this case, we can often ignore the small term when considering
 1942 low-energy processes.

1943 • Spontaneous symmetry breaking (SSB) - spontaneous symmetry breaking
 1944 occurs when the Lagrangian is symmetric with respect to a given symmetry
 1945 transformation, but the ground state of the theory is *not* symmetric with respect
 1946 to that transformation. This can have some fascinating consequences, as we
 1947 will see in the following examples

1948 Symmetry breaking a

1949 **U(1) global symmetry breaking**

Consider the theory of a complex scalar field under the $U(1)$ symmetry, or the transformation

$$\phi \rightarrow e^{i\theta} \phi \quad (10.16)$$

The Lagrangian for this theory is

$$\mathcal{L} = \partial^\mu \phi^\dagger \partial_\mu \phi + \frac{\mu^2}{2} \phi^\dagger \phi + \frac{\lambda}{4} (\phi^\dagger \phi)^2 \quad (10.17)$$

Let us write this theory in terms of two scalar fields, h and ξ : $\phi = (h + i\xi)/\sqrt{2}$.

The Lagrangian can then be written as

$$\mathcal{L} = \partial^\mu h \partial_\mu h + \partial^\mu \xi d\mu \xi - \frac{\mu^2}{2} (h^2 + \xi^2) - \frac{\lambda}{4} (h^2 + \xi^2)^2 \quad (10.18)$$

First, note that the theory is only stable when $\lambda > 0$. To understand the effect of SSB, we now enforce that $\mu^2 < 0$, and define $v^2 = -\mu^2/\lambda$. We can then write the scalar potential of this theory as :

$$V(\phi) = \lambda(\phi^\dagger \phi - v^2/2)^2 \quad (10.19)$$

Minimizing this equation with respect to ϕ , we can see that the “vacuum expectation value” of the theory is

$$2 < \phi^\dagger \phi > = < h^2 + \xi^2 > = v^2 \quad (10.20)$$

1950 We now reach the “breaking” point of this procedure. In the (h, ξ) plane, the
 1951 minima form a circle of radius v . We are free to choose any of these minima to expand
 1952 our Lagrangian around; the physics is not affected by this choice. For convenience,
 1953 choose $\langle h \rangle = v, \langle \xi^2 \rangle = 0$.

Now, let us define $h' = h - v, \xi' = \xi$ with VEVs $\langle h' \rangle = 0, \langle \xi' \rangle = 0$. We can
 then write our spontaneously broken Lagrangian in the form

$$\mathcal{L} = \frac{1}{2} \partial_\mu h' \partial^\mu h' + \frac{1}{2} \partial_\mu \xi' \partial^\mu \xi' - \lambda v^2 h'^2 - \lambda v h' (h'^2 + \xi'^2) - \lambda (h'^2 + \xi'^2)^2 \quad (10.21)$$